Universitat Politècnica de Catalunya

Experimental study of feedback-induced dynamics in semiconductor lasers: from symbolic analysis to subwavelength position sensing.

Tesis presentada por **Andrés Aragoneses Aguado**
para obtener el grado de Doctor en Física
Computacional y Aplicada por la Universitat
Politècnica de Catalunya

Directoras: Cristina Masoller y Maria Carme Torrent

Terrassa, junio 2014

Departament de Física i Enginyeria Nuclear

Resumen

Estudio experimental de la dinámica inducida por realimentación en láseres de semiconductor: análisis simbólico y detección de posición de alta resolución

El objetivo de esta tesis es el estudio de la dinámica inducida por realimentación óptica en láseres de semiconductor. Dicho estudio persigue, por un lado, profundizar en el conocimiento de aspectos generales de los sistemas complejos, y por otro lado, utilizar dicha dinámica para crear un protocolo para medir desplazamientos en dos dimensiones con una resolución mucho menor que la longitud de onda del láser utilizado.

La intensidad de la luz emitida por un láser de semiconductor es estable salvo fluctuaciones debidas al ruido de emisión espontánea. Sin embargo, cuando la luz del láser se refleja en una superficie y parte de esta luz vuelve a entrar en el láser, la intensidad de la luz emitida se puede desestabilizar y mostrar una amplia gama de comportamientos dinámicos.

Uno de los regímenes dinámicos presentes en láseres con realimentación óptica es el de fluctuaciones de baja frecuencia (LFF de sus siglas en inglés). Está dinámica se caracteriza por caídas abruptas de la intensidad del láser (hasta casi apagarse), seguidas de recuperaciones graduales, siendo la separación temporal entre dos caídas consecutivas irregular.

La primera parte de esta tesis está centrada en este régimen dinámico, habiéndose realizado un detallado estudio experimental para caracterizarlo. Se ha utilizado un análisis simbólico de series de datos basado en patrones ordinales, definidos mediante la comparación de tiempos consecutivos entre caídas.

En la dinámica del láser de semiconductor con realimentación intervienen varios factores: la interacción no lineal entre luz y materia en el medio activo del láser, el ruido cuántico debido a la emisión espontánea y la señal retardada de la realimentación. Por ello las caídas en el régimen de LFFs pueden ser inducidas tanto por ruido como por procesos deterministas. En esta tesis, mediante el análisis simbólico se ha conseguido distinguir estadísticamente, qué caídas pueden ser inducidas por ruido y cuales presentan una estadística que muestra señales de determinismo.

En esta tesis también se ha estudiado la dinámica simbólica del régimen de LFF y se han encontrado correlaciones entre varias caídas consecutivas. También se ha encontrado una estructura jerárquica en la dinámica simbólica que incluye emparejamientos de las probabilidades de los patrones simbólicos. Además se ha encontrado un modelo simple a tiempo discreto (mapa) que describe adecuadamente la dinámica simbólica del régimes de LFF.

Debido a la importancia de forzamientos externos en sistemas dinámicos, se han realizado experimentos incorporando modulación en la corriente de inyección del láser. Estos experimentos han permitido caracterizar el efecto de la amplitud de la modulación en la dinámica simbólica, encontrando cambios claros en la estructura simbólica, inducidos por la modulación, pero que se conservan los emparejamientos observados sin modulación. El modelo simple ha sido verificado ya que reproduce satisfactoriamente la dinámica simbólica encontrada en los datos experimentales.

Asimismo, en esta tesis se ha demostrado experimentalmente un protocolo que permite detectar desplazamientos de dos objetos independientes en una escala muy inferior a la longitud de onda de la luz empleada ($\lambda/160$). Para ello se ha diseñado un experimento donde el láser esta sometido a realimentación de dos espejos que se mueven de manera independiente. Además de la alta resolución, otra ventaja de este protocolo reside en que únicamente es preciso medir una variable para calcular los dos desplazamientos.

Abstract

Experimental study of feedback-induced dynamics in semiconductor lasers: from symbolic analysis to subwavelength position sensing

The aim of this thesis is the study of the dynamics induced by optical feedback in semiconductor lasers. This study aims, on the one hand, to improve our knowledge of stocahstic complex systems, and on the other hand, to use complex dynamics of semiconductor lasers to develop a protocol for subwavelength position sensing.

The intensity of the light emitted by a semiconductor laser is stable, besides fluctuations due to spontaneous emission noise. When the light of the laser is reflected and part re-enters into the laser, the laser intensity can become unstable, displaying a broad range of dynamical behaviors.

One of the dynamical regimes present in lasers with optical feedback is the low frequency fluctuations (LFF). This dynamics is characterized by sharp drops in the laser intensity (to almost switch the laser off), followed by gradual recoveries. The time intervals between two consecutive drops is irregular.

The first part of this *Thesis* is focused on this dynamic regime, and a detailed experimental study has been performed to characterize it. A symbolic time series analysis has been used, based on the comparison of successive time intervals between dropouts.

The dynamics of a semiconductor laser with feedback is governed by nonlinear light-matter interaction in the active medium of the laser, quantum noise due to spontaneous emission and time-delayed feedback. Therefore, the dropouts in the LFF regime can be noise-induced or triggered by deterministic processes. In this

Thesis symbolic ordinal analysis has been used to statisticlly distinguish dropouts that can be noise-induced from those that have signatures of a deterministic origin.

In this *Thesis*, the symbolic dynamics in the LFF regime has also been studied, and serial correlations have been found among several consecutive dropouts. It has been found a hierarchical and clustered structure of the symbolic dynamics. Moreover, a minimal iterative model has been found that, despite its simplicity, describes successfully the correlations found in the experiments.

Because of the importance of external forcing in dynamical systems, the effect of current modulation on the symbolic dynamics of the LFFs has been studied. These experiments have allowed to characterize the effect of the modulation in the symbolic dynamics. The clusters of ordinal patterns formed without forcing remain under external periodic forcing. The minimal model has been verified, as it reproduces satisfactorily the symbolic dynamics of the experimental data.

Also, in this *Thesis* a technique has been developed to detect displacements of two independent objects at subwavelength resolution ($\lambda/160$). With this purpose, a setup has been developed with a semiconductor laser with dual feedback. In addition to the high resolution, this protocol offers the advantage of sensing two objects by just measuring one variable.

Agradecimientos

Tienes en tus manos el resultado del trabajo de investigación que he llevado a cabo en el campo de la dinámica no lineal de láseres en los últimos cuatro años. Personalmente, me siento muy orgulloso de mi pequeña aportación a la ciencia y espero que disfrutes leyéndola tanto como yo he aprendido y disfrutado escribiéndola.

Obviamente, como casi todos los proyectos humanos, se trata de un proceso no lineal y altamente complejo, en el sentido más científico de la palabra. En este trabajo han intervenido muchos elementos, ha habido interacción con muchas personas, feedback, ruido y forzamiento externo; así como memoria del camino previo recorrido y anhelos sobre el futuro por recorrer.

Estamos en el siglo XXI y ahora la ciencia no es cosa de personas aisladas y encerradas en sus oscuros laboratorios. Galileo Galilei, Isaac Newton, Henry Cavendish o Michael Faraday pertenecen a otra época de la historia de la ciencia; ahora la ciencia es colaborativa y apenas hay logros individuales. Esta tesis doctoral es un claro ejemplo de ello, pues no hubiese visto la luz sin la implicación de muchas personas que, tanto en el ámbito científico, como en el ámbito personal y humano, me han servido de inspiración, orientación y ayuda, así como de soporte personal y emocional.

A todos ellos debo mi más sincero agradecimiento.

Mis directoras de tesis: Incuestionable e imprescindible ha sido en mi aprendizaje la labor de Cristina Masoller y Maria Carme Torrent. Ellas me han abierto las puertas a un mundo que creía lejano: la investigación de primera línea. Con ellas he aprendido, discutido, me he emocionado y me he hecho muchas preguntas a lo largo de estos cuatro años, es decir, he hecho ciencia. Gracias, Cristina, por creer en

mi y apostar por alguien con un perfil tan poco ortodoxo para hacer un doctorado. Gracias a ambas también por la paciencia cuando los resultados no llegaban y por valorarme cuando sí lo hacían (mérito de todos).

DONLL: Ramon Vilaseca y Jordi García Ojalvo fueron también artífices de que yo entrase en el grupo de dinámica y óptica no lineal y láseres de la UPC, clave para que puedas leer esta tesis en estos momentos. La oportunidad de hacer ciencia en este grupo de investigación no se tiene todos los días: estimulantes discusiones sobre ciencia todos los días, reuniones y labmeetings donde siempre se aprende algo. Pero el grupo está formado por personas, personas de gran valía tanto científica como humana, como el propio Ramon, cuya manera de entender la ciencia y de expresarla en términos sencillos ayuda a amar más la ciencia, o Jordi, fuente inagotable de ideas que despiertan en uno las ansias por investigar y formularle preguntas a la naturaleza. Toni Pons, que como científico, profesor y persona, sus comentarios me han aportado frescas y profundas ideas; Crina Cojocaru, una estupenda compañera en las aulas, con quien comparto muchos puntos de vista; Josep Lluis Font, por que disfruto y me esmero en mi labor docente, me alegro de haber estado cerca de ti para aprender a ser mejor (gracias por tus palabras de ánimo). Ramon Herrero, Josep Trull, Muriel Botey, Kestas Staliunas, siempre es estimulante escucharos e intercambiar opiniones. Cómo no, Dani, Ignacio, Sandro, Giulio, Simone, Carlos, Taciano, Auro, Lina, y antes Jordi Z., Jordi T., Belén, Pau, Vito, Marta, Lorena y Elena, esos cafés en la Pastisseria acompañados por conversaciones sobre láseres, copmplejidad, docencia, Einstein, Sheldon Cooper o política científica, han ido dando forma a los logros de esta tesis. Gracias por vuestra ayuda con la programación. Cristina M., siempre has estado ahí cuando me he atascabdo en el laboratorio, has supeusto una gran ayuda.

DFEN: Estos cuatro años han sido posibles por que, desde un punto de vista administrativo, Josep Lluis Tamarit, Jordi José y Josep Trull apostaron por mi y me aceptaron como profesor ayudante del DFEN.

Duke University: Having the opportunity to work for three months with professor Daniel J. Gauthier has been, from the scientific and personal point of view, very fruitful, as I have learnt a lot in your lab, under your guidance. The experience, operativeness and working capability of Seth D. Cohen, the valuable advice of prof. Gauthier and the estimulating talks with Damien Rontani, Kristine Callan and David

Rosin contributed significantly in making me better scientist.

DILAB: Aún recuerdo la entrevista para el puesto de profesor asociado en la cual, la potente voz y el semblante serio de Belana imponiéndo respecto, escondían a una gran persona que más adelante me invitaría a hacer investigación con él y su grupo, que representaría un importante paso previo a esta tesis. También recuerdo muy gratamente los años de investigación y los consejos de Miguel, el rigor científico con una visión políticamente correcta. Jordi Òrrit, Jordi Sellarès, José Antonio Diego, Juan Carlos Cañadas, Idalberto y Alexander, gracias por enseñarme a moverme en el laboratorio, aprendí y disfruté en el DILAB, desvelando el comportamiento de las cargas en los dieléctricos. Jaume, tanto los inventos del taller, siemper útiles para la ciencia, como los cafés con denuncia política, siempre útiles para el ánimo, han ayudado a retomar fuerzas.

Divulgación científica: Creo que los cieníficos tenemos la obligación de facilitar que nuestra ciencia llegue a la sociedad, bien sea comunicándola directamente o bien haciendo que otros la comuniquen de manera asequible. También pienso que mi labor divulgativa de estos años ha servido de inspiración en momentos de esta tesis. Recuerdo los consejos que me dieron Tamarit, José y Trull cuando me aceptaron como ayudante del DFEN, pero ha sido inevitable. Además la situación socioeconómica ha hecho que mi universidad (aquí no entro a valorar quien mató a quien) me ha negado una catorceava parte de lo prometido (ya justo de por sí), impulsándome a intensificar mi labor extra-académica (primero el estómago y después la filosofía) con la consiguiente compensación en lo material y satisfacción en lo personal. Aquí también agradezco la paciencia y comprensión de Cristina y Carme, pero ha supuesto un balón de aire fresco en los momentos difíciles.

Cesca, es un placer explicar ciencia a los más jóvenes, estimularles y mostrarles la importancia de la ciencia en nuestra sociedad; creo que es una labor muy necesaria (algunos de estos jóvenes estarán en nuestros laboratorios en unos años: feedback con time delay). Planeta da Vinci, significas mucho y mucha gente te valora, hacen falta proyectos así. Toni Hernández, Isaac Camps, ha sido un placer contribuir en que nuestros jóvenes tengan una buena base en matemáticas, a parte de un estímulo y un honor escribir los libros de texto. Pasar de la dinámica simbólica a las ecuaciones de segundo grado ayuda a mantener ágil el cerebro. Toni, tu paso por el DFEN fue

breve pero intenso, eres una fuente de ideas e inspiración.

Triginer, en su día no llegamos a compartir despacho como doctores, pero hablar de ciencia y sociedad contigo ha dejado huella en mi formación como científico, persona y ciudadano.

Mariona, no sé si como modernistas tenemos mucho futuro o no, pero el hacer El Submarí todas las semanas ha supuesto una válvula que me ha oxigenado y ha mantenido ágil mi capacidad comunicativa. Además de disfrutar transmitiendo para que otros aprendan, también he aprendido a transmitir, fundamental para un científico, y ha resultado fácil y ameno estando tú en el otro micrófono.

Papá, mamá, ¿os acordáis de aquel flan que se cayó en el bar del instituto allá por 1988? Yo sí. ¿Os imagináis la de chistes que podréis hacer con un doctor en casa? En cualquier caso, gracias por estar ahí en todos los momentos.

Egara, Teresa, sobran los motivos y no los voy a enumerar aquí, no hay espacio. En cualquier caso, Egara, ha sido muy interesante escuchar tus ideas sobre experimentos con láseres acoplados, y tus sugerencias para el laboratorio. Además tus anotaciones en la pizarra del despacho siempre me han acompañado, manteniendo tu presencia en mis duros momentos de cálculos.

Teresa, siempre se aprenden cosas, sea de la mano de Richard P. Feynman o de la persona que tienes a tu lado, pero de esta última además obtienes apoyo, comprensión y calor vital para mejorar como persona y poder seguir navegando y llegar a buen puerto, por lo tanto, el mérito es también tuyo.

Que la ciencia te acompañe

Contents

Part I: Introduction

If I have seen further it is by standing on the shoulders of giants.
Isaac Newton

Five decades have elapsed since the first laser was buit [1, 2]. At that time (1960) the laser was considered *'a solution looking for a problem'*, but since then, it has dramatically changed our technological society. Hundreds of applications for the laser have emerged, while thousands of millions of dollars are generated by the laser industry.

The first laser was a rubi laser, and since then many different types of lasers have been developed: chemical lasers, dye lasers, solid-state lasers, metal-vapor lasers, semiconductor lasers, free electron lasers, etc. [3, 4]. Semiconductor lasers have become the most widespread type of laser (more than 90% of the lasers fabricated every year). Because they cover a wide range of wavelenghts (0.4 μm to 20 μm), powers (from mW to kW) and they are suitable for many applications (telecommunications, CD, DVD, Blu-ray, printing, pointers, barcode readers, gas sensors, surgery, material processing, pump sources for solid state lasers and optical amplifiers, etc.).

Besides their direct applications in our society, semiconductor lasers have been shown to be relevant devices in the research of dynamical systems. One interesting aspect of semiconductor lasers is that they are easily perturbed through optical injection, optical feedback, electro-optical feedback, or pump current modulation. These perturbations induce instabilities in the output intensity of the laser, which can result in a wide range of dynamical regimes, including periodic behavior and broad band chaos [5–8]. One situation that induces complex dynamics in a semiconductor laser is by submitting the laser to external optical feedback from a reflecting surface.

This thesis aims to investigate experimentally the dynamics of a semiconductor laser induced by optical feedback in two directions: on one hand, to exploit the laser's complex dynamics for improving the understanding of nonlinear and stochastic dynamical systems, and on the other hand to exploit the laser's complex dynamics for finding new technological applications that exploit the laser's complex dynamics.

Chapter 1

Stochastic complex systems in nature

Lisa, in this house we obey the laws of thermodynamics!
Homer Simpson (The Simpsons)

1.1 Introduction

Nature presents many fascinating complex systems. These systems are constituted by numerous elements that interact with each other, leading to collective emergent phenomena that can not be explained by analyzing its elements individually. Examples of complex systems are the human brain, cellular networks, insect populations, the climate, the stock market, social networks, car traffic, and earthquake activity, among many others [9]. These examples of complex systems might seem to be disconnected from each other, as they refer to very different aspects of nature and social behavior. However, they share common underlying characteristics, as they can all be studied with the same perspective and the statistical tools developed by the complex systems community. Therefore, some results obtained from one complex system might be extrapolated for a better understanding of other systems.

Most complex systems in nature share the following three basic ingredients: they are nonlinear (i.e., the output of the system is not directly proportional to the in-

put), noise is present in the system (random fluctuations of some of the variables of the system, as well as observational noise, are unavoidable), and the information propagates at a finite velocity, giving rise to time-delayed interactions. In addition, the lack of full information about state of the system (one can measure only one or a few relevant variables, and with a limited spatial and/or temporal resolution) makes identifying signatures of determinism very complicated, and a hot topic of research nowadays [10–19].

In many systems, the dynamics can be described through sequences of events (sequences of neuronal spikes, of heart beats, earthquake times, etc.). A successful approach for studying such systems is by focusing on an event-level description of their dynamics, considering, for example, intervals between consecutive events.

1.2 Semiconductor lasers with optical feedback as stochastic complex systems

In photonics, a clear example of a system producing a sequence of spike-like events is a semiconductor laser with optical feedback. Under specific conditions (which will be explained in detail in *Chapter 2*), the laser can present sudden irregular dropouts of its output intensity, followed by slow recoveries (see Fig. 1.2). This dynamical regime is referred to as *Low Frequency Fluctuations* (LFF) and, it has attracted a great deal of interest over the last three decades [20–35], it is not fully understood.

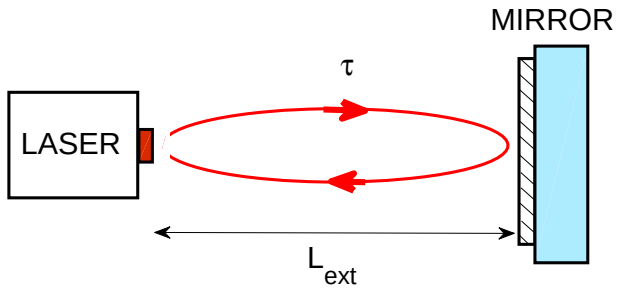

Figure 1.1: (a) Scheme of a semiconductor laser with external optical feedback. The emitted light is reflected by a mirror placed at a distance L_{ext}, and it takes a time $\tau = 2L_{ext}/c$ to make the round trip, where c is the speed of light.

As will be discussed in *Chapter 2*, a semiconductor laser can be described by two coupled differential equations [5], that describe the time evolution of the photon density and the carrier density in the active region of the laser. These equations only allow transient relaxation oscillations, but the inclusion of optical feedback can lead to complex dynamics. When part of the laser's emitted light is re-injected, by means of a reflecting surface, the light needs time to travel from the laser to the reflecting surface and back to the laser, and this introduces a delay time that enables high-dimensional dynamics (see Fig. 1.1).

Specifically, the output intensity of a semiconductor laser with optical feedback can display high and low dimensional chaos [36, 37], intermittency [38], quasiperiodicity [39], period doubling [40], bifurcation cascades [41], etc. This sensitivity to external perturbations makes the semiconductor laser an attractive device from the basic's research perspective, as it is an excellent tool to study complex dynamics, and in particular the dynamics induced by time-delayed feedback. Because of this wide range of dynamical possibilities, semiconductor lasers with optical feedback provide a controlable experimental setup to understand these phenomena, which can be found in many natural systems.

Also from the practical applications perspective, a semiconductor laser with optical feedback is very relevant: on one hand, the induced perturbations might be seen as a nuisance for a proper operation, where spurious reflections can lead to unavoidable optical feedback, which degrades the laser performance in telecommunications, data storage or reading, etc. Therefore, understanding and controlling the feedback induced effects is crucial in a wide range of laser applications. On the other hand, improving our knowledge of feedback-induced dynamics, can lead to new applications of semiconductor lasers, as will be discussed in *Chapter 2*. Nowadays, semiconductor lasers with optical feedback are being used for reservoir computing, a novel neuro-inspired computation method [42–44]. They are also used for random number generation [45, 46], as well as for chaos-based telecommunications [47].

As discussed before, the LFF is a feedback induced regime that has attracted a lot of attention since it was forst reported [20]. From the point of view of complex systems, this spiking regime is relevant because many natural systems show similar spiking behavior.

(a)

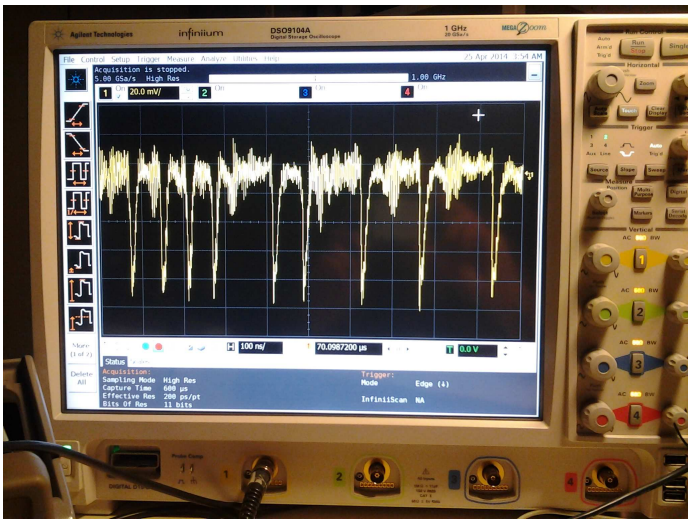

(b)

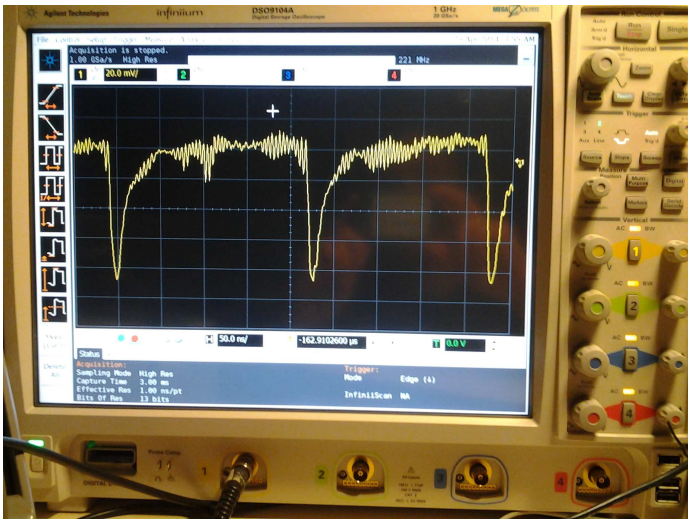

Figure 1.2: (a) Time trace of the intensity of a semiconductor laser in the LFF regime, acquired with a 1 GHz bandwidth oscilloscope (Agilent, DSO9104A). The output intensity of the laser presents sudden, irregular dropouts, followed by slow recoveries. (b) A detail of the sharp drops followed by slow recoveries. This *Thesis* focusses in studying the statistics of the time intervals between consecutive dropouts, which will be referred to as *inter-dropout intervals*, or IDIs. The analysis will be performed using a symbolic methodology, referred to as *ordinal analysis*.

Another dynamical regime, which can be observed in a semiconductor laser with optical feedback is the quasi-periodic (QP) regime. This QP behavior arises when a dynamical system is ruled by two, or a few, frequencies which are incommensurate.

This *Thesis* focuses in these two dynamical regimes of semiconductor lasers with optical feedback. They are used to improve our knowledge of complex systems, and to develop a novel technique for subwavelength position sensing.

1.3 Overview of the thesis, objectives, chapter summaries and main results

The main objectives of this *Thesis* are twofold: first, to study the nonlinear dynamics of a semiconductor laser with external optical feedback, in the LFF regime, to improve our understanding of stochastic complex systems. In this direction, this work focuses on distinguishing signatures of stochasticity and determinism from observed time series; unveiling hidden statistical features in the LFF dynamics; comparing with the predictions of a well known model; and finding a minimal model that describes the dynamics. Second, to exploit the quasi-periodic regime for a novel application, specifically, for two-dimension subwavelength position sensing.

This *Thesis* presents experimental results, numerical simulations, and data analysis. Most of the work has been done in the laboratory of the DONLL research group (Dinàmica i Òptica No Lineal i Làsers), at UPC in Terrassa (Spain). The experiments presented in *Chapters 4* and *5*, and the simulations of the circle map model, presented in *Chapters 5* and *6* were performed by the author of this *Thesis*. The experiments on modulation, presented in *Chapter 6*, were performed by the author and Taciano Sorrentino. The simulations of the LK model (*Chapters 5* and *6*) were performed by Sandro Perrone. The experiments and data analysis on subwavelength position sensing (*Chapter 7*) were performed by the author and Seth D. Cohen in the laboratory of Professor Daniel J. Gauthier (Duke university, North Carolina, USA).

The *Thesis* is organized as follows:

In *Chapter 2*, the dynamics of a semiconductor laser with optical feedback is

described. In particular, the LFF regime is described, as it is the dynamical regime investigated in *Chapters 4* to *6*. Typical experimental features and the details of a well established model, the Lang & Kobayashi model (LK) model, are also presented.

Chapter 3 describes the method of symbolic analysis used to study the LFF regimes. This analysis method transforms the time series of inter-dropout intervals into ordinal patterns, and it is used in chapters *Chapters 4* to *6* to characterize the complexity of the LFF dynamics. Other analysis methods are presented, and the advantages and drawbacks of the ordinal symbolic analysis are discussed.

In *Chapter 4*, ordinal analysis is used to distinguish signatures of determinism and stochasticity in the LFF dynamics. It has been an open question since the LFF discovery, whether they are noise-induced stochastic instabilities or triggered by deterministic processes. The study presented in this chapter allows to statisticaly determine which dropouts are consistent with a stochastic process and which have signatures of a deterministic one.

In *Chapter 5*, ordinal analysis is employed to unveil a symbolic structure hidden in the LFF dynamics. A clustered hierarchy of ordinal patterns is found, which is a signature of an underlying attractor topology, and serial correlations among several consecutive dropouts are uncovered. Moreover, a minimal model is found, a modified circle map, that mimics the LFF symbolic dynamics. This minimal model has been previously used to describe the neural activity of sensory neurons of paddlefish [48]. This suggests that semiconductor lasers with feedback could be used to simulate neural activity, as if they were optical neurons. From this perspective, yielding new light into the spiking, high-dimensional and stochastic LFF dynamics can improve our understanding of sequences of neuronal spikes, or other spiking real-world systems. Also, the ordinal analysis is used in this chapter to verify the validity of the LK model in an unprecedent long time-scale, as serial correlation among several consecutive dropouts are also found in the simulations of the LK model.

Chapter 6 is devoted to analyze the LFF dynamics of the laser under external periodic forcing. The response to a direct sinusoidal modulation of the bias current is studied, by employing the ordinal analysis. This forced situation is of special interest, not only because the LFFs can be suppressed via current modulation [49, 50],

but also, from a complex systems perspective, because the interplay of nonlinearity, noise, and periodic forcing leads to entrainment and synchronization, providing a controllable experimental setup for studying these phenomena. In addition, because the LFF dynamics is excitable [25, 32, 51], the influence of external forcing has also attracted attention from the point of view of improving our understanding of how excitable systems (like neurons) respond to external signals to encode information. The LK model is also analized considering the external forcing, finding a good qualitative agreement with experiments. Next, the modified circle map model is analyzed, and its suitability to describe the symbolic dynamics of the LFFs with pump current modulation is demonstrated.

Chapter 7 exploits the sensitivity of the multifrequency power spectrum of the laser in the quasi-periodic regime to perform two-dimensional (2D) subwavelength position sensing. In the literature, different approaches have been developed in order to detect subwavelength changes in the external cavity length of a laser with feedback, which use self-mixing interferometry (see [52] for a recent review). These laser-based approaches are restricted to 1D sensing or have the drawback that they need to perform scans to do 2D sensing. Here, an experimental setup consisting of a semiconductor laser with two external cavities is used to demonstrate 2D position sensing. Using a $\lambda = 1550$ nm wavelength laser, displacements of $\Delta x \sim 10$ nm are resolved ($\lambda/160$). With this setup, by measuring just one input (the power spectrum of the intensity) two independent displacements can be simultaneously measured with subwavelength resolution.

Chapter 8 presents the conclusions and future work as result of this research. Finally, a list of publications and conference contributions related with this *Thesis* is presented.

Chapter 2

Dynamics of semiconductor lasers with optical feedback

Yes, in 1917 when Albert Einstein established the theoretic foundation for the laser in his paper "Zur Quantentheorie der Strahlung," his fondest hope was that the resultant device be bitchin'.

Sheldon Cooper (The Big Bang Theory)

2.1 Introduction

In 1917 Albert Einstein predicted that a photon, interacting with an exited atom, could stimulate the emission of a second photon by this atom, being the latter identical to the former [53]. It was not until 1954 that Gordon, Zeiger and Townes developed the first maser [54], by amplifying the electromagnetic radiation in the microwave frequency region. This paved the way for the Light Amplification by Stimulated Emission of Radiation (LASER), the first laser, which came into reality in 1960 [1, 2]. Since then, an explosion of different types of lasers has followed. In particular, in 1962 different groups demonstrated the first semiconductor laser [55–58].

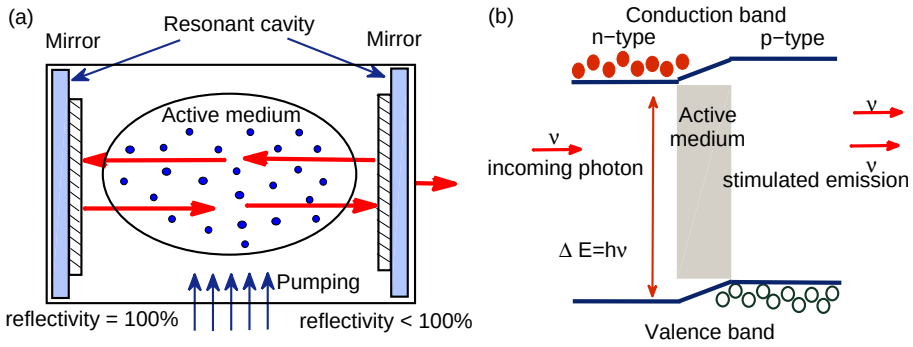

Figure 2.1: (a) Schematic representation of a laser. Light excitates the active medium inside the cavity. The mirrors make the photons to go back and forth, amplifying the stimulated emission. (b) Schematic representation of the stimulated emission process, where a photon induces a electron-hole pair to recombine, by emitting a photon identical to the former.

2.1.1 The laser operating principles

Most lasers are formed by an active medium in a resonant cavity (see Fig. 2.1). The active medium consists of a collection of atoms, molecules, or ions, which have several energy levels or energy bands. When these particles are in an excited state, they can decay to a lower energy state by emitting a photon. In semiconductor lasers, the active medium is a p-n junction of a semiconductor diode (therefore also called laser diodes), where recombination of electrons from the conduction band, and holes from the valence band (charge carriers) induces light emission. This process is due to spontaneous and stimulated emission.

When a direct voltage is applied to the p-n junction, the electrons are in the conduction band and the holes are in the valence band. At this stage, when a photon passes through the medium (initial photons proceed from quantum spontaneous emission noise) it stimulates the electron-hole recombination, emitting a second, identical photon. The identical features of all photons refer to the same wavelength, phase, polarization, and propagation direction. The frequency, ν, of the emitted photons is related to the energy difference of the electron-hole pair ($\Delta E = h\nu$, where h is Planck's constant). That is why only a range of photon frequencies can induce this process.

To sustain the stimulated emission, the medium is placed in a cavity with mirrors

at its ends (free electron lasers, random lasers, or distributed feedback lasers do not require a resonant cavity, but these lasers are not studied in this *Thesis*). In semiconductor lasers the medium facets constitute the cavity. These mirrors reflect the emitted photons and make them go back and forth in the cavity, amplifying the process. The size and design of the cavity also select the modes (frequencies) that can lase: for constructive interference inside the cavity, the wavelength of the photons has to be a sub-multiple of the cavity length (this set of eavalengths is referred to as longitudinal modes).

By making one of the ends of the cavity slightly transparent, light (highly monocromatic and coherent) can escape the cavity. When the gain in the cavity is larger than the losses (by absorption and cavity losses), the laser reaches its threshold and begins lasing.

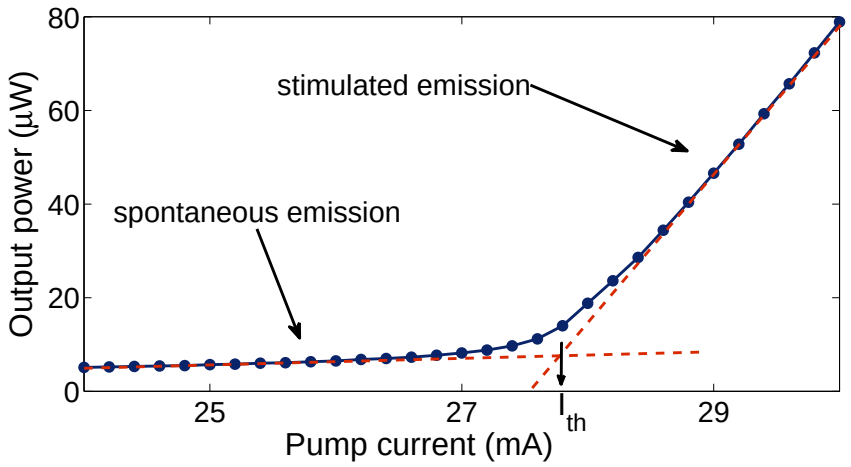

Figure 2.2: Output power vs. pump current of a laser diode. When the gain is larger than the losses the system begins to lase, this happens at the threshold, indicated with an arrow (27.8 mA in this case). The laser used is a 675 nm AlGaInP semiconductor laser (Hitachi Laser Diode HL6724MG).

Figure 2.2 shows the output power of the laser vs. the pump current (also referred to as light vs. current characteristic, or L-I curve). For pump currents below the threshold, the output power (due to spontaneous emission) hardly increases with the pump current. Above the threshold (at 27.8 mA in Fig. 2.2) there is a sharp increase in the the output power, then presenting a linear dependence on the pump current.

2.1.2 Characteristic features of semiconductor lasers

Relaxation oscillations. When a laser diode is switched on, the carrier density (i.e., pairs of electrons and holes) increases at a finite rate, which implies a delay in the laser switch on [59]. The nonlinear coupling between photons and carriers results in transient oscillations, referred to as relaxation oscillations [5]. Figure 2.3 shows the optical output of the laser when it is subject to a step-like pump injection. The frecuency of the relaxation oscillations increases with the pump current. Due to the characteristic life-times of the carriers and the photons (10^{-9} s and 10^{-12} s, respectively) the relaxation oscillation frequency is of the order of a few GHz.

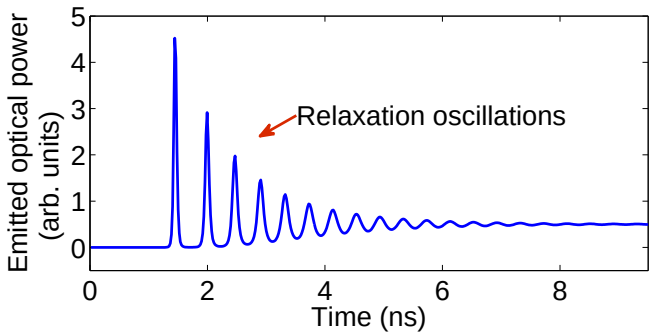

Figure 2.3: Emitted optical power of the laser subject to a step-like pump current at time = 0 ns. Simulations of the rate equations presented in *Section 2.4* with parameters: $\tau_p = 1$ ps, $\tau_n = 1$ ns, $\mu = 1.5$, $\beta = 10^{-4}$.

Thermal effects. Depending on the pump current, thegeometry and the dimensions of the cavity, a laser can emit in one or a few longitudinal modes (referred to as single-mode or multi-mode laser, respectively). When a semiconductor laser is switched on, and for low pump currents, it often emits several longitudinal modes, but, as the pump current is increased one mode dominates the emission. The emission modes depend, not only on the pump current, but also on temperature. Changes on temperature affect the refractive index of the active medium and, as consequence, they produce a shift in the frequencies of the cavity modes. An increase in temperature induces a reduction of the band gap in the active medium, and therefore, also a shift of the maximum gain of the active medium, which results in a shift of the emission modes towards longer wavelengths [60].

Figure 2.4 shows the optical spectrum, normalized to the maximum intensity, of a multi-mode laser for three pump currents (low to high from left to right).

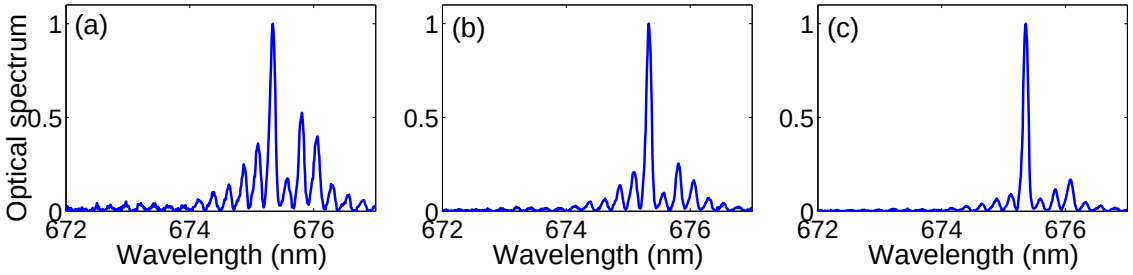

Figure 2.4: Normalized optical spectrum of a semiconductor laser of nominal wavelength of 675 nm (Hitachi Laser Diode HL6724MG) at three pump currents: (a) 29.10 mA, (b) 29.70 mA, and (c) 30.30 mA.

Another thermal effect that occurs at high pump current is due to Joule heating and results in gain saturation

Amplitude-phase coupling and linewidth enhancement. In a semiconductor laser, the refractive index depends on the carrier density in the active medium, which in turn varies with the photon density. This results in a coupling of phase and intensity fluctuations, which broades the linewidth of the laser. It is phenomenologically represented by the α-parameter or linewidth enhancement factor [21].

2.2 Applications of semiconductor lasers

Since 1962, different semiconductor materials have been used as active medium to obtain lasing emission. Depending on the semiconductor material, the optical wavelength of the emitted light goes from infrared to ultraviolet. This, and the wide range of output powers attainable (from milliwatts to kilowatts), make semiconductor lasers suitable for many applications, for scientific and for commercial purposes.

Laser diodes aer used for optical information processing. Information can be coded in a sequence of zeros and ones. The tracks on CDs, DVDs, or blue-rays are written with sequences of dark-bright patches. The light from a semiconductor laser scans these tracks recognizing the reflectivity of every patch (if it reflects light, then it is a 'one', otherwise it is a 'zero'). The amount of information that can be stored

depends on the resolution to read it, which is directly related to the wavelength of the light (the wavelength used for CDs is of 780 nm, for DVDs 650 nm, and for blue-rays 405 nm), which in turn is inversely proportional to the storage capacity of the disk (one CD can store 0.7 GB, while double-sided DVDs can store 9.4 GB, and double-sided bue-ray 50 GB).

Another use of semiconductor lasers can be found in medicine and biology. In surgery, they represent a source of heat that cuts organic tissues, as a scalp, based on the phototermal interaction of laser light with the main components of the extracellular matrix of specific tissues [61]. They can also be used for single particle tracking techniques to explore biomolecules dynamics in live cells [62].

The field where laser diodes are of most importance is in telecommunications. Optical fibers are glass filaments, made basically of silica, that have a minimum of absorption of light at around 1550 nm wavelength, and also at around 1310 nm wavelength. Telecommunications through optical fiber use semiconductor lasers operating at these wavelengths, and provide transmission rates up to several tens of gigabytes/s. Because semiconductor lasers are unexpensive, compact, energy efficient and reliable, they are the lasers used in fiber TV, local area networks (LAN), and to optically pump Erbium-doped fiber amplifiers used in long distance telecommunications.

In position sensing and distance measurements, semiconductor lasers are also very popular. By sending a modulated signal, detecting its reflection on a target, and comparing the phase of the emitted light with the reflected one, it can be measured the distance to the target with high resolution [63].

From the fundamental point of view, semiconductor lasers are relevant for understanding and investigating different phenomena of nonlinear systems.

Semiconductor lasers are described by two coupled rate equations, which do not manifest chaos by themselves, but semiconductor lasers are very sensitive to external perturbations (injection, modulation, optical feedback, etc.), that destabilize the laser output, and can drive the system to display highly complex nonlinear dynamics and bifurcations. This behavior openes a rich field of research, as diverse dynamical phenomena can be observed, like excitability [25], low frequency fluctuations [24, 64], coherence collapse [65, 66], synchronization [67], stochastic resonance, coherence

resonance or ghost resonance [68–71]. Therefore, semiconductor lasers with feedback are good testbed to improve our understanding of these phenomena.

These optical instabilities are seen as a nuisance for engineering performance, but a challenge from the fundamental science point of view.

One of the first applications of optical feedback in semiconductor lasers is the threshold reduction, as will be discussed in the next section. Optical feedback can also induce a narrowing of the linewidth, with clear advantages in optical communications [72].

Other applications, related to the feedback-induced chaotic dynamics, are found in chaotic secure communications [47, 73], as the high-dimensional dynamics can be used to encrypt information, embedded in a chaotic signal, and transmit it securely. Another application of laser dynamics is in the performance of chaotic radars [74], as the chaotic dynamics generated by a semiconductor laser can be used to achieve wide range high-resolution, secure detection. Chaotic semiconductor lasers also offer a fast and reliable way to generate random numbers [43, 45, 46], which is of great importance in numerical simulations, or in secure communications.

Recently, a novel computational method has been demonstrated, referred to as reservoir computing [75]. It is inspired in the way the brain processes and computes information. This concept takes advantage of the transient states that can be induced by a nonlinear system, and it can be performed by using a semiconductor laser network. The complex transient dynamics required in some of the experiments can be obtained with a laser (as nonlinear system), submitted to a time-delayed feedback [76, 77].

2.3 Semiconductor lasers with optical feedback

When a semiconductor laser is submitted to optical feedback, using a reflecting surface, it can present a wide range of dynamics. One of the first effects of optical feedback is on the laser threshold. Figure 2.5 depicts the dependence of the optical output of the solitary laser, without feedback (blue), and with three feedback levels (red, green and black), vs. the pump current. The vertical lines indicate the region where LFF dynamics takes place for the highest feedback level, corresponding to the

black L-I curve.

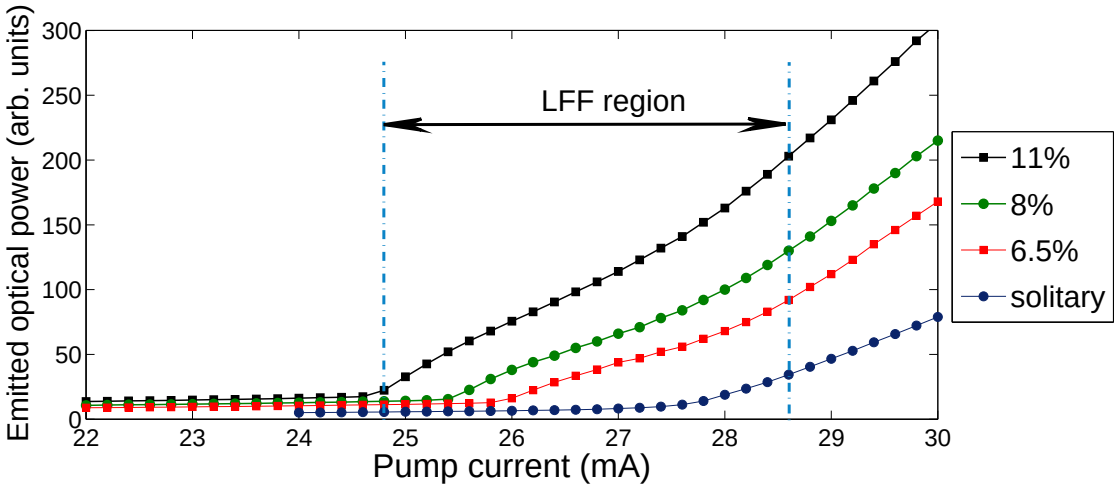

Figure 2.5: Effect of optical feedback in the lasing threshold. The laser starst lasing at lower values of the pump current. Three feedback strengths are plotted, corresponding to 6.5%, 8%, and 11% threshold reduction. The vertical lines indicate the region of pump currents where the LFFs take place for highest feedback case. The laser used is a 675 nm AlGaInP semiconductor laser (Hitachi Laser Diode HL6724MG)

The laser threshold is reduced by optical feedback (the light re-entering the laser cavity reduces the cavity losses and, thus, the threshold current). The stronger the feedback, the greater the threshold reduction. The amount of feedback can then be quantified by the reduction of the threshold pump current, as

$$\eta_{reduction} = \frac{I_{sol} - I_{fb}}{I_{sol}} \times 100, \tag{2.1}$$

where $\eta_{reduction}$ stands for the percentage of the reduction of the threshold, I_{sol} is the threshold of the solitary laser (without feedback), and I_{fb} is the threshold of the laser with feedback. The threshold reductions depicted in Fig. 2.5 correspond to 6.5% (red), 8% (green), and 11% (black).

A key parameter in the dynamics of a laser with feedback is the delay time, τ (the time needed by the light to do a round trip in the external cavity), determined by the cavity length. Figure 1.1(a) depicts schematically a semiconductor laser with external optical feedback. The delay time is

$$\tau = \frac{2L_{ext}}{c}. \tag{2.2}$$

where L_{ext} is the length of the external cavity and c is the speed of light.

Due to the relaxation oscillations of the semiconductor laser, the external cavity can be classified as *short cavity*, if the delay time is of the order or smaller than the relaxation time (of the order of hundreds of picoseconds) [64, 78]; or *long cavity*, if the delay time is much longer than the relaxation time [79]. The dynamics induced in these two regimes are qualitatively different. This *Thesis* is focussed on the long cavity regime, as the lengths of the external cavities in the experiments range from tens of centimeters to a few meters, which give delay times between 3 ns and 55 ns (one or two orders of magnitude greater than the period of the relaxation oscillations).

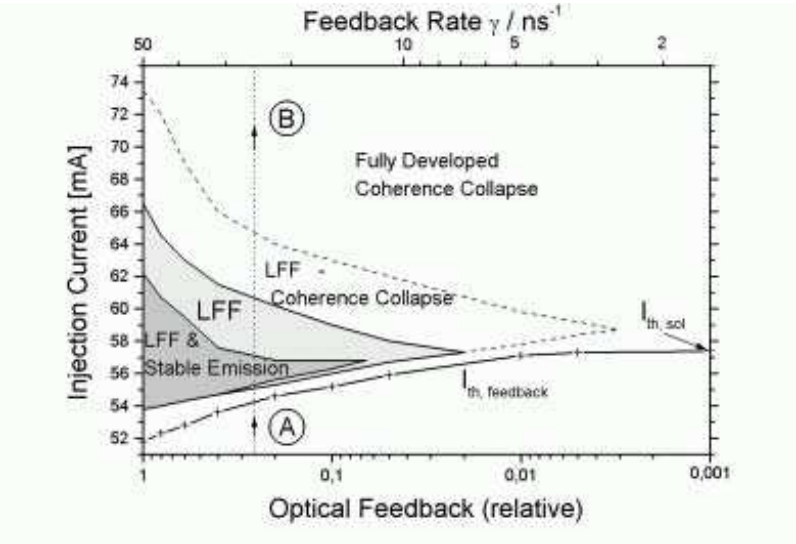

Figure 2.6: Dynamical behavior for a semiconductor laser with feedback in the injection current-feedback strength parameter space. Four regimes are indicated. Figure from Heil et al., Phys. Rev. A, **60**, 634, 1999 [66]. Feedback increases from right to left.

The dynamics that arises in this long cavity regime is high dimensional [80], and depends on several parameters. Figure 2.6 (taken from the work of Heil et al. [66]) maps the dynamics of a semiconductor laser with feedback, in the current-feedback space. For different parameter combinations, four regimes can occur: i) coexistence

of stable emission and LFFs, ii) LFFs, iii) coexistence of LFFs and coherence collapse, and iv) fully developed coherence collapse. The coherence collapse term refers to a large increase in the linewidth of the laser mode (from hundreds of MHz to tens of GHz). This regime occurs for moderate and for high feedback strengths, and pump currents well above the laser threshold (B in Fig. 2.6) [36, 38, 65, 81, 82]. Following the dotted line from A to B in Fig. 2.6 the system explores all four regimes. Of special relevance in this *Thesis* is the LFF regime.

2.3.1 The low-frequency fluctuations (LFFs) regime

For moderate feedback strengths and pump currents close to the laser threshold (as indicated in Fig. 2.5), optical feedback induces irregular dropouts with a mean inter-dropout interval of the order of hundreds of nanoseconds, that results in a peak in the power spectrum (see Fig. 2.7) with a frequency of the order of a few tens of MHz. These fluctuations (first observed by Risch et al. in 1977 [20]) have a longer time scale than the other time scales of the system, like the relaxation oscillations (smaller than nanoseconds for pump currents above the laser threshold) or the time delay due to the external cavity (nanoseconds to tens of nanoseconds). That is why they are referred to as low-frequency fluctuations (LFFs). Figure 2.7 shows the radio-frecuency (RF) spectrum of the dynamics of a laser with optical feedback. Two peaks are depicted, one about 20 MHz due to the LFFs, and another at about 250 MHz, due to the external cavity delay-time.

The LFFs consist of sudden dropouts of the laser intensity, followed by a slow recovery (of a duration of several delay times). After one dropout has taken place, the system recovers and then emits a nearly constant output power, until the next dropout takes place, as seen in Fig. 1.1, that depicts a time series in the LFF regime, recorded with a 1 GHz bandwidth oscilloscope and a time delay of 4 ns.

In fact, in this regime, the laser intensity manifests a fast pulsing dynamics, of the order of picoseconds, but due to the limitations of the experimental detection system in the laboratory, which has a limited bandwidth (1 GHz), it is only the envelope of the fast dynamics that can be observed. This fast dynamics is predicted by a rate equation model with delayed feedback (LK model, see *Section 2.4* for details), and was first observed experimentally by Fischer et al. in 1996 [24]. Figure 2.9, taken

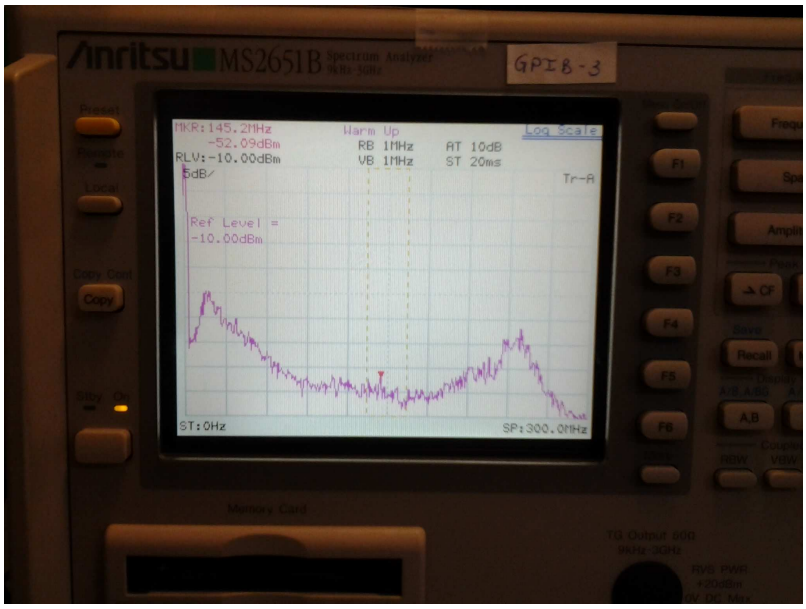

Figure 2.7: Power spectrum of the intensity of the laser, acquired with an RF spectrum analyzer (Anritsu MS2651B, 3 GHz). The photodetector used has a bandwidth of 2 GHz. The horizontal scale ranges from 0 MHz to 300 MHz. Two peaks are seen, at about 20 MHz, and at about 250 MHz. The first one corresponds to the LFFs, while the second one to the external cavity frequency.

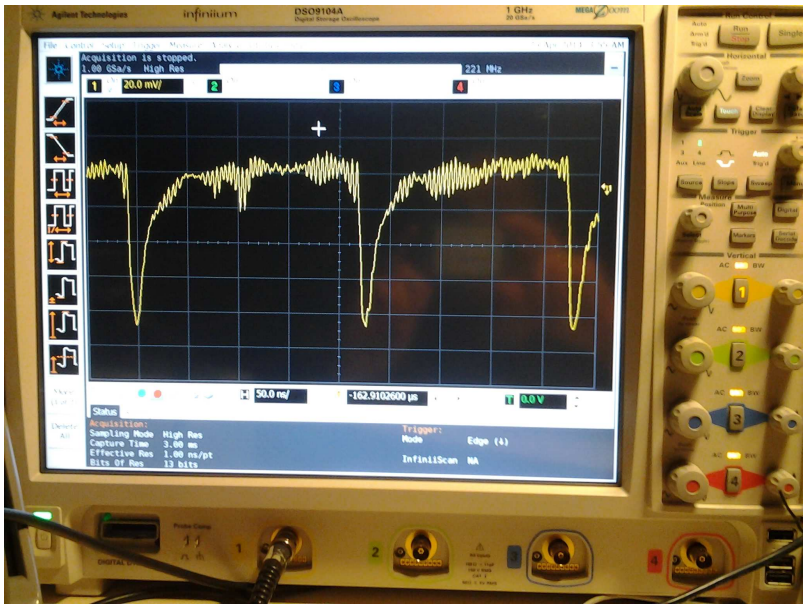

Figure 2.8: Output intensity of the laser in the LFF regime. Experimentally recorded with a 1 GHz bandwidth oscilloscope (Agilent DSO 9104A), for a time delay feedback of 4 ns.

from Fischer et al. [24], shows in the top panel the slow dynamics in the LFF regime, with the sudden dropouts and the inter-dropout intervals of the order of hundreds of nanoseconds, and in the bottom panel the fast pulsing dynamics, of a much faster time scale.

In this regime the laser can emit several longitudinal modes (optical frequencies). Indeed, all the experiments performed in this *Thesis* in the LFF regime are done with multimode lasers. Figure 2.10 shows the optical spectrum of a 675 nm wavelength laser without feedback (a, d), and with feedback (b, c, e, f), acquired with an Optical Spectrum Analyzer (Anritsu MS9710C). The figures of the top row correspond to low pump currents, and the figures of the bottom row correspond to higher pump currents. It can be observed that optical feedback induces the laser to emit in several longitudinal modes, equally spaced (Fig. 2.10(b,e)). By using a diffraction grating as external reflecting surface, almost single longitudinal mode emission can be achieved (Fig. 2.10(c,f)).

A common way of characterizing the LFF dynamics is by focusing on the inter-dropout intervals, i.e., the time intervals between two consecutive dropouts (IDIs). A

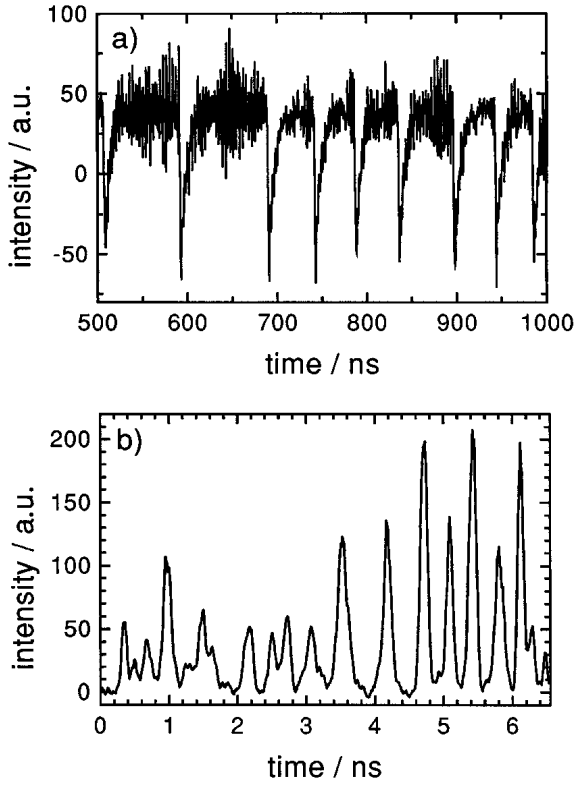

Figure 2.9: (a) Output intensity of the laser with feedback, where the LFF dropouts are observed. (b) Fast pulsing dynamics acquired with a fast streak camera. Figure from I. Fischer et al., Phys. Rev. Lett., **76**, 220, 1996. [24]

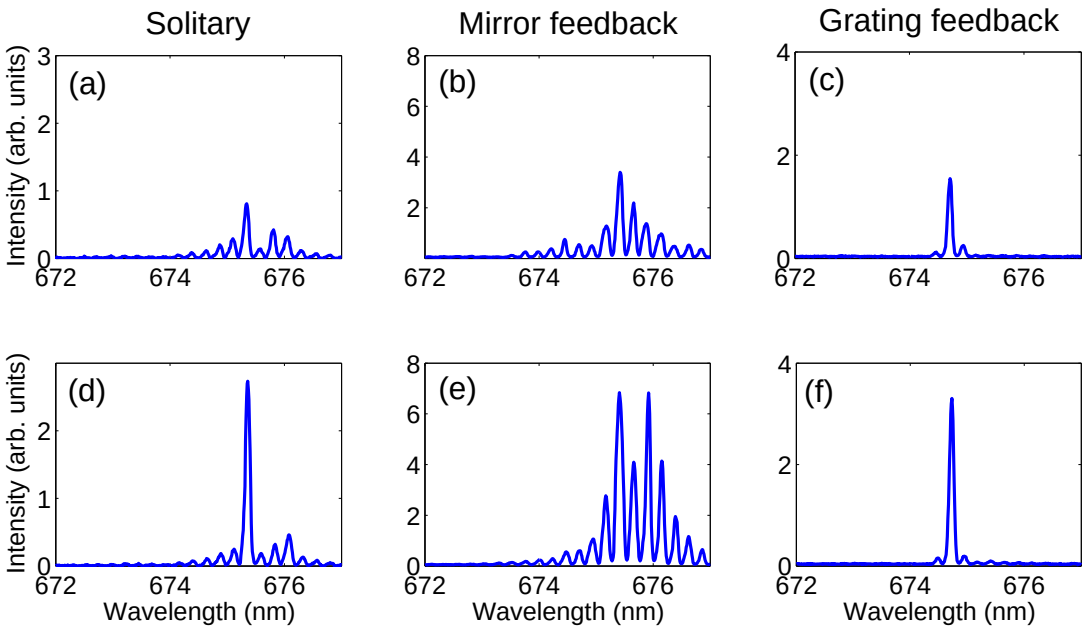

Figure 2.10: (a,d) Optical spectrum of a laser of a nominal wavelength of 675 nm, without feedback. (b,e) Optical spectrum of the laser with feedback from a mirror. (c,f) Optical spectrum of the laser with feedback from a difraction grating. Top row corresponds to low pump current. Bottom row corresponds to high pump current.

typical feature of the statistics of the IDIs is that, as the pump current is increased, the dropouts become more frequent and regular. Figure 2.11 depicts the experimental time series of a semiconductor laser with feedback in the LFF regime for two values of the pump current (top row), and the corresponding histograms of the inter-dropout intervals (middle row). It can be observed that the distribution of the IDIs presents a two peak structure for low pump currents, while it becomes narrower for high pump currents. Figure 2.11(e) displays the dependence of the mean inter-dropout interval, $\langle \Delta T \rangle$, with the pump current. $\langle \Delta T \rangle$ is depicted for the range of pump currents where the LFF dynamics takes place. In Fig. 2.11(f) the effect of the pump current on the normalized standard deviation ($\sigma / \langle \Delta T \rangle$) is depicted. There is a maximum in the dispersion of the IDIs at low currents, followed by a decrease of $\sigma / \langle \Delta T \rangle$ with increasing pump current.

2.3.2 Other dynamical regimes

As mentioned before, by following the vertical dotted line in Fig. 2.6 from A to B, four dynamical regimes can be explored (LFFs, coexistence of stable emission and LFFs, coexistence of LFFs and coherent collapse, and coherence collapse). For low pump currents the coexistence between the LFFs and stable emission is found. In this regime bursts of LFFs alternate with long times of stable, continuous emission. Once the system reaches a fixed point in phase space, it stays there until noise kicks it out, and a new burst of LFFs takes place. As the pump current is low, the system stays in the fixed point for periods of time longer than the LFF recovery time. Figure 2.12(a) shows the time trace of the laser in the coexistence regime between LFFs and stable emission.

By slightly increasing the pump current, the laser enters into the LFF regime. The interval between dropouts (ΔT) decreases as the pump current increases, as mentioned above. For large enough currents the dropouts are too frequent to be distinguished and there is a continuous transition to the fully developed coherence collapse [65]. Figure 2.12(b) depicts a time trace of the laser in the transition from the LFF regime to the coherence collapse regime.

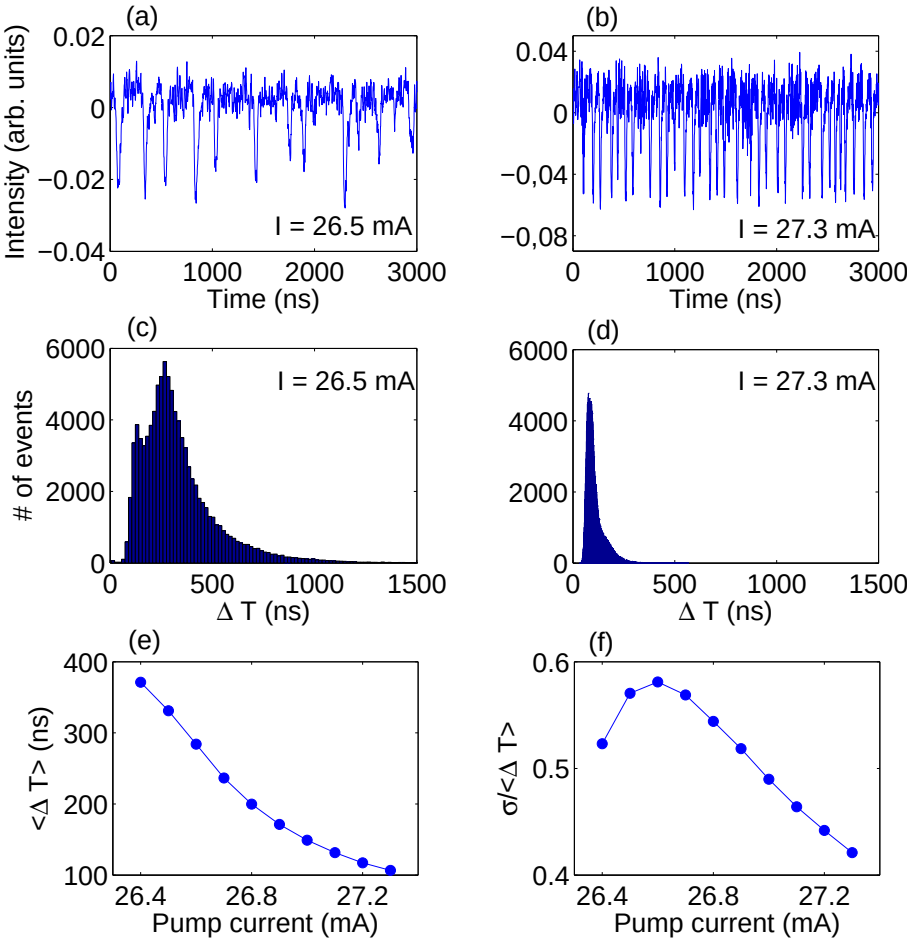

Figure 2.11: Experimental time trace of the laser (top row) in the LFF regime: (a) low pump current, I = 26.5 mA, (b) high pump current, I=27.3 mA. (c,d) Corresponding histograms. (e) Mean inter-dropout interval ($\langle \Delta T \rangle$) vs. pump current. (f) Normalized standard deviation ($\sigma / \langle \Delta T \rangle$) vs. pump current. These results are consistent with previous works [26, 27, 33, 70].

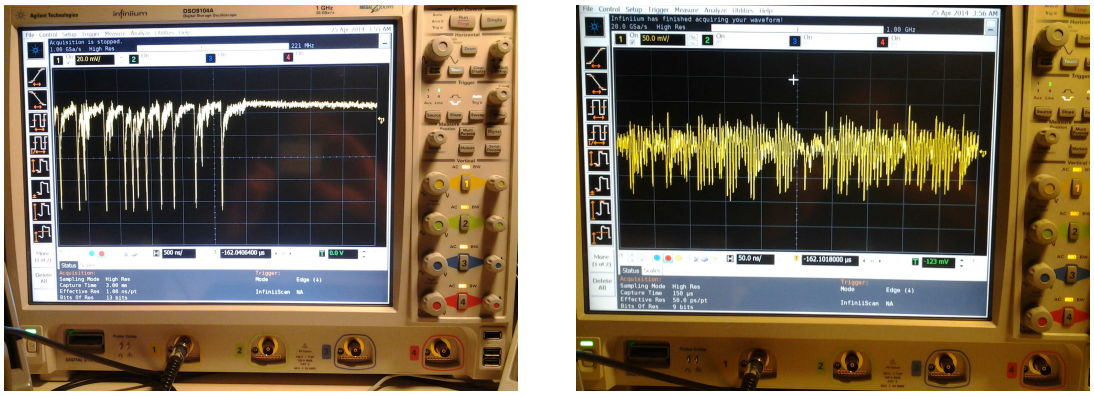

Figure 2.12: (a) Experimental time trace showing coexistence between LFFs and stable emission. (b) Experimental time trace in the transition from the LFF regime to the coherence collapse regime.

2.4 Modeling a semiconductor laser with optical feedback: the Lang & Kobayashi model

As mentioned before, semiconductor lasers can be described by two coupled rate equations [5, 60]. These equations describe the optical field, and the carrier density in the active medium of a laser.

In 1980, Lang and Kobayashi proposed a model to describe the behavior of a semiconductor laser submitted to optical feedback [83]. The Lang and Kobayashi (LK) model consists of two coupled delay-differential rate equations governing the evolution of the slowly varying complex electric field amplitude, E, and the carrier density, N. The model equations are:

$$\frac{dE}{dt} = \frac{1}{2\tau_p}(1+\alpha)(G-1)E + \eta E(t-\tau)e^{-i\omega_0\tau} + \sqrt{2\beta_{sp}}\xi, \tag{2.3}$$

$$\frac{dN}{dt} = \frac{1}{\tau_N}(\mu - N - G|E|^2), \tag{2.4}$$

where τ_p and τ_N are the photon and carrier lifetimes respectively. α is the linewidth enhancement factor, that describes the coupling between the amplitude and the phase of the electric field [21]. G is the optical gain, $G = N/(1+\epsilon|E|^2)$ (with ϵ being a saturation coefficient). It describes the gain saturation, due to hole burning or

carrier heating. μ is the normalized pump current parameter ($\mu = 1$ at threshold). η is the feedback strength, τ is the feedback delay time, $\omega_0\tau$ is the feedback phase, β_{sp} is the noise strength, representing spontaneous emission, and ξ is a complex uncorrelated Gaussian noise, with zero mean and unit variance.

The LK model makes strong simplifications with respect to the experimental situation. For the laser emission, it considers a single mode emission, while feedback often induces multi-mode emission (except in single-mode lasers). It also assumes the feedback strength to be weak or moderate, and neglects the effects of multiple round-trips of the light in the external cavity. It neither considers spatial effects, or thermal effects (in particular the shift of the emission wavelength with increasing current due to Joule heating). However, these effects have been included in extensions of the model [5].

Due to all these simplifications only a qualitative agreement with experimental observations could be expected, but surprisingly, the LK model describes to a great extent the dynamics of a semiconductor laser under a wide range of conditions: LFFs, coherence collapse, or coexistence of LFFs and continuous emission.

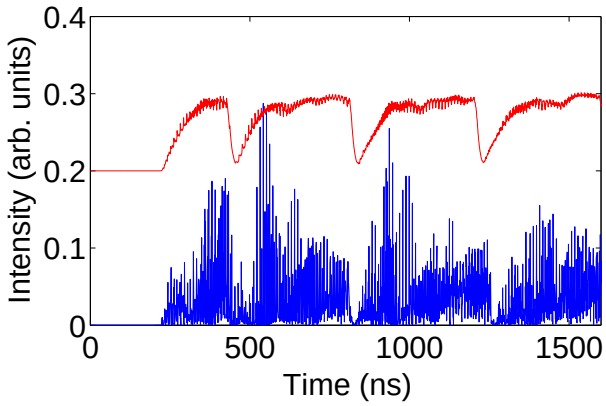

Figure 2.13: Time series simulated numerically with the LK model. The fast dynamics, of the order of picoseconds is shown in the blue trace, while the filtered signal, to account for the limited bandwidth of the experimental instruments, is depicted in red. The LFF dropouts can be observed in the filtered trace. The data are a courtesy of Carlos A. Quintero.

The LK model predicts the fast dynamics mentioned above, of the order of picoseconds, in the LFF regime. This can be observed in Fig. 2.13, where the fast

dynamics is plotted in blue and the filtered time series, the envelope of the fast dynamics that depicts the irregular dropouts, is plotted in red. Therefore, in order to take into account the bandwidth limitations of the experimental equipment, the time series obtained from the model simulations have to be filtered out.

Figure 2.14 is equivalent to Fig. 2.11 but obtained from numerical simulations of the LK model. Panels (a,b) show two typical time traces in the LFF regime, corresponding to two values of the pump parameter ($\mu = 0.98$ and $\mu = 1.02$, where $\mu = 1$ corresponds to the laser solitary threshold). Panels (c,d) are the corresponding histograms of the inter-dropout intervals, ΔT. (e) plots the mean ΔT vs. the pump current, and (f) depicts the normalized standard deviation, $\sigma/\langle\Delta T\rangle$, vs. the pump current. By comparing Fig. 2.14 with Fig. 2.11, a good qualitative agreement experiments-simulations can be observed in the statistics of the intervals between dropouts. The dependence with the pump current of $\langle\Delta T\rangle$ and $\sigma/\langle\Delta T\rangle$ is equivalent for the experiments and the numerical simulations [33, 70]. Also the histograms are in a good qualitative agreement [30, 84].

Even though, for low pump current in the numerical histogram (Fig. 2.14(c)) there is a sharp peak at low ΔT values, that is not seen in the experimental histogram (Fig. 2.11(c)). The reason of this peak is the presence of intermittent bursts of regular spikes (see Fig. 2.14(g)). This regular dynamics has been observed experimentally in the literature and has been referred to as *regular pulse packages* [64, 85, 86]. This phenomena can be avoided by the criterion to detect the dropouts (explained in detail in *Section 4.2*).

It has been a long debate whether the origin of the LFFs is stochastic or deterministic. A first explanation, due to Henry and Kazarinov [87], argued that they were caused by spontaneous emission fluctuations. They described the system in a potential well, that leaves it due to noise, then producing the LFFs. Another explanation [24, 88] suggested a deterministic origin for the LFFs. Sano [22] made an analysis of the trajectory in phase space, and found that the LFFs are caused by collisions of the trajectory with unstable fixed points. Further experimental and numerical analysis [23, 31] have shown that both processes, stochastic and deterministic, are required to explain the intensity dropouts in the LFF regime. Indeed, the dropouts, in deterministic simulations, are interpreted as a transient dynamics

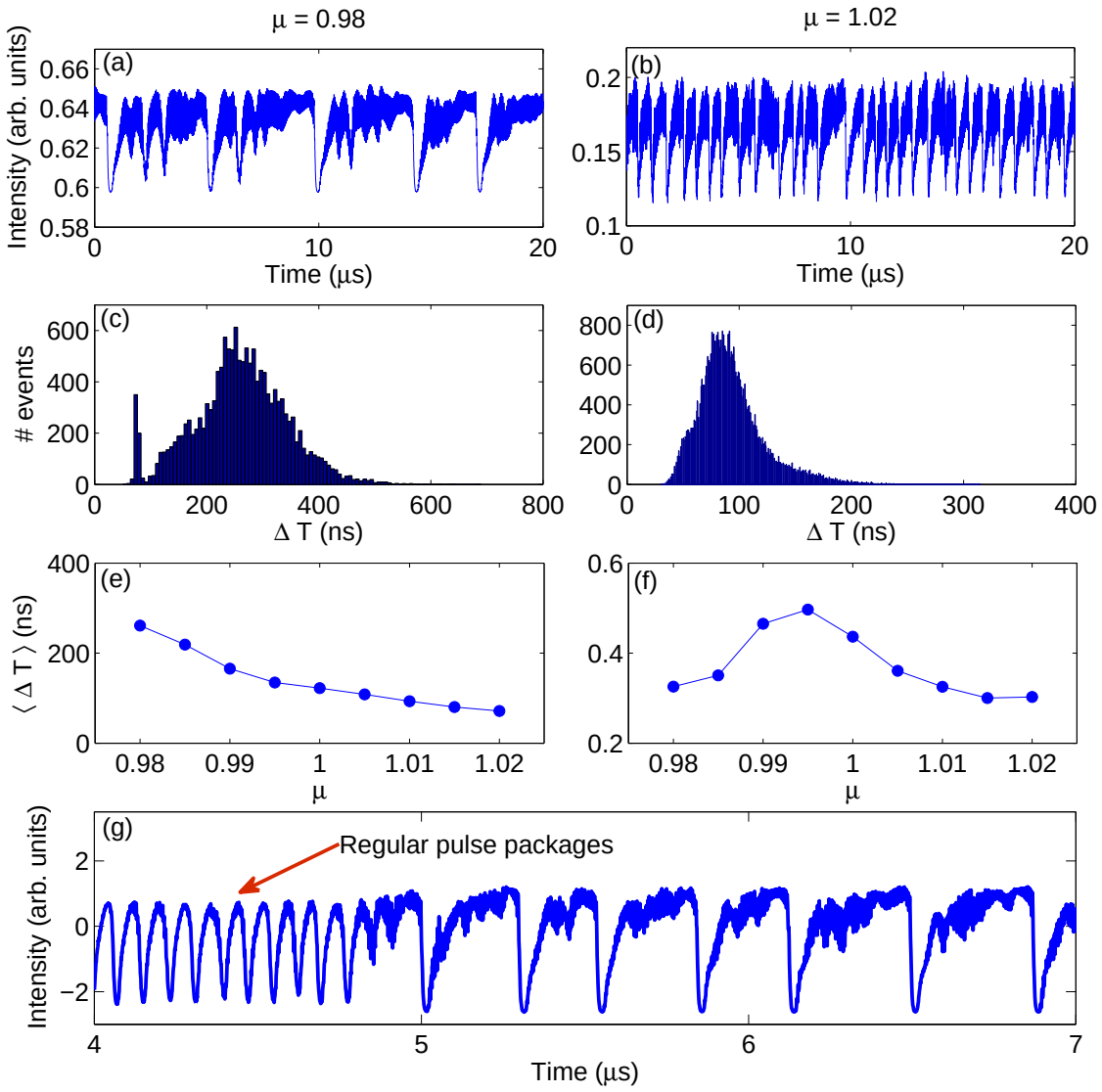

Figure 2.14: Numerically computed time traces of the laser intensity. (a) $\mu = 0.98$, and (b) $\mu = 1.02$. (c,d) Corresponding histograms of the IDIs. (e) Mean inter-dropout interval ($\langle \Delta T \rangle$) vs. pump current. (f) Normalized standard deviation ($\sigma / \langle \Delta T \rangle$) vs. pump current. (g) Detail of the regular pulse packages in the simulated time-series for $\mu = 0.98$. this figured is taken from the supplementary information of *A. Aragoneses et al., Sci. Rep.* **4**, *4696, 2014*. The simulations were performed by Sandro Perrone.

towards stable fixed points in phase space, and escapes from the fixed points are triggered by noise [34, 35]. *Chapter 4* of this *Thesis* is devoted to statistically distinguish dropouts triggered by stochastic fluctuations and dropouts which display signatures of determinism.

Chapter 3

Symbolic time-series analysis

One of the pleasures of looking at the world through mathematical eyes is that you can see certain patterns that would otherwise be hidden.

Steven H. Strogatz

3.1 Introduction

As already mentioned in *Chapter 1* and *Chapter 2*, a great variety of complex systems can be found in nature, whose different dynamics range from complete regularity to full stochasticity. Between these extremes, many levels of complex behavior can be manifested.

When studying a dynamical system, it can happen that, due to the intrinsic characteristics of the system, or due to the limitations of the experimental detection equipment, the information can only be recorded in the form of sequences of events, i.e., sequences of spikes, earthquakes, tweets, peaks of solar magnetic activity, etc.

When analyzing a time series obtained from an experiment or from a numerical simulation, from a natural or a man-made system, it is not straightforward to determine which method of analysis extracts all the information that is contained in the time series. Different analysis methods have been developed through the years, specially devoted to quantify the complexity of the dynamics [14, 89–93].

One relevant information when analyzing complex time series is whether they have been produced by a stochastic process, by a deterministic one, or by a combination of both. One way of distinguishing if the dynamics is deterministic or stochastic is by estimating the Lyapunov exponent, or the Kolmogorov-Sinai entropy [90, 94, 95]. These measures give information about how chaotic or stochastic a system is.

The correlation dimension also provides relevant information as a pure stochastic system has an infinite fractal dimension, while a deterministic system has a finite fractal dimension, as introduced by Grassberger and Procaccia [96].

Entropy is a relevant concept in dynamical systems, as it can be interpreted as the disorder, or lack of information in a system. Shannon [97] defined entropy as the measure of the uncertainty associated to the physical process, P, as

$$S[P] = -\sum_{i=1}^{N} p_i \ln(p_i), \tag{3.1}$$

where the probabilities $\{p_i\}$, such that $\sum_{i=1}^{N} p_i = 1$, characterize the process P. For a completely known process, which is predictable with certainty, Shannon's entropy is minimum, $S[P] = 0$, while for a uniform distribution, where the knowledge about the system is minimum and all outcomes are equally probable, Shannon's entropy is maximum, $S[P] = ln(N)$, with N being the number of possible outcomes.

Another way to quantify the stochasticity and determinism in time series is by considering coarse grained dynamical entropies, based on the fact that infinite precision is a never reachable limit [98], and considering a nontrivial dependence between precision and predictability.

The auto-correlation function is another well-known function, commonly used to infer correlations and nontrivial structures in the data [89]. It can be used to explore correlations at different time scales in the time trace, as it compares the trace with itself after a delay τ, and allows to find repeating patterns in the complex signal. The auto-correlation function is related to the power spectral density, through the fast Fourier transform (Wiener-Khinchin theorem), which is another well-kown time series analysis method in the frequency domain. It allows to idensity the characteristic frequencies in the dynamics.

3.2 Symbolic analysis

Another way of analyzing and extracting information from time series is by transforming the acquired data into series of symbols. This method can retain the relevant temporal information of the system, and can result in a faster and more efficient numerical computation [99]. Transforming a time series into a series of symbols is referred to as symbolic analysis. It consists in defining certain symbols or patterns, from the original time series, which will be then analyzed.

Most approaches for defining symbols rely on partitioning the range of the original observations into a finite number of cells or patterns. This discretization process can be based on the Poincaré section [100], that follows a stroboscopic sampling of the multidimensional trajectory of the system in phase-space, giving as result a discrete-time mapping, having reduced the dimensionality of the problem. Poincaré section can then be subdivided into cells and assign to all points in each cell the same symbol.

The transformation into a symbolic series can be based on a thresholding criteria, by transforming into a sequence of 'ones' and 'zeros' those values that are higher or lower, respectively, than a specific threshold [101, 102]. To inspect different time scales this binary symbolic sequence can also be transformed into a sequence of more than two symbols by collecting groups of consecutive symbols.

The temporal structure present in the system can be revealed by computing the relative frequencies of appeareance of each symbol in the sequence, and the presence of forbidden or missing patterns can also reveal relevant information about the dynamics of the system.

Of course, the conventional methods of time series analysis, such as auto-correlation, entropy or Lyapunov exponent calculations can be applied to the symbolic series to gain insight into the dynamics.

In 2002, Bandt and Pompe [103] proposed a new method for analizing time series, referred to as *ordinal analysis*. They define symbolic ordinal patterns by comparing neighbouring values of the time trace, and then compute the probability of each pattern.

3.3 Ordinal symbolic analysis

The method proposed by Bandt & Pompe is as follows:

Given a time series of length N, $X = \{x_1, x_2, x_3, ..., x_N\}$, it is divided in $N-D+1$ vectors of dimension D:

$$\{x_1, ..., x_D\},\ \{x_2, ..., x_{D+1}\},\ ...,\ \{x_{N-D}, ..., x_{N-1}\},\ \{x_{N-D+1}, ..., x_N\},$$

where D is the embedding dimension. Then each element of a vector is replaced by a number from 0 to D-1, according to the relative value of the element in the ordered vector (0 corresponding to the shortest, and D-1 to the longest value in each vector). In this way, each vector has associated an ordinal pattern (also referred to as *word*) composed of D symbols. The number of ordinal patterns for an ambedding dimension D is $D!$. For example:

• For $D = 2$ there are two possible ordinal patterns (OPs): $x_i < x_{i+1}$ gives word '01' and $x_{i+1} < x_i$ gives word '10'.

• For $D = 3$ there are six possible OPs: $x_i < x_{i+1} < x_{i+2}$ gives '012', $x_{i+2} < x_{i+1} < x_i$ gives '210', etc.

Figure 3.1 depicts schematically the ordinal patterns formed for $D = 2$, and $D = 3$. Also three of the 24 OPs for $D = 4$ are shown.

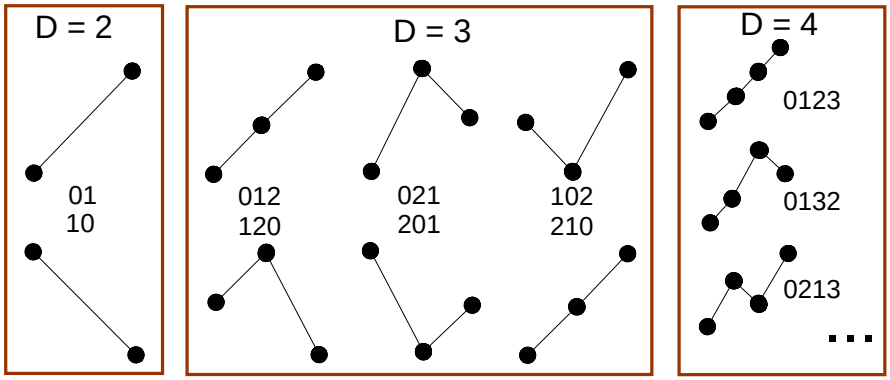

Figure 3.1: Schematic representations of the ordinal patterns (OPs) of dimension $D = 2$ ('01', and '10'), $D = 3$ ('012', '021', '102', '120', '201', and '210'), and three examples of OPs of dimension $D = 4$ ('0123', '0132', and '0213').

Then, by computing the probabilities of occurrence of the different words, the more frequent and the more unfrequent patterns can be found and one can gain also informatino about the existence of forbidden, or missing patterns [104, 105]. To perform a statistically significant analysis, the number of data points in the time series should be $N \gg D!$. Otherwise, it can not be distinguished whether the computed probabilities are due to the dynamics of the system of to lack of data.

Then, the *permutation entropy* is defined as the entropy of the probabilities of the $D!$ different patterns, normalized to its maximum value, $S_{max} = \ln D!$ [103]:

$$S = \frac{-\sum_{j=1}^{D!} p_j \ln p_j}{S_{max}},$$

Compared with other symbolic methods, the ordinal transformation has the advantage that the symbolic sequence keeps the information about the correlations present in the time-series and the memory in the system, but it has the drawback that the information about the actual value of each element is lost.

This analysis method can be used to explore the dependence of the probabilities of the ordinal patterns with different parameters of the system, whether from a model or from an experimental setup. As an example, the ordinal dynamics, with words of $D = 3$, of two well-kown dynamical systems is analized: the *logistic* and *tent maps*. Their iterative equations are given by

$$\text{Logistic map: } x_{n+1} = r x_n (1 - x_n)$$

$$\text{Tent map: } x_{n+1} = \begin{cases} \mu x_n \text{ if } x_n < 1/2 \\ \mu(1 - x_n) \text{ if } x_n > 1/2 \end{cases}$$

Given an initial condition, these two iterative models provide sequences of values which are deterministic time series, neglecting numerical noise. By comparing three consecutive values of the sequences, they can be transformed into sequences of $D = 3$ OPs. Then, the model parameter can be varied (r for the logistic map, and μ for the tent map), and the dependence of the probabilities with respect to the model

parameter can be analyzed. Figure 3.2 shows the probabilities of the OPs for the logistic map (a) and the tent map (b), as the corresponding model parameter is varied.

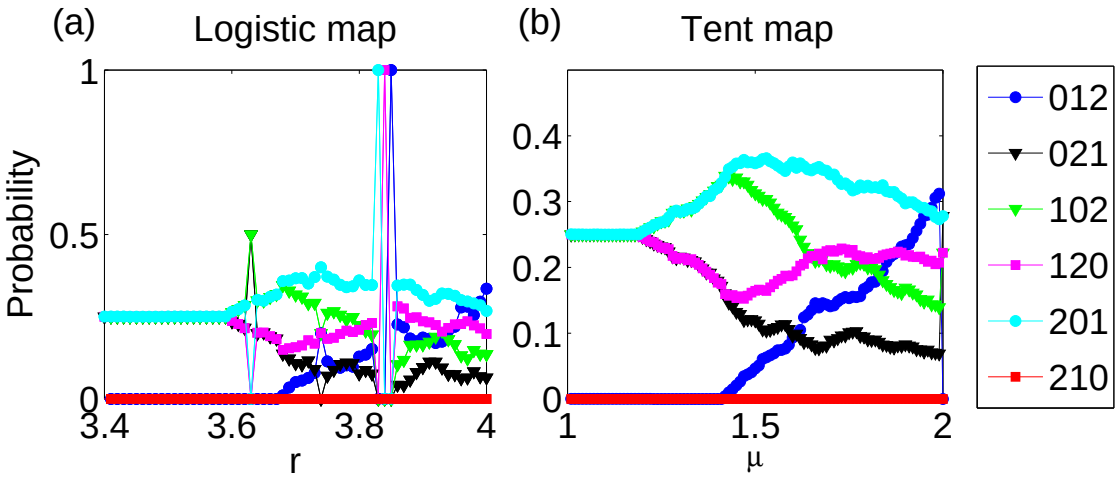

Figure 3.2: The probabilities of the ordinal patterns for $D = 3$ are plotted versus the model parameter for (a) the logistic map varying r, (b) the tent map varying μ.

In both maps, the ordinal pattern '210' is always a forbidden pattern. This indicates that three consecutively decreasing values can not be found in the time series. Also, for low parameter values, the ordinal pattern '012' is forbidden (three consecutively increasing values). Therefore, for low paramenter values, there is an oscillatory behavior such that only words which contain alternatively increasing and decreasing values are possible. As the model parameter values increase, changes in the dynamics are reflected in different probabilities of the words.

3.4 Applications of ordinal analysis

This ordinal pattern analysis has demonstrated its usefulness in several fields since it was proposed in 2002, from neuroscience, to stock markets, or climatology [106, 107].

Amigó and co-workers [104, 108] used it to distinguish deterministic chaos from stochasticity in time series with observational white noise. They analized the forbidden patterns, and their dependence with the time series length, studying the decay

rate of missing patterns. Carpi et al. [109] applied the ordinal patterns analysis to study Brownian motion and different types of noise. They studied the decay rate of the missing patterns with the time series length, and with the embedding dimension D. They found that missing ordinal patterns are more persistent in time series with higher correlation structures.

One issue of importance in a complex time series is determining the intrinsic time scale of the dynamics. Zunino et al. [110] applied the Bandt-Pompe methodology to a Mackey-Glass oscillator and found that the permutation entropy is minimum when the delay, r, used to construct the OPs $(x_1, x_{1+\tau}, x_{1+2\tau,\ldots})$ coincides with the delay of the system. This method has been shown to be robust to noise contamination or to considering systems with several time delays.

The probabilities of the different ordinal patterns can also be used to search for correlations among different time series. To do so, a two-dimensional array of ordinal patterns with $D! \times D!$ OPs can be constructed [111, 112].

Ordinal analysis has demonstrated to be useful also for the study of time series from neuroscience. For example, in epileptic seizures, it has been applied to identify and characterize the epileptic activity, in order to find evidence for the prediction of ocurrence of seizures. Veisi et al. [113] showed that ordinal patterns analysis allows distinguishing between normal and epileptic EEG. Cao et al. [114] found in some patients that, after a seizure, the brain first becomes more regular, then its irregularity increases and finally it moves to the normal state. Li et al. [115] used permutation entropy to detect the pre-seizure state in a group of rats in EEG, five seconds in advance. Another work [116] suggests that forbidden patterns may be used as a predictor of absence of epileptic seizures.

Ordinal analysis has also been applied in cognitive neuroscience, for example to achieve better signal-to-noise ratio in language processing experiments, with a significant reduction in the number of trials required to identify the task [117].

In cardiac diseases, ordinal analysis has also demonstrated its potential. These diseases are associated with changes in the patterns of beat-to-beat intervals. Permutation entropy has improved the diagnostic and classification under different conditions (congestive heart failure, myocardial infarction, or fetal heart state) [118–120]. Because of the interaction of the heart with other physiological mechanisms, failure

in one of them can lead to failure in the heart, or vice versa. This analysis method has shown to be useful in distinguishing the directionality of the driving [121].

The hability of ordinal analysis to discriminate between different types of time series has also found applicability in econophysics. Real time series from the stock market have been analyzed [122] and it has been found that they present a much higher number of forbidden patterns than stochastic time series. Ordinal analysis has also been used to identify periods where noise prevailed and periods with a more deterministic behavior of the makets. For example, Zunino et al. [123, 124] performed statistics of ordinal patterns to show that markets from developed countries have a lower number of forbidden patterns, and a higher permutation entropy, indicating that they are less predictable.

The ordinal patterns methodology has also been used to gain insight into the solar activity. In 2012, Suyal et al. [125] analyzed the solar wind of a specific solar cycle and found a hysteresis behavior with a fluctuating increase of the permutation entropy towards the peak activity, and a smooth decrease as the solar activity diminishes.

In climatology, the ordinal patterns time series analysis is also reporting its usefulness. By analyzing different intervals during the Holocene period, Saco et al.[126] found intervals of low permutation entropy, and an increase in the forbidden patterns, suggesting a higher predictability of the El Niño Southern Oscillation (ENSO), as well as periods of increasing and decreasing entropy of 2,000 years. Deza et al. [127] used the ordinal patterns with different embedding dimensions to explore climate networks, and found correlations between geographically distant regions at specific time scales. They found a clear relation between the spacing in the ordinal patterns and the connectivity in the equatorial Pacific area.

3.5 Ordinal analysis of the LFF regime

The LFF regime was described in detail in *Chapter 2*, and it is one of the aims of this *Thesis* to improve our understanding of this dynamics. With this purpose, ordinal analysis is used to analyze the time series of the output intensity of the laser in the LFF regime.

A thresholding method for detecting the dropout times is defined (see details in *Section 4.2*). Once the dropouts are detected, the intensity time series is transformed into a sequence of times when the dropouts occur, $\{t_1 < t_2 < t_3 < ... < t_N\}$. Then, ordinal analysis is applied to the sequences of inter-dropout intervals ($\Delta T_i = t_{i+1} - t_i$), also referred to as IDIs. This results in sequences of OPs, whose probabilities are then computed for the different experimental measurements, or model parameters.

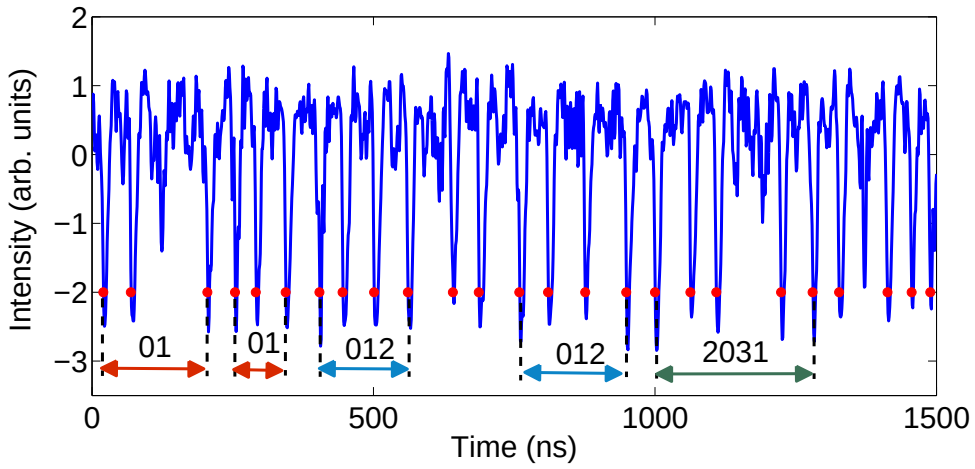

Figure 3.3: Typical experimental time series of a semiconductor laser with optical feedback in the LFF regime. The red dots indicate the detection of the dropouts, and several words are indicated as examples. Two words are depicted for $D = 2$; they correspond to two sets of two intervals each, which have different lengths, but they correspond to the same word ('01'). For $D = 3$ the word '012' is shown; for $D = 4$, the word '2031' is shown.

Figure 3.3 shows a typical time trace of the laser intensity in the LFF regime. As examples, some words for $D = 2$, $D = 3$, and $D = 4$ are depicted. The detection of the dropouts is indicated with red dots. It has to be noticed that, as the absolute magnitude of the time interval between dropouts is not taken into account, two different sets of intervals can give rise to the same word. This is shown in Fig. 3.3 with the two words of $D = 2$ ('01'), and the two words of $D = 3$ ('012') depicted.

When forming words, once the first one is constructed, there are two options for the consecutive ones: they can be considered by overlapping values, i.e., $\{\Delta T_1, \Delta T_2, \Delta T_3\}$, $\{\Delta T_2, \Delta T_3, \Delta T_4\}$, ...; or non-overlapping values, i.e., $\{\Delta T_1, \Delta T_2, \Delta T_3\}$,

$\{\Delta T_4, \Delta T_5, \Delta T_6\}$, ... In the experimental time traces, the probabilities computed in one way or in the other give equivalent results, something that is expected, as the acquisition of the experimental data performed by the oscilloscope could have began at t_1, at t_2, or at t_3, etc. In order to have longer statistics, each sequence of dropouts is transformed into D sequences of words, by considering respectively t_1, t_2, ..., t_N as the first dropout for each sequence. Then the probabilities obtained with each sequence of words are averaged. This is equivalent to consider overlapping OPs.

This transformation of the time series allows to compute the probabilities of the different words as the experimental or numerical parameters are varied, for example, the pump current in a laser with optical feedback, or the modulation amplitude, in the case of a laser with external periodic forcing.

The Bandt & Pompe method has already shown to succesfully characterize the dynamics of semiconductor lasers with feedback. In 2010, Tiana-Alsina et al. [128] used ordinal analysis to characterize the LFF dynamics. They computed the entropy and the statistical complexity measure introduced by Martín et al. [129] via ordinal patterns. They found a trasition in the dynamics, as the pump current is increased, characterized by a reduction of the permutation entropy accompained by an increase of the statistical complexity, which is robust to the size of the data sets and the dimension of the ordinal patterns. In a follow-up study, Rubido et al. [130] applied the ordinal analysis to characterize the dynamics of the LFF regime for a wide range of pump current values. They found that for low pump currents the dropouts have no correlations, as all the words were equally probable; but for higher pump currents, correlations between consecutive dropouts appear. Their results were consistent with the previous study [128], and demonstrated that ordinal pattern analysis is also a powerful tool for model validation.

Soriano et al. [131] and Zunino et al. [132] also estimated the permutation entropy, together with the permutation statistical complexity, of a semiconductor laser with feedback in the chaotic regime. By analyzing these quantifiers as a function of the embedding dimension, they identified the relaxation oscillation period and the feedback time delay.

Xiang et al. [133] used the permutation entropy to study the unpredictability of the chaotic dynamics of a laser diode with polarization-preserved and polarization-

rotated feedback. They performed model simulations [134] to study the dependence of the permutation entropy with the pump current, for the X-polarization, Y-polarization modes and the total output of the laser. They found that the effect of both types of feedback is different, i.e., while for polarization-preserved feedback the permutation entropy of the X-mode and the Y-mode are quantitatively different for low pump currents, they are equal for the polarization-rotated feedback.

More recently, Toomey and Kane [135] estimated the permutation entropy of a laser diode with optical feedback for different feedback strengths and pump currents, showing the different degrees of complexity in a two-dimensional parameter space (optical feedback and pump current). They showed that the degree of complexity is sensitive to the delay used to compute the ordinal patterns.

The following *Chapters 4*, *5* and *6* of this *Thesis* present the results of analyzing experimental LFF time series using the Bandt & Pompe ordinal analysis method, and novel results about serial correlations among dropouts, and about the underlying structure of the LFF dynamics are presented.

Part II: Results

Credo che nella discussione di problemi naturali dobbiamo cominciare non con le Scritture, ma con gli esperimenti e dimostrazioni.
Galileo Galilei

Chapter 4

Distinguishing signatures of determinism and stochasticity in the LFF dynamics

...when you have eliminated all which is impossible, then whatever remains, however improbable, must be the truth.
Sherlock Homes (The Blanched Soldier)

4.1 Introduction

Deterministic nonlinearities and noise are present in many natural systems (neuronal networks, Brownian motion, climate, economics) and the distinction of the relative influence of each contribution is a long-standing challenge [10–16, 136–138]. This can be particularly difficult in complex systems and in systems with time delayed interactions, since high-dimensional chaos can be in practice indistinguishable from stochastic dynamics.

As described in the *Introduction*, a semiconductor laser with optical feedback is a well-known example of this situation: the interplay of deterministic nonlinear light-matter interactions, spontaneous emission noise and time-delayed feedback, results in a complex dynamical behavior [8]. In particular, as described in *Chapter 2*, this

nontrivial interplay is responsible for the LFF dynamics, which occurs close to the lasing threshold, and for moderate feedback strengths.

In this chapter, the symbolic ordinal analysis introduced by Bandt and Pompe [103], and explaind in *Chapter 3*, is used to study the LFF dynamics, with the goal of distinguishing signatures of determinism and stochasticity in the time series of inter-dropout intervals. It is shown how this analysis allows to statistically determine which of the dropout events are compatible with a stochastic process and which have a more deterministic nature. This distinction is relevant in many different dynamical systems, as noise is present in most of them, and high dimensional chaos is very dificult to distinguish from noise.

By experimentally varying the laser drive current, it is covered the range of pump currents where the laser displays spiking dropouts: from low pump currents, where the intensity is low and the dropouts are too small to be distinguished from small fluctuations, to high pump currents, where the dropouts become very frequent and they can not be distinguished from one to another as individual events.

The inter-dropout interval (IDI or ΔT) sequence is transformed into a symbolic sequence of ordinal patterns (OPs), or words. Then, a threshold is chosen, ΔT_{th}, to classify IDIs into two types: those shorter than ΔT_{th} are referred to as *short intervals* (SIs) and those longer than ΔT_{th}, as *long intervals* (LIs). In this way the laser spiking activity is separated in periods of fast dropout events that alternate with periods of no events. The motivation for this classification is that some dropouts can be noise-induced while others can be due to a deterministic underlying dynamics [32, 34, 35]. Thus, some IDIs correspond to waiting intervals in a resting state until noise triggers a dropout, while others correspond to time intervals between dropouts that are more likely to have a deterministic origin.

The probabilities of the words formed by consecutive SIs and by consecutive LIs are computed, and it is found that there is a range of pump currents where they are significantly different; the LI probabilities are consistent with stochastic dropouts while the SI probabilities have a more deterministic distribution. Since the type of dynamics analyzed here occurs in various natural complex systems under the influence of noise, the method proposed here can be a powerful tool of time-series analysis of spiking systems, at an event-level description of the dynamics.

The results presented in this chapter have been sumarized in [139].

4.2 Experimental setup

The experiments are performed with a 675 nm AlGaInP semiconductor laser (Hitachi Laser Diode HL6724MG) with optical feedback from a diffraction grating (see Fig. 7.1). The external cavity length is 45 cm and, thus, the feedback delay time is 3 ns. To detect the laser output power a beam-splitter is used, that sends 50% of the light to a 2 GHz photodetector, and then to a 2.5 GHz oscilloscope (Agilent Infiniium 9000). The laser temperature and pump current are controlled to an accuracy of 0.01 C and 0.01 mA respectively (with a ITC502 Thorlabs laser diode controller). The measurements are obtained at T=18C. At this temperature, the threshold current of the solitary laser is 27.6 mA, which is reduced to 25.7 mA under optical feedback (the feedback strength being such that the threshold reduction is 7%). In the experiments the pump current is varied in steps of 0.20 mA, from 26.20 mA to 28.00 mA.

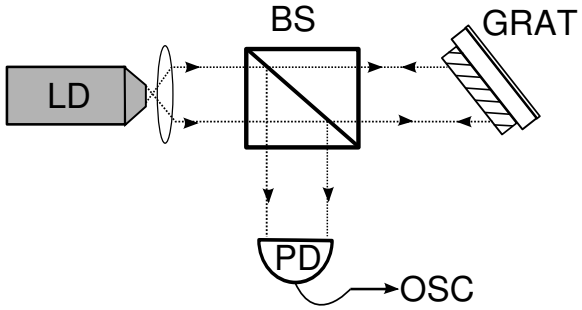

Figure 4.1: Experimental setup of a semiconductor laser with external optical feedback from a difraction grating. LD stands for laser, BS for beamsplitter, GRAT for grating, PD for photodetector ans OSC for oscilloscope.

In order to perform a robust statistical analysis, one time series of 32 million points for each pump current is recorded, with a sampling time of 0.5 ns. As the frequency of dropouts rises with the pump current, less statistics are available for low pump currents than for high pump currents. However, the time series recorded (45,000 dropouts for low pump currents, and more than 220,000 for high pump currents) provide a much longer statistics than previously reported [8, 30, 130].

4.3 Detection of the dropout times

The laser intensity detected is filtered out by the photodetector's and the oscilloscope's bandwidth (2 GHz and 2.5 GHz, respectively). This enables to study the LFF dynamics but not the underlying fast picosecond dynamics [24]. The shape and depth of the dropouts is not the same for all pump currents. For low pumps the dropouts are less frequent, their depth distribution is wide (some dropouts are deeper while other dropouts are shallower) and the time trace is quite noisy, which makes the dropout detection not straightforward. Figure 4.2 (a) shows as example, the time series of the laser for a low value of the pump current ($I = 26.4$ mA). For increasing pump current the dropouts become more frequent and more similar in depth. Figure 4.2(b) shows the time trace for a higher value of the pump current ($I = 27.2$ mA).

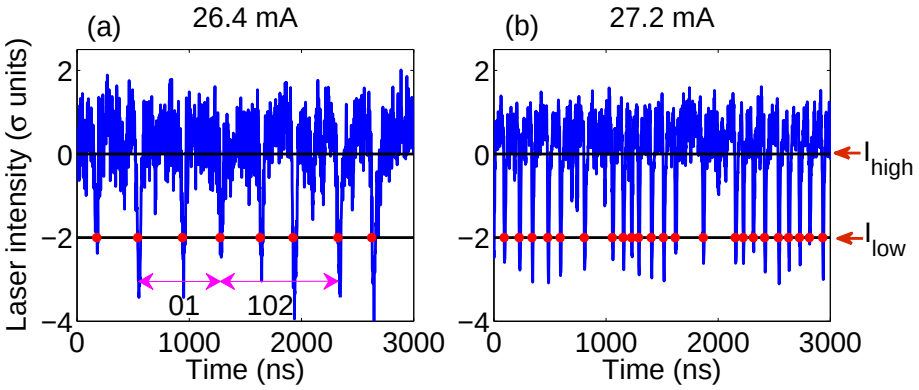

Figure 4.2: Time series of the intensity of the laser for (a) 26.4 mA and (b) 27.2 mA. The red dots indicate the dropout detection and the solid black lines the low and high detection thresholds.

The method used to detect when a dropout takes place is the following: first, each time series is normalized to have zero mean value and standard deviation equal to one. Next, the dropout times were determined by using a double thresholding method: when the intensity decreases below a certain value (I_{low} in Fig. 4.2), a spike is recorded. Then, it is required that the intensity grows above a high threshold, which is set to zero (I_{high} in Fig. 4.2), before another dropout can occur. This avoids detecting spurious dropouts, specially during the intensity recovery (the drop

is sharp but the recovery is gradual and noisy). Alternatively, one could use a refractory time after each dropout, during which the intensity is recovering and no dropouts are detected. In Fig. 4.2 the detections are indicated with red dots, and the two thresholds with solid black lines. For consistency, the detection thresholds all the time series are set at the same values (see {Section 5.3 for a discussion of the effect of the threshold).

4.4 Results

4.4.1 Ordinal analysis of the IDIs

In this section, the symbolic method introduced by Bandt and Pompe [103], and explained in *Chapter 3*, is applied to the sequences of IDIs recorded in the experiments. For each pump current, the IDI sequence, $\{\Delta T_i\}$, is transformed into a sequence of words of length D, by considering the relative length of D consecutive IDIs. Figure 4.2(a) shows, as examples, one word of dimension $D = 2$ ('01', $\Delta T_i < \Delta T_{i+1}$) and one word of dimension $D = 3$ ('102', $\Delta T_{i+1} < \Delta T_i < \Delta T_{i+2}$). As explained in *Chapter 3*, this symbolic transformation neglects the information contained in the duration of the IDIs, but keeps the information about the correlations in the dropout sequence and the short-time memory in the system.

By counting the number of times a word appears in the symbolic sequence, the probabilities of the various words are computed (p_i with $i = 1 \dots D!$). The results are displayed in Fig. 4.3, that shows the probabilities, for each pump current, of the two words for the case of $D = 2$ (Fig. 4.3(a)), the six words for the case of $D = 3$ (Fig. 4.3(b)), and the twenty-four words for the case $D = 4$. The error bars represent the confidence interval computed with a binomial test, corresponding to a confidence level of 95%, and the gray region represents the probability values consistent with the null hypothesis (N.H.) that there are no correlations in the sequence of dropouts and thus, the words are equally probable. Probability values in the gray region, $p \pm 3\sigma_p$, are consistent with the N.H., where $p = 1/D!$ and $\sigma_p = \sqrt{(p(1-p)/N)}$, with N being the number of OPs in the sequence.

It can be observed in figures 4.3(a), 4.3(b) and 4.3(c) that, except at low pump currents, the most probable words are '10' for $D = 2$, '210' for $D = 3$, and '3210' for

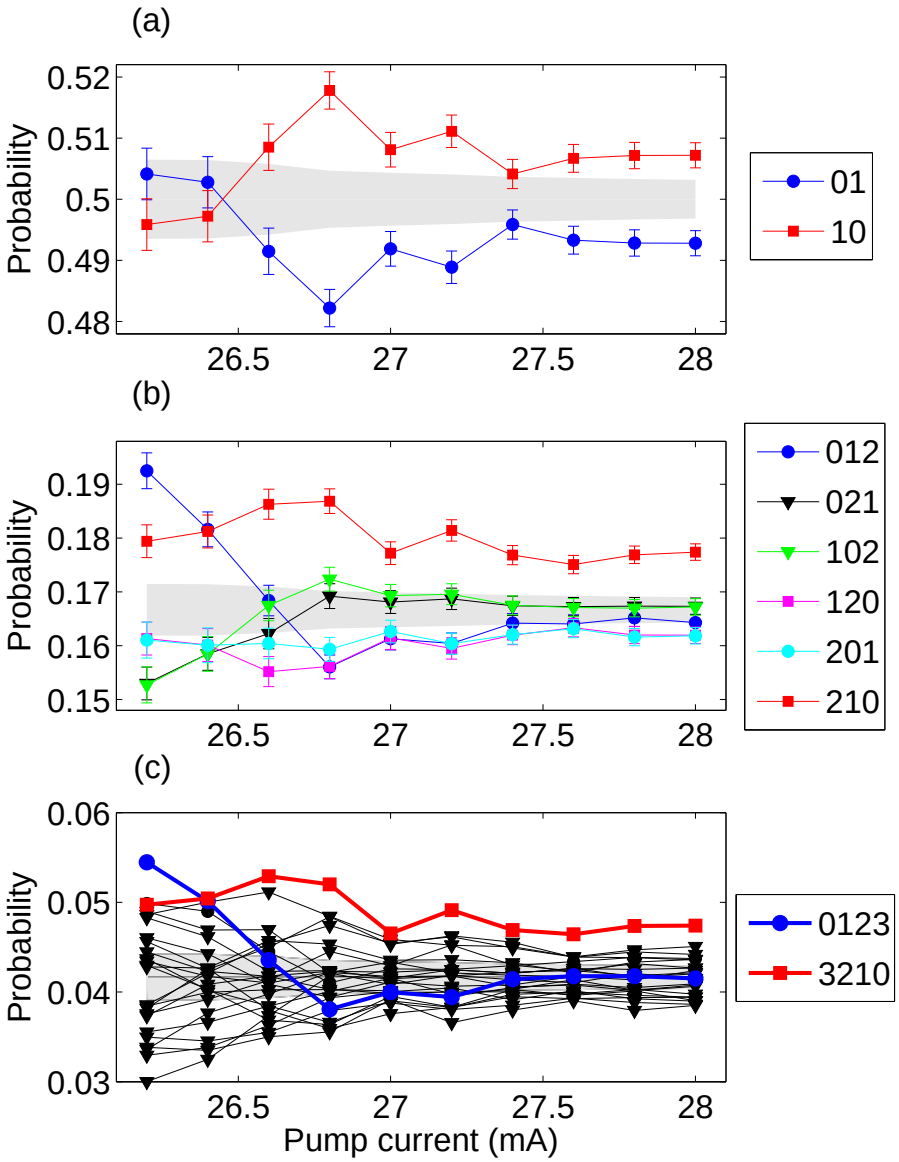

Figure 4.3: Probabilities of words formed with (a) $D = 2$, with (b) $D = 3$ consecutive IDIs, and with (c) $D = 4$ consecutive IDIs. The gray region indicates probabilities consistent with the null hypothesis that there are no correlations in the IDI sequence. Except for the lowest values of the pump current, the most probable word is the one formed by consecutive decreasing IDIs. In (c), the words formed by four consecutively increasing ('0123') and four consecutive decreasing ('3210') IDIs are highlighted in blue and red, respectively.

$D = 4$, respectively. These words correspond to two, three and four consecutively decreasing IDIs respectively. For $D = 4$ (Fig. 4.3(c)) the word '3210' is highlighted in red. Notice that, at low pump currents, the analysis for $D = 2$ (Fig. 4.3(a)) gives probabilities that are consistent with a stochastic behavior (they are within the N.H. region); however, the analysis for $D = 3$ Fig. 4.3(b)) actually reveals a significant degree of determinism, since there are several words with probabilities outside the N.H. gray region for all pump currents. Also signals of determinism are present for $D = 4$. This shows correlations for this low pump current values, that can not be detected with $D = 2$.

4.4.2 Classifying the IDIs as long and short intervals

To further analyze the underlying structure of the experimental sequence of dropouts a threshold is selected, ΔT_{th}, close to the most probable IDI value, ΔT^*. *Section 4.4.3* discusses the criterium used for selecting the threshold and classify the IDIs into two types: those shorter than ΔT_{th}, as SIs (short intervals), and those longer than ΔT_{th}, as LIs (long intervals). Figure 4.4 shows the histograms of ΔT for two pump currents and the threshold to classify into SIs and LIs is depicted as a red line ($\Delta T_{th} = 0.9\Delta T^*$). As examples, Fig. 4.4(a) shows two IDIs classified as SI and LI. By counting the number of times a word appears in the sequence of consecutive LIs or consecutive SIs, new probabilities of words are now computed, formed by consecutive LIs (referred to as LI words) and by consecutive SIs (SI words).

Because the words are now formed with consecutive LIs or SIs, there are shorter sequences of words, as compared to those in the full sequence of IDIs; however, the data sets are long enough to still allow calculating the LIs and SIs probabilities with good statistics.

One of the criteria used for choosing the threshold is to obtain enough LI and SI words to allow for a robust statistical analysis. For example, for $\Delta T_{th} = 0.9\Delta T^*$ and $D = 2$, the number of words of SI is about 6,000-7,000 for low and high current respectively, and the number of words of LI is about 9,000-68,000. For $D = 3$ the number of words is smaller, formed by about 1,900-1,300 SI words, and about 3,800-35,000 LI words. The probabilities of the LI words and of the SI words are displayed in Fig. 4.5 for $D = 2$ and $D = 3$ words. In both cases, the LI probabilities are

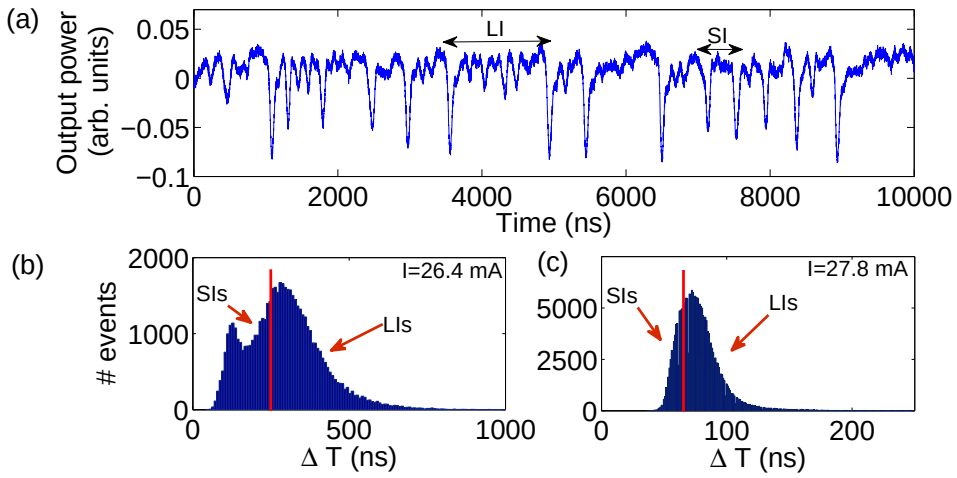

Figure 4.4: (a) Experimental time series of the laser intensity displaying several dropouts. The pump current is 26.4 mA. Also as examples, two IDIs are classified either as SIs or as LIs (see *Section 4.4* for details). (b,c) Histogramd of the IDIs for a pump current of 26.4 mA and 27.8 mA, respectively. The red lines indicate a threshold corresponding to $\Delta T_{th} = 0.90\Delta T^*$ to classify the IDIs into SIs and LIs. By doing this, the distribution corresponding to the LIs is close to a decaying exponential, compatible with a stochastic process.

displayed in the left column, and SIs in the right column.

In these figures it is observed that the OPs formed by consecutive LIs appear equally probable for all pump currents, as it is expected in a random process like noise-induced escapes. On the other hand, the probabilities of the OPs formed by consecutive SIs keep the deterministic signature of the IDI sequence, except at low pump currents, while the random signatures of the LIs have been removed.

It should be noticed that at low pump currents, both LIs and SIs are consistent with the null hypothesis, for $D = 2$ and for $D = 3$ (Fig. 4.5). By fine-tuning it could not be found a threshold that allowed to separate the IDIs into two sets with significantly different statistical properties. While for $D = 2$ this could be expected (as also for $D = 2$ the IDIs seem stochastic, and lie in the gray region), for $D = 3$ this is rather unexpected as the probabilities of the words formed by consecutive IDIs are all not consistent with the N.H., as can be seen in Fig. 4.3(b).

Moreover, the IDI distribution, shown in Fig. **??**(b), has a nontrivial structure at low IDI values and an exponential decay at large IDIs, suggesting the existence of two IDI categories. The fact that when separating the IDIs in LIs and SIs we obtain two sets consistent with the N.H. means that, by separating, the correlations existing in the IDI sequence are removed. This effect can be understood in terms of the numerical results in Refs. [34, 35], where it was shown that the average duration of the transient dynamics decreases with increasing current values. Thus, at low pump currents long intervals between consecutive dropouts might occur during the transient dynamics, and these "long SIs" have time-scales comparable to noise induced escapes. Therefore, in the low pump current region the method can not distinguish two different IDI categories, in spite of the fact that the distribution of IDIs displays a bimodal structure.

To further demonstrate that the LIs and SIs have indeed different statistical properties (and thus are likely to correspond to dropouts triggered by different mechanisms), the histograms of the time intervals composed by the sum of consecutive SIs, $\sum \Delta T_{i,SI}$, and by the sum of consecutive LIs, $\sum \Delta T_{i,LI}$, are computed. These are shown in figure 4.6. The histogram of the sum of consecutive LIs displays an exponential decay, as can be expected for a variable that is the sum of independent random variables, each with an exponentially decaying distribution. On the contrary,

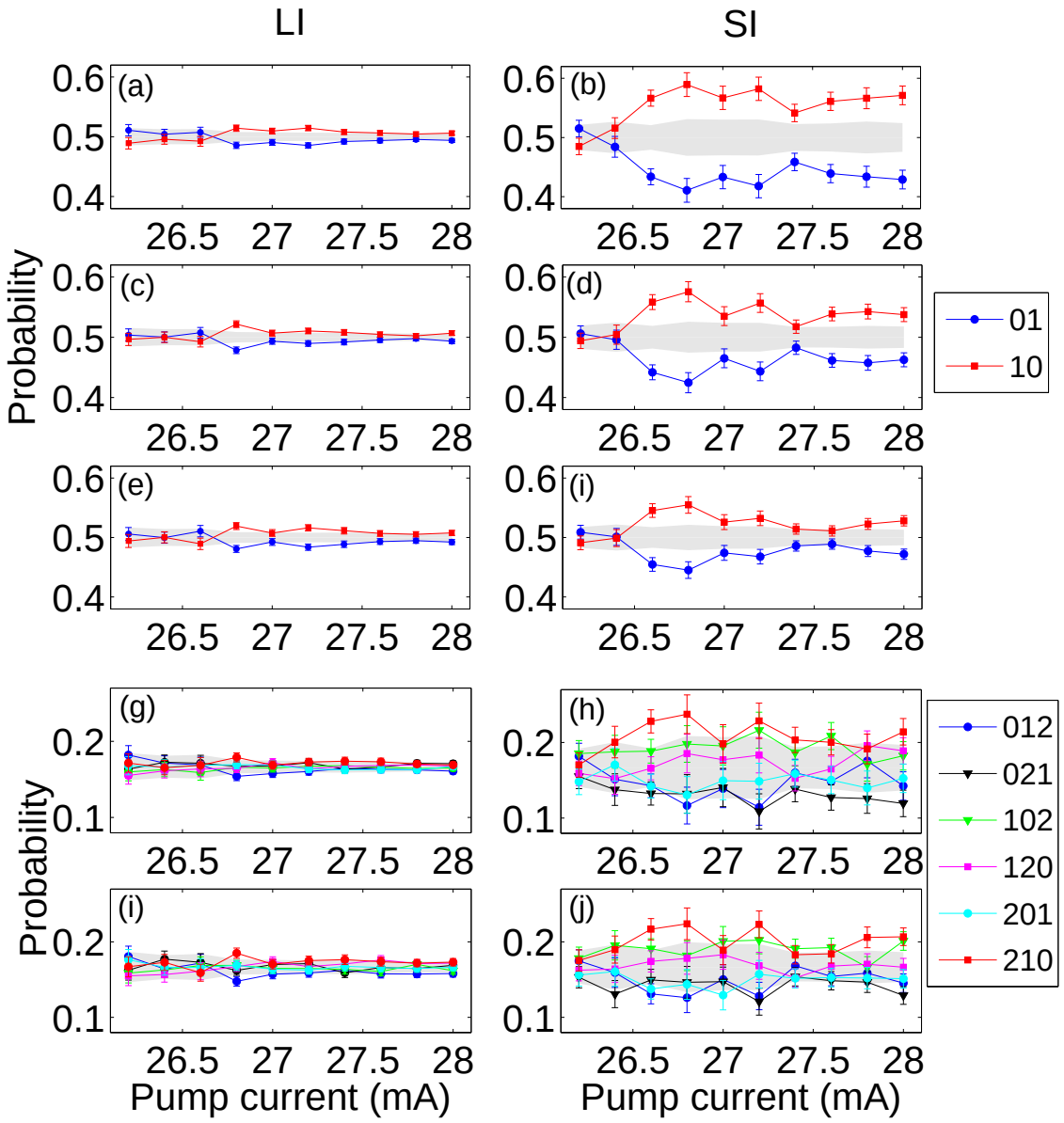

Figure 4.5: (a,c,e) Probabilities of $D = 2$ words formed by consecutive LIs. (b,d,f). Probabilities of $D = 2$ words formed by consecutive SIs. The probabilities are computed for three threshold values, (a,b) $0.85\Delta T^*$; (c,d) $0.90\Delta T^*$; and (e,f) $0.95\Delta T^*$. ΔT^* is the most probable IDI value. Figures 4.4(a) and 4.4(b) depict, with a vertical red line, the threshold corresponding to $0.95\Delta T^*$. (g,i) Probabilities of $D = 3$ words formed by consecutive LIs. (h,j) Probabilities of $D = 3$ words formed by consecutive SIs. The probabilities are calculated using the threshold $0.90\Delta T^*$ (g,h) and $0.95\Delta T^*$ (i,j).

the histogram of the sum of consecutive SIs displays a nontrivial structure.

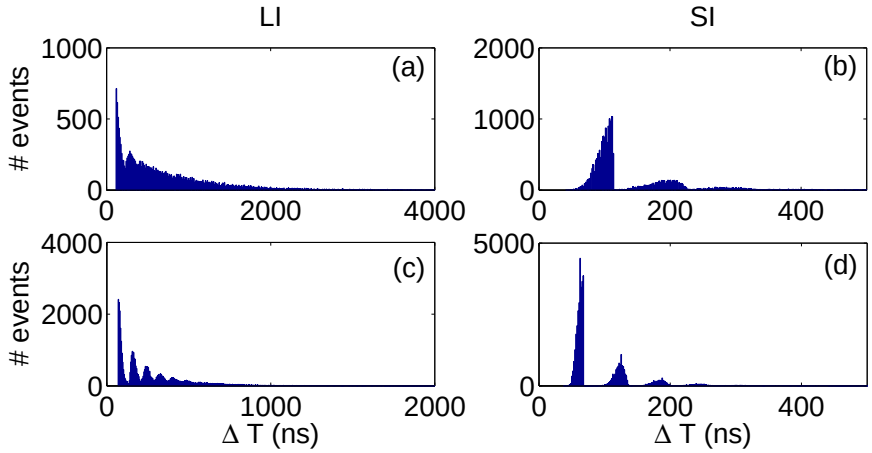

Figure 4.6: Histogram of the sum of consecutive LIs, $\sum T_{i,LI}$ (a,c), and of the sum of consecutive SIs, $\sum \Delta T_{i,SI}$, (b,d). The laser pump current is 26.8 mA (a,b) and 27.8 mA (c,d). Threshold is $0.95\Delta T^*$.

In the interpretation of the SIs as time-intervals between deterministic dropouts, the sum of consecutive SIs represents the duration of the transient dynamics, before returning to the resting state. Thus, this distribution of transient times can be traced back to a deterministic attractor that rules the dynamics, and can be compared with recent simulations by Zamora-Munt et al. [35]. The good agreement with the simulated statistics of transient times enforces the interpretation of the dropouts observed experimentally as a dynamics sustained by intrinsic laser noise.

4.4.3 Influence of the classification threshold

As the choice of the threshold is rather arbitrary, it can be expected that there will be short LIs that are wrongly classified as SIs, and long SIs that are wrongly classified as LIs. However, Fig. 4.5 shows that the differences between the LI and SI probabilities are significant (except at low pump currents) and that they are robust to threshold variations. It can be observed that the lower threshold reveals more deterministic SIs (with probabilities far from the uniform distribution) but has the drawback of a larger degree of uncertainty (i.e., the error bars and the N.H. region are wider due to a low number of OPs in the SI sequence). On the other hand, for

the larger threshold one can observe that the degree of SI determinism decreases, while the robustness of the analysis increases (i.e., the error bars and the width of the N.H. region of the SI probabilities decrease due to a larger number of OPs in the sequence). As the variation of the threshold leaves rather unaffected the number of LI OPs, it has almost no effect on the LI probabilities.

In Fig. 4.5 the thresholds were selected in order to take into account the following three goals: i) enough SI and LI words can be formed to compute their probabilities with good statistics (i.e., having small error bars and narrow N.H. region), ii) the LI OP distribution is close to the uniform distribution, and iii) the distribution of the LIs is close to a decaying exponential. In the histograms in Fig. 4.4, it can be observed that the distributions corresponding to the LIs are close to decaying exponentials.

While in this analysis, the same threshold has been chosen for all data sets ($T_{th} = \alpha \Delta T^*$, where α in the range 0.85-0.95 takes the same value for all pump currents), the method could be optimized by fine-tuning the threshold such that it is optimal for each data set, giving a sequence of LIs with the closest statistics to a random sequence of events.

4.4.4 Permutation entropy

The different statistical properties of the IDIs, LIs and SIs are also captured by the permutation entropy [103], i.e., the entropy of the probabilities of the OPs, $S = -\sum_{j=1}^{N} p_j \ln p_j$, normalized to its maximum value, $S_{max} = \ln D!$ (see {Chapter 3). This has been shown to be an appropriate measure of complexity for chaotic time series in the presence of noise [14, 106, 135].

Figure 4.7 displays the permutation entropy computed for OPs formed by consecutive IDIs (top), LIs (middle) and SIs (bottom), for a threshold $\Delta T_{th} = 0.95 \Delta T^*$. Notice that the entropy of SI-words is smaller than that of IDIs and LIs, which is consistent with a lower degree of randomness in the SI sequence, as compared to the IDI and LI sequences.

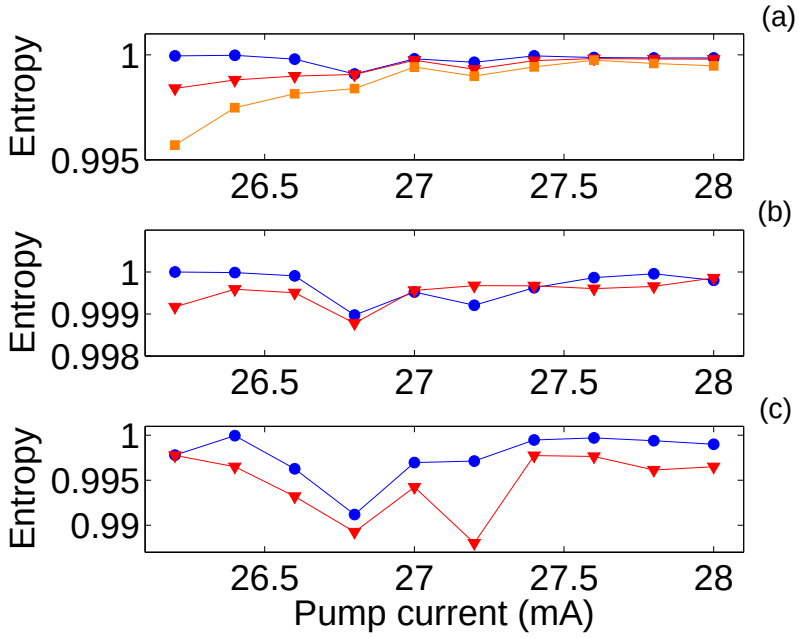

Figure 4.7: Permutation entropy of OPs formed by consecutive IDIs (a), LIs (b) and SIs (c). Circles correspond to OPs of length $D = 2$, triangles $D = 3$, and squares to $D = 4$. Threshold for classifying the IDIs as LIs or SIs is $0.95\Delta T^*$.

4.4.5 Additional experimental measurements

In order to verify the robustness of the results, another set of measurements is presented, acquired at a temperature of 20C. The analysis of the IDIs does not reveal any significant difference with those acquired at 18C, neither in the OPs formed by the IDI sequence and their dependence with the pump current, nor in the OPs formed by consecutive LIs and SIs.

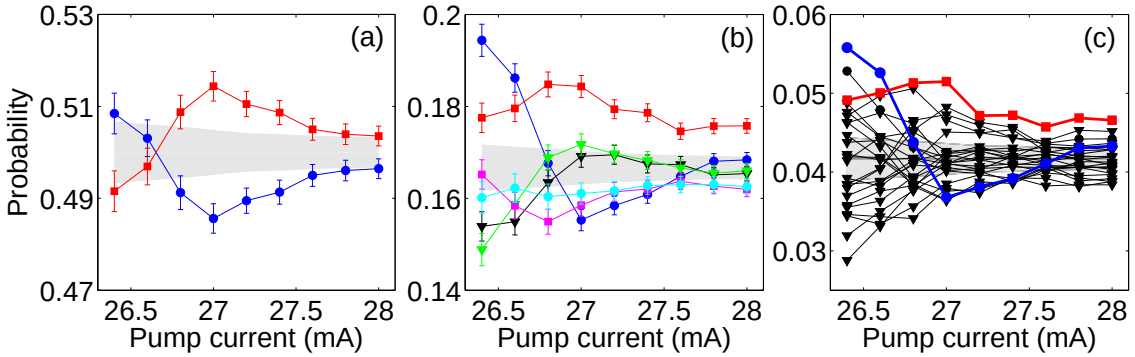

Figure 4.8: Probabilities of words formed with (a) $D = 2$ and with (b) $D = 3$ consecutive IDIs. Experimental data acquired at 20C.

Figure 4.8 shows the OPs for $D = 2$, $D = 3$ and $D = 4$ formed with the IDIs, for the 20C experimental data set. Figure 4.9 shows the OPs for $D = 2$ and $D = 3$ formed with consecutive LIs (left column and SIs (right column) for the different thresholds already used in the 18C experimental set.

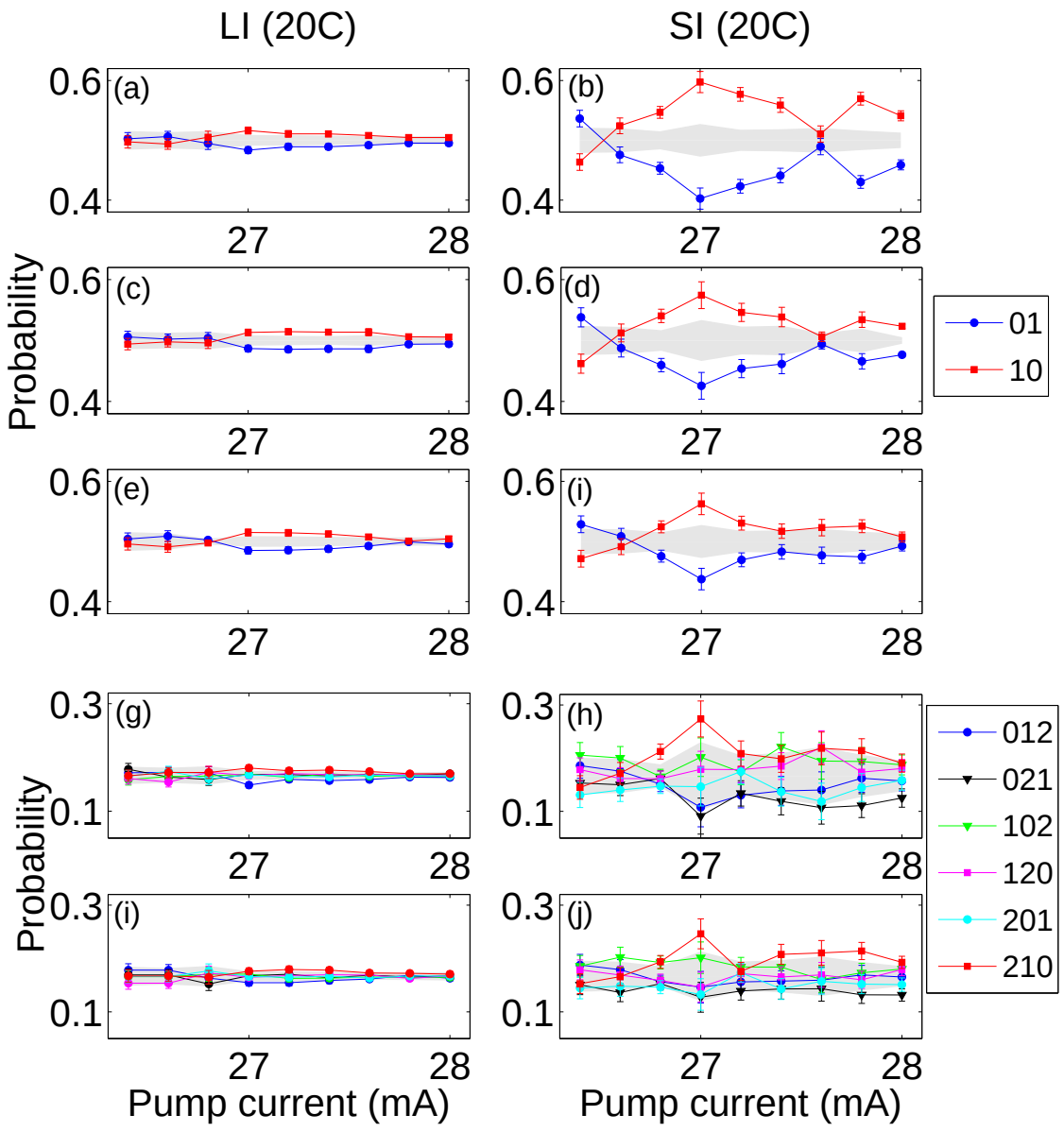

Figure 4.9: (a,c,e) Probabilities of $D = 2$ words formed by consecutive LIs. (b,d,f) Probabilities of $D = 2$ words formed by consecutive SIs. The probabilities are computed for three threshold values, (a,b) $0.85\Delta T^*$; (c,d) $0.90\Delta T^*$; and (e,f) $0.95\Delta T^*$. (g,i) Probabilities of $D = 3$ words formed by consecutive LIs. (h,j) Probabilities of $D = 3$ words formed by consecutive SIs. The probabilities are calculated using the threshold $0.90\Delta T^*$ (g,h) and $0.95\Delta T^*$ (i,j). Experimental data acquired at 20C.

4.5 Summary

In this chapter, a novel method of analysis has been proposed, that allows to distinguish statistical signatures of determinism and stochasticity in the sequence of dropouts of a semiconductor laser with optical feedback. The analysis reveals the existence of an underlying structure in the IDI sequence. By choosing an appropriate threshold, the IDIs can be classified into two categories, SIs and LIs, with significantly different deterministic components that suggest that different physical mechanisms trigger the dropouts. These are consistent with interpreting the LIs as waiting intervals in a resting state, and the SIs as intervals between dropouts occurring during the return to the resting state. Thus, the method allows statistically inferring which dropouts could be noise induced, and which ones could have a deterministic origin, due to a stochastic trajectory that follows an underlying attractor in its return to the resting state.

The threshold for classifying the IDIs as LIs or SIs is chosen taking into account three criteria: i) the probability distribution of the LIs is exponentially decaying (expected for noise-induced escapes), ii) the probabilities of the words formed by the LIs are close to the uniform distribution (also expected for noise-induced escapes), and iii) there are enough words formed by consecutive LIs and by consecutive SIs to perform a robust statistical analysis. There is a range of threshold values that meet these criteria and it is shown that the results are qualitatively robust to threshold variations within this range.

The method is computationally simple to implement and the data requirements can be easily adapted to small and large data sets by appropriately choosing the length D of the ordinal patterns. For improved performance, instead of using a general criterion across all data sets for selecting the threshold, ΔT_{th} could be fine tuned to work optimally for each data set, giving the sequence of LIs with an statistics closest to a random sequence of events.

The method proposed here can be a very powerful tool for the analysis of real-world data, such as experimental recordings of neuronal inter-spike intervals, or data generated by complex systems such as inter-event times of user activity in social communities, where signatures of deterministic underlying dynamics can be obscured by the presence of noise.

Chapter 5

Symbolic dynamics of a semiconductor laser in the LFF regime

Nothing is too wonderful to be true if it be consistent with the laws of nature.
Michael Faraday

5.1 Introduction

In the previous chapter, the capability of symbolic ordinal analysis to infer signatures of determinism and stochasticity in the LFF dynamics was shown. It was demonstrated that this analysis method can indicate which of the dropouts are statistically compatible with a stochastic process, and which reveal fingerprints of an underlying attractor.

In this chapter, ordinal analysis is used to unveil the hierarchical structure of the probabilities of the ordinal patterns in the LFF dynamics. Correlations among several consecutive dropouts are uncovered, not reported so far: it is shown that the probabilities of the patterns display a well-defined, hierarchical and clustered structure. The robustness of these findings are confirmed with different experimental measurements.

To test whether simulations of the stochastic Lang and Kobayashi model (LK model) also displays similar dropout correlations, the same symbolic analysis is applied to numerical time series, and it is confirmed the validity of the LK model also a this level of analysis. Most importantly, a minimal model, a modified circle map, which exhibits the same hierarchical and clustered symbolic organization, is identified. Since the circle map describes many dynamical systems, including neurons [48] and cardiac cells [140], the results presented in this chapter suggest that similar correlations and hierarchies of patterns can be found in other systems.

The experiments and the simulations with the circle map presented in this chapter were performed by the author, and the simulations of the Lang and Kobayashi model were performed by Sandro Perrone.

The results presented in this chapter have been sumarized in [141].

5.2 Experimental setup

The experimental setup is the same as in *Chapter 4* (see Fig. 7.1), i.e., a semiconductor laser in the optical domain (675 nm wavelength), with light propagating in free space, is submitted to optical feedback from a diffraction grating. The laser diode used in these experiments is an AlGaInP semiconductor laser (Sanyo DL-2038-023). The external cavity length is 70 cm, giving a feedback delay time of 4.7 ns. A beam-splitter sends 50% of the light to a 1 GHz oscilloscope (Agilent Infiniium DSO9104A). The laser temperature and pump current are controlled to an accuracy of 0.01 C and 0.01 mA respectively with a ITC502 Thorlabs laser diode combinator controller. The operating temperature is 18C and the laser pump current is varied in steps of 0.1 mA, from 26.3 mA to 27.3 mA. At 18C the threshold current of the solitary laser is $I_{th} = 27.8$ mA, and the feedback-induced threshold reduction is 6.5%. Time series of 32 ms are recorded (3.2×10^7 data points), containing 70,000 to 300,000 dropout events, for low and high pump current respectively.

5.3 Results

5.3.1 Experimental results

This section describes the experimental results, which on one hand they confirm the experimental results presented in the previous chapter, but on the other hand, novel findings about clusters in the word probabilities are presented.

For the time series analysis of the experiments, ordinal patterns for $D = 3$ consecutive intervals (four consecutive dropouts) are constructed. Figure 5.1 displays the probabilities of the six possible words computed from the time-series recorded. The symbolic analysis reveals that serial correlations among four consecutive dropouts are present in the dropout sequence: in Fig. 5.1 one can observe that the probabilities lie outside the gray region, and therefore, they are clearly not consistent with the null hypothesis.

Moreover, in this figure one can recognize a hierarchy in the probability values, which presents a crossover at about 26.6 mA: for higher pump currents the most probable word is '210' (corresponding to three consecutively decreasing interdropout intervals), while for lower pump currents, the most probable word is '012' (corresponding to three consecutively increasing intervals).

Figure 5.1 also reveals a clustered organization of the probabilities: words '021' and '102', on the one hand, and words '120' and '201', on the other hand, occur with similar probability. The probabilities of these two pairs of words present the same evolution when the pump current is varied. The same crossover at 26.6 mA is also found for these clusters. It is important to recall that this behavior can also be seen in the experiments presented in *Chapter 4* (Figs. 4.3(b) and 4.8(b)), where a different laser (Hitachi Laser Diode HL6724MG) was used, lasing at 675 nm and working at 18C, with a shorter external cavity (45 cm corresponding to 3 ns of time delay), and a threshold reduction of 7% (see Fig. 5.3 (b,c)).

Figure 5.2 displays the results for words of length $D = 2$ (a), and $D = 4$ (c). One can clearly observe that, also in these cases, the distribution of probability values is not consistent with the N.H., as several probabilities are outside the N.H. region. The same crossover is observed at about 26.6 mA for both embedding dimensions (2 and 4), just as it occurs for $D = 3$ (depicted in 5.2(b) for comparison). The words

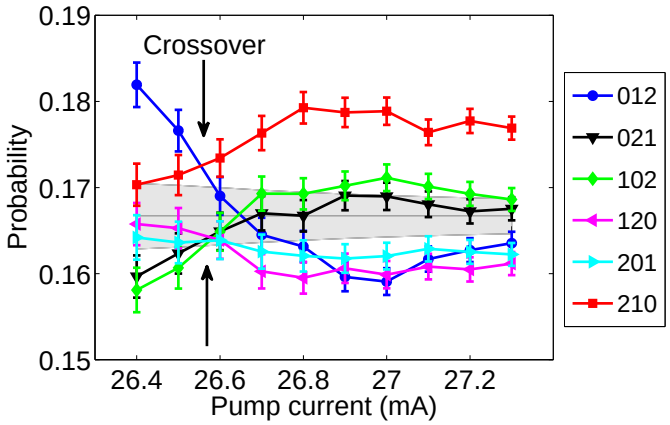

Figure 5.1: Probabilities of the six words vs. the laser pump current. A crossover in the hierarchical organization of the words occurs at about 26.6 mA: at lower current values the word '012' (blue) is the most probable one, while at higher currents values, the word '210' (red) is the most probable one. Two clusters of words can be observed, with similar probabilities: '021'-'102' (black-green) and '120'-'201' (magenta-cyan).

formed by consecutively increasing and consecutively decreasing intervals ('0123' and '2310') are highlighted in Fig. 5.2(c) to appreciate that their behavior is equivalent to the one found for $D = 3$ ('012' and '210'), and $D = 2$ ('01' and '10'). For the sake of clarity, Fig. 5.2(d) displays the probabilities of words of length $D = 4$ computed from surrogate data (shuffled inter-dropout intervals time series), and it can be confirmed that in this case the probabilities are all within the gray region, as expected from a sequence of events that are not correlated.

For the sake of completeness, additional experiments were performed to compare with, employing different lasers and feedback conditions, to verify that this hierarchical and clustered behavior is indeed a general feature. Figure 5.3(a) displays the probabilities computed with the same laser as in Figs. 5.1 and 5.2, but with weaker feedback strength, resulting in a threshold reduction of 4%. For a better comparison, Figs. 5.3(b,c) display the probabilities computed with data analyzed in the previous chapter for 18C (a) and 20C (b). Also the two clusters and the crossover (such that the word '210' becomes the most probable one at high current) are seen in these data sets.

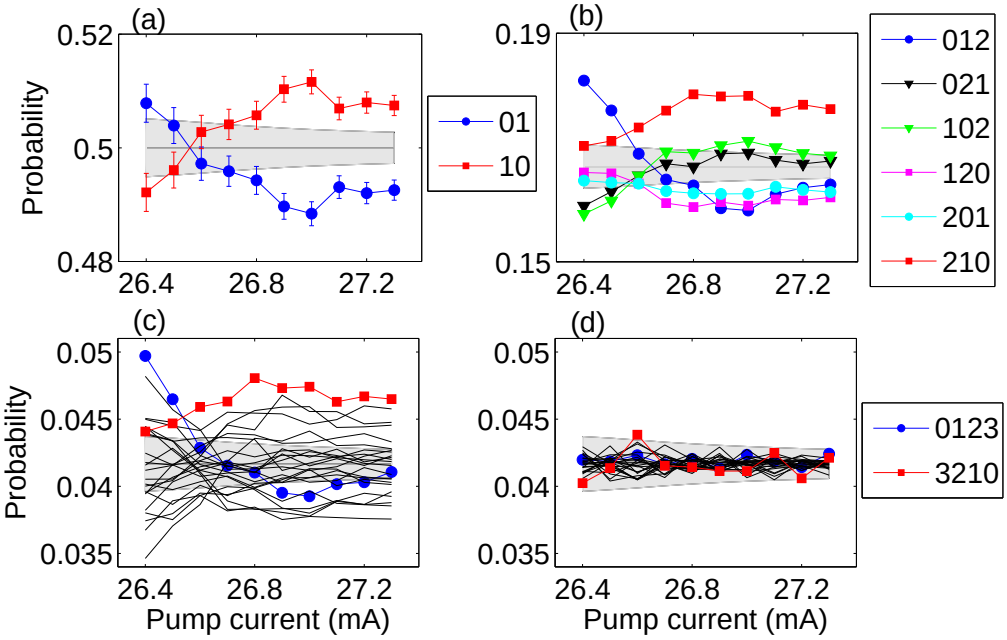

Figure 5.2: (a) Words probabilities for $D = 2$. The crossover in the probabilities also appears around 26.6 mA. (c) Words probabilities for $D = 4$. Highlighted in red is the word '3210', and in blue the word '0123'. The behavior of these two words is the same as the one of words '210', and '012' for $D = 3$ (b). The crossover is also appreciated in this case. Panel (d) displays the probabilities for $D = 4$ computed from the surrogated data (shuffled inter-dropout intervals time series).

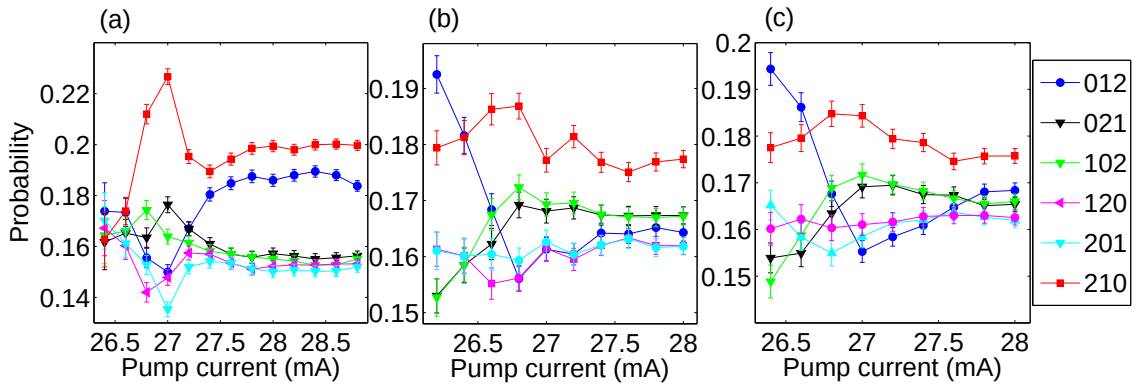

Figure 5.3: Words probabilities computed from data recorded using different experimental conditions. Panel (a) present the analysis of the data from the same experimental conditions as in Fig. 5.1 but with a threshold reduction of 4%. Panels (b) and (c) present the probabilities from the experiments presented in *Chapter 4*, were a different laser was used (Hitachi Laser Diode HL6724MG) in a shorter external cavity (45 cm) and a feedback leading to a threshold reduction of 7%. Panel (b) corresponds to a working temperature of 18C and panel (c) to 20C.

5.3.2 Correlation analysis

To further corroborate the presence of correlations in the dropout sequence, the usual autocorrelation coefficients are computed for the sequence of inter-dropout intervals, $\{\Delta T_i\}$, as

$$C_n = \frac{\langle (\Delta T_i - \langle \Delta T \rangle)\,(\Delta T_{i-n} - \langle \Delta T \rangle) \rangle}{\sigma^2}, \tag{5.1}$$

where $n \in N$ is the order of the correlation (the delay considered to compute the autocorrelation), σ is the standard deviation of the intervals (ΔT_i), and $\langle \Delta T \rangle$ is the mean value of the sequence of intervals. The result is shown in Fig. 5.4, that displays C_1 (first-order autocorrelation) and C_2 (second-order autocorrelation) vs. the pump current for the experimental data. First-order correlations are clearly identified, which are stronger at low pump currents, while second-order correlations are significantly weaker.

From these results it can also be confirmed that the symbolic ordinal analysis indeed provides additional information with respect to the usual correlation analy-

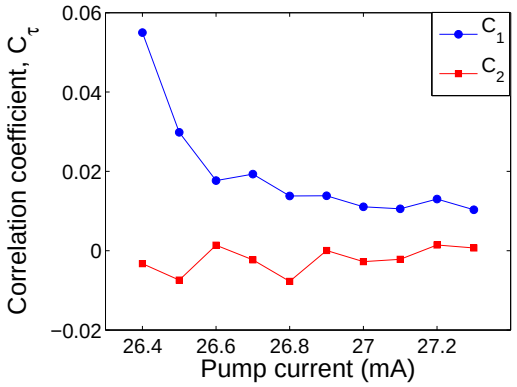

Figure 5.4: First and second order correlation coefficient of the inter-dropout interval sequence, C_1 and C_2 [Eq. 5.1], computed from the experimental data, as a function of the laser pump current.

sis. In particular, it is noticed that C_1 is positive for all current values; however, in Fig. 5.2(a) it is seen that at high currents the word '10' is more probable (i.e., $\Delta T_i > \Delta T_{i+1}$ is more probable than $\Delta T_i < \Delta T_{i+1}$), and at low currents, it is the opposite situation (the word '01' is more probable, and thus, $\Delta T_i < \Delta T_{i+1}$ is more probable than $\Delta T_i > \Delta T_{i+1}$). This is apparently contradictory; however, one should keep in mind that the ordinal analysis takes into account the relative values of consecutive intervals, while the correlation coefficient, takes into account the magnitude of consecutive $\Delta T_i - < \Delta T >$ values. Moreover, Fig. 5.4 shows that C_2 is very small, suggesting negligible correlations; notwithstanding the probabilities of the words of length $D = 3$ are clearly not consistent with the N.H.

5.3.3 Comparison with the LK model.

To further check the robustness of the observations, simulations of the LK model [83] (introduced in *Section 2.4*) were performed. The model predicts a fast pulsing behavior, in the picosecond time-scale that, after being properly filtered out (to account for the bandwidth of experimental measurements), gives a sequence of dropouts in good agreement with the observations.

Within the framework of the LK model it has been shown that the dropouts are often a transient dynamics, even when noise is included in the simulations, and

the duration of the transient increases with the pump current parameter [34, 35]. In order to compute long time series of inter-dropout intervals, when the trajectory finds a stable fixed point, the simulation is re-started with new random initial conditions. Simulations of 2 milliseconds are performed, obtaining time series containing between 12,000 and 48,000 events, for low and high pump currents, respectively.

Because the LK model is a simple model (it takes into account only one reflection in the external cavity, it neglects multi-mode emission, spatial effects, and thermal effects; in particular the shift of the emission wavelength with increasing current due to Joule heating), only a qualitative agreement could be expected.

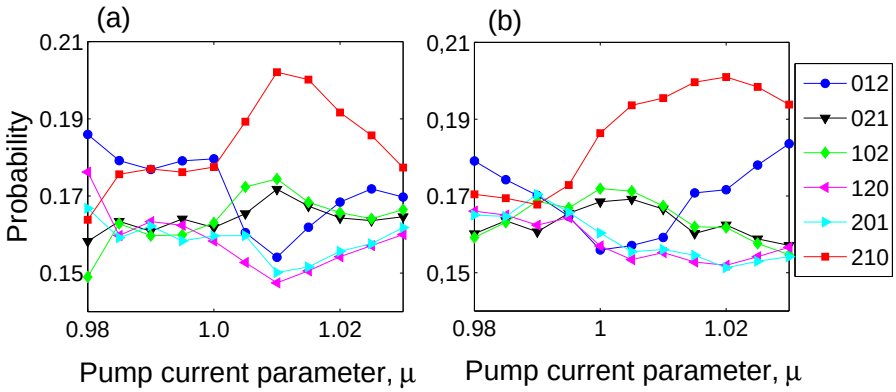

Figure 5.5: Probabilities of the ordinal patterns computed from simulations of the LK model. (a) The feedback strength is $\eta = 10$ ns^{-1}, and $\alpha = 4$. (b) The feedback strength is 20 ns^{-1}, and $\alpha = 4.5$. The hierarchy in the word probabilities, the clustering and the crossover are the same as in the experimental data, Fig. 5.1.

Figures 5.5(a) and 5.5(b) show the numerically calculated word probabilities vs. the laser pump current parameter of the model, μ, for two sets of parameters. Typical values of the parameters were used in the simulations: $k = 300$ ns^{-1}, $\gamma = 1$ ns^{-1}, $\epsilon = 0.01$, $\tau = 5$ ns, and $\beta_{sp} = 10^{-4}$ ns^{-1}. In Fig. 5.5(a), the feedback parameter is $\eta = 10$ ns^{-1}, and $\alpha = 4$; in Fig. 5.5(b), $\eta = 20$ ns^{-1}, and $\alpha = 4.5$.

The simulations agree qualitatively well with the experimental findings: the same hierarchical and clustered organization of patterns is observed, as well as the same crossover. Figures 5.5(a) and 5.5(b) also point to the robustness of the results, as the two clusters are present in simulations with different feedback strengths.

5.4 Influence of the detection threshold

A sensitive issue in the dropout detection is the choice of the detection threshold. Due to the fact that not all the dropouts are equally deep, and to the presence of noise in the time trace, different thresholds could lead to different dropout detections. When computing the word probabilities, the hierarchy might, in principle, be different for each detection threshold.

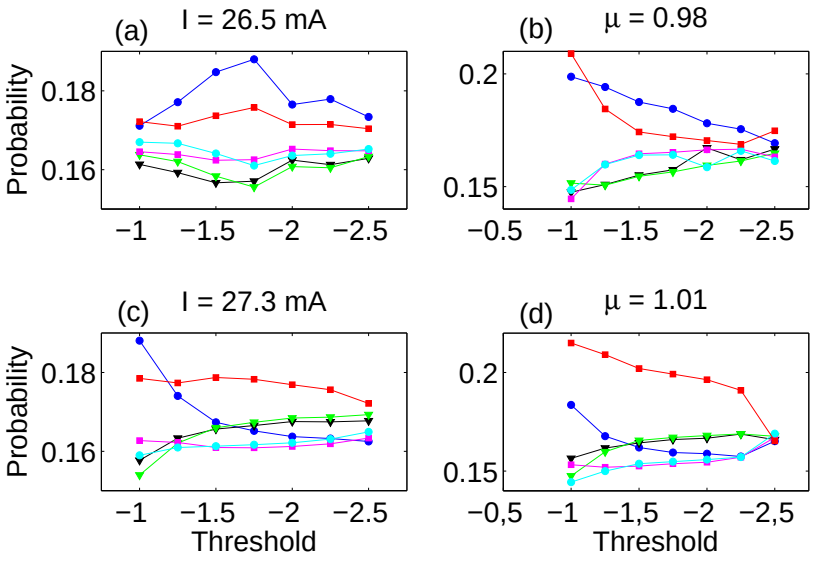

Figure 5.6: Probabilities of the words vs. the detection threshold is shown for different pump current values both, for the experimental (a,c) and the simulations (b,d) data. The hierarchy of the probabilities remains for most of the detection thresholds.

That is why an analysis of the influence of the detection threshold in the probabilities of the ordinal patterns is required. Figure 5.6 shows the probabilities of the words vs. the detection threshold for two different pump current values of the experimental data (a and c) and two different values of the pump parameter, μ, of the LK model (b and d). The corresponding time traces are depicted in Fig.5.7. It can be appreciated that, while the values of the probabilities vary with the threshold, the hierarchy and the clusters ('021'-'102' and '120'-'201') are robust and occur in a wide range of threshold values. While for too low (or too deep) thresholds the probabili-

ties vary significantly (as too many or too few dropouts are detected), the presence of the two clusters is robust to threshold variations in a wide range of thresholds.

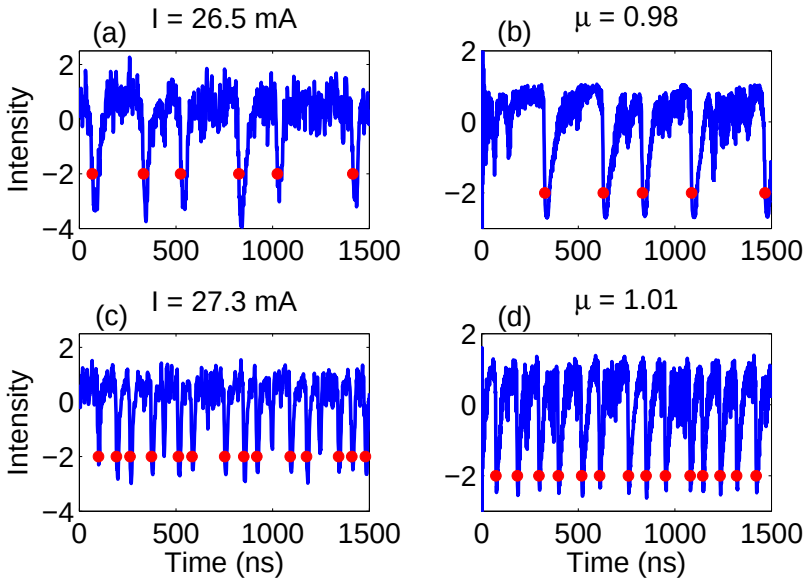

Figure 5.7: Time series for two different pump currents of the experimental data (a,c), and two different values of the pump parameter, μ, of the LK model (b,d). Red dots indicate the dropout detection, indicated at a threshold of -2.

Most importantly, the variation of the probabilities with the threshold is qualitatively the same in the experimental and in the numerical data. The same hierarchy and clusters are seen. This is remarkable because the model used for the simulations is the simplest rate equation model, as mentioned before, and the filter used to simulate the finite detection bandwidth is also a simple moving-average window.

While an optimal threshold could be defined for each pump current (that is in the center of the plateau where the probabilities do not vary significantly with the threshold), for the sake of simplicity, it is used a fixed threshold value, equal to -2, for detecting the dropouts.

5.5 A minimal model: the modified circle map

A relevant question is whether the hierarchical and clustered organization of symbolic patterns uncovered here also occurs in other natural systems. If this is the case, there

should be a minimal model that also displays such organization of ordinal patterns. Several iterative maps have been analyzed with the symbolic analysis, and it has been found one surprisingly simple, a modified circle map, that reproduces the hierarchy and clustered organization of the word probabilities.

The modified circle map was proposed by Neiman and Russell [48] to describe serial correlations in electroreceptors of paddlefish. It describes the dynamics of a forced oscillator. The map equation is given by:

$$\phi(i+1) = \phi(i) + \rho + \frac{K}{2\pi}[\sin(2\pi\phi(i)) + \alpha_c \sin(4\pi\phi(i))] + \beta_c \xi(i) \tag{5.2}$$

The parameter ρ is proportional to the ratio between the period of the forcing and the natural period of the oscillator, K is proportional to the forcing amplitude, α_c represents the strength of a second harmonic component, and β_c represents the strength of stochastic fluctuations (ξ being a Gaussian white noise). Considering that the values $\phi(i)$ can represent the dropout times, the time series of phase increments, $\Delta\phi(i) = \phi(i+1) - \phi(i)$, are analyzed in analogy with the inter-dropout intervals, ΔT_i.

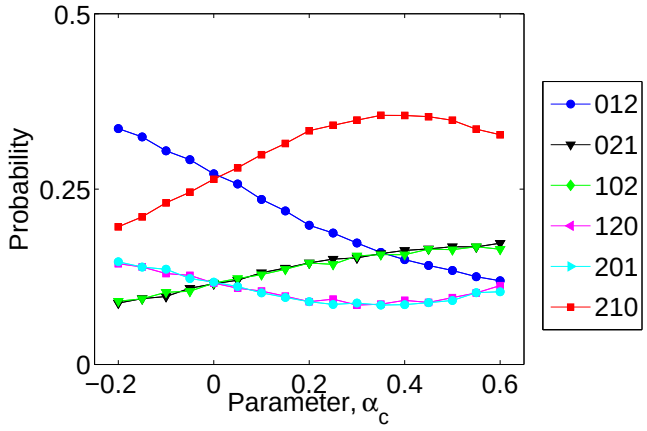

Figure 5.8: Probabilities computed from the minimal model, Eq. 5.2. The parameters are: $\rho = 0.23$, $K = 0.04$ and $\beta_c = 0.002$. The hierarchy in the word probabilities, the clustering and the crossover are the same as in the experimental data (Figs. 5.1, 5.3) and as in the LK numerical simulations (Fig. 5.5).

Figure 5.8 shows the probabilities obtained from the modified circle map vs. the map parameter, α_c. It is noted that the effect of varying α_c corresponds, qualitatively,

to varying the laser pump current: a similar behavior as in the experimantal data (Figs. 5.1, 5.3) and the LK numerical simulations (Fig. 5.5) can be observed. There is the same hierarchy in the probabilities, which undergoes the same crossover. The existence of the two clusters is also remarkable, formed by the same words as in the sequence of optical dropouts.

The symbolic behavior of the modified circle map demonstrates that it is an adequate minimal model for representing qualitatively the symbolic dynamics underlying the sequence of optical dropouts. Considering the high-dimensionality of the laser dynamics (induced by the feedback delay time), it is unexpected and remarkable that a simple iterative model with only one variable can mimic the extended correlations present in the sequence of dropouts.

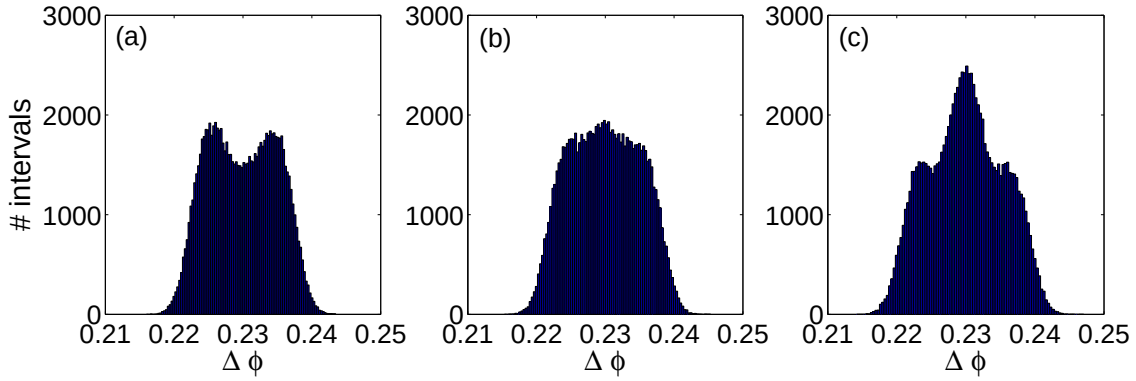

Figure 5.9: Histograms of the intervals, $\Delta\phi(i) = \phi(i+1) - \phi(i)$, form the modified circle map, for three values of the map parameter. (a) $\alpha_c = -0.1$, (b) $\alpha_c = 0.3$, and (c) $\alpha_c = 0.5$. Parameters as in Fig. words$_c ircle$

However, the good agreement between the LFF dynamics and the modified circle map model is restricted to the symbolic ordinal analysis, and it does not describe the statistical distribution of event intervals. Figure 5.9 shows the histograms of the intervals $\Delta\phi(i) = \phi(i+1) - \phi(i)$ for three values of the model parameter α_c (-0.1, 0.3 and 0.5), and it is shown that these histograms are not equivalent to the ones obtained from the IDIs, presented in *Chapter 2* (Fig. 2.11).

5.6 Transition probabilities

From the sequence of words, additional information can be extracted by computing the transition probabilities (TPs) [130] from one word to the next. In Fig. 5.10, the transitions '01'→'10' and '01'→'01' are depicted as examples.

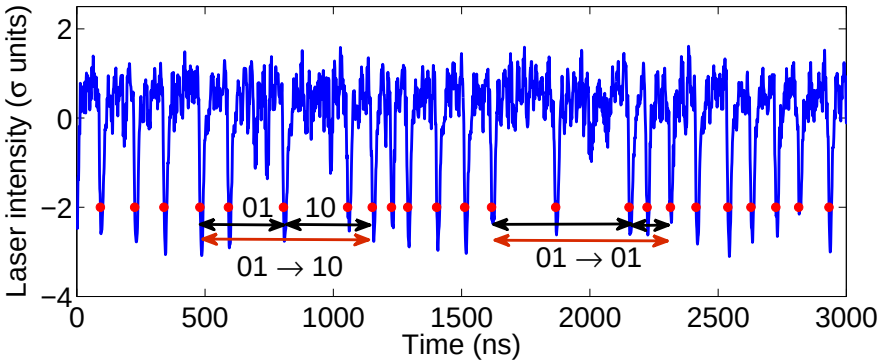

Figure 5.10: Time trace of the laser at I = 27.2 mA. Two transitions are depicted as examples $'01 \rightarrow 01'$ and $'01 \rightarrow 01'$.

The TP analysis with $D = 2$ words can uncover correlations among five consecutive dropouts, and thus allows to extract information about the memory of the system in a longer time scale. The TPs can be normalized in two different ways:

i) Normalized for each word i,

$$TP_{i\rightarrow j} = \frac{\sum_{t=1}^{N-1} n(s(t) = i, s(t+1) = j)}{\sum_{t=1}^{N-1}(s(t) = i)}, \tag{5.3}$$

where n is a count of the number of occurences, N is the length of the symbolic sequence $s(t)$, and t is the position of the OP in the sequence. In this case, $\sum_j TP_{i\rightarrow j} = 1 \; \forall \; i$.

ii) Normalized for all transitions $i \rightarrow j$,

$$TP^*_{i\rightarrow j} = \frac{\sum_{t=1}^{N-1} n(s(t) = i, s(t+1) = j)}{N-1}. \tag{5.4}$$

In this case the sum of all possible TPs is one, $\sum_{i,j} TP^*_{i\rightarrow j} = 1$.

This analysis, which uncovers correlations among five consecutive dropouts, can be performed with shorter time series (as only 4 TPs are computed) in comparison

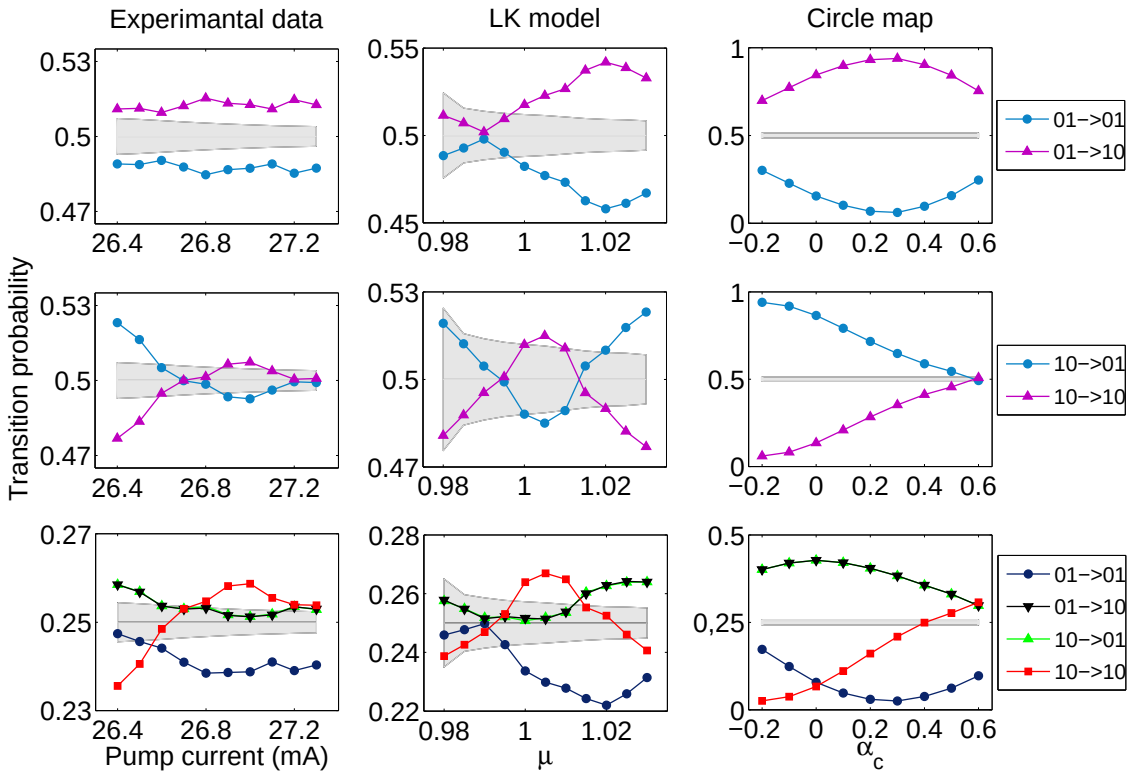

Figure 5.11: Transition probabilities for the experimental data (left column), the LK numerical simulations (center column), and the circle map numerical simulations (right column). The first row indicates the transition probabilities from word '01' to '01' and '10', such that $TP_{(01\to01)} + TP_{(01\to10)} = 1$. The second row indicates the transition probabilities from word '10' to words '01', and '10', such that $TP_{(10\to01)} + TP_{(10\to10)} = 1$. The third row considers all four transitions, such that $TP_{(01\to01)} + TP_{(01\to10)} + TP_{(10\to01)} + TP_{(10\to10)} = 1$. Parameters are as in Fig. 5.5(b) (LK model), and as in Fig. 5.8 (circle map).

with the length of the data required to compute the 24 $D = 4$ words with robust statistics. The transition probabilities are depicted in Fig. 5.11, where the left column corresponds to the experimental data, the center column to the LK numerical simulations, and the right column to circle map numerical data. For the first normalization of the TPs, the first-row shows the transitions from word '01' to words '01' and '10', while the second-row shows the transitions from word '10' to words '01' and '10'. The third-row corresponds to the second normalization (TP*).

The results in Fig. 5.11 confirm that, also at this time scale, there is a non-trivial structure of the ordinal patterns, and the crossover from low to intermediate pump currents ($I \sim 24.6$ mA, $\mu \sim 0.99$, and $\alpha_c = 0$) is also present.

5.7 Delay embedding analysis.

Another well-known method to unveil the hidden structure in a timer series, which allows reconstructing the attractor in phase space, is to compute a delay embedding of the inter-dropout intervals [92]. This method compares the values of the time sequence at different times, considering a embedding dimension m: $\{\Delta T_i, \Delta T_{i+m}, \Delta T_{i+2m}\}$. To explore this method, several embedding dimensions are considered, and the three-dimensional reconstruction of the attractor, for the experimental and for the simulated data, are plotted in Fig. 5.12. The first row corresponds to a embedding dimension *m=1*, (i.e., $\{\Delta T_i, \Delta T_{i+1}, \Delta T_{i+2}\}$), the second row to *m=2* (i.e., $\{\Delta T_i, \Delta T_{i+2}, \Delta T_{i+4}\}$), and the third row to *m=3* (i.e., $\{\Delta T_i, \Delta T_{i+3}, \Delta T_{i+6}\}$). This embedding dimension analysis is depicted for the experimental data (left column for I=26.4 mA), the LK model simulations (center column for $\mu = 0.985$), and the circle map (right column for $\alpha_c = 0.2$), where $\Delta\phi(i) = \phi(i) - \phi(i-1)$.

No well-defined attractor can be inferred by this technique, but rather an apparently random cloud of data points. This reinforces the relevance of the symbolic ordinal method used in this thesis, that it can unveil an underlying structure in the sequence of inter-dropout intervals, which can not be revealed by the reconstruction of the trajectory method. In the case of the circle map model (right column of 5.12) a noisy but clear structure can be appreciated. Therefore, the suitability of the circle map to describe the LFFs dynamics of a semiconductor laser with feedback is limited

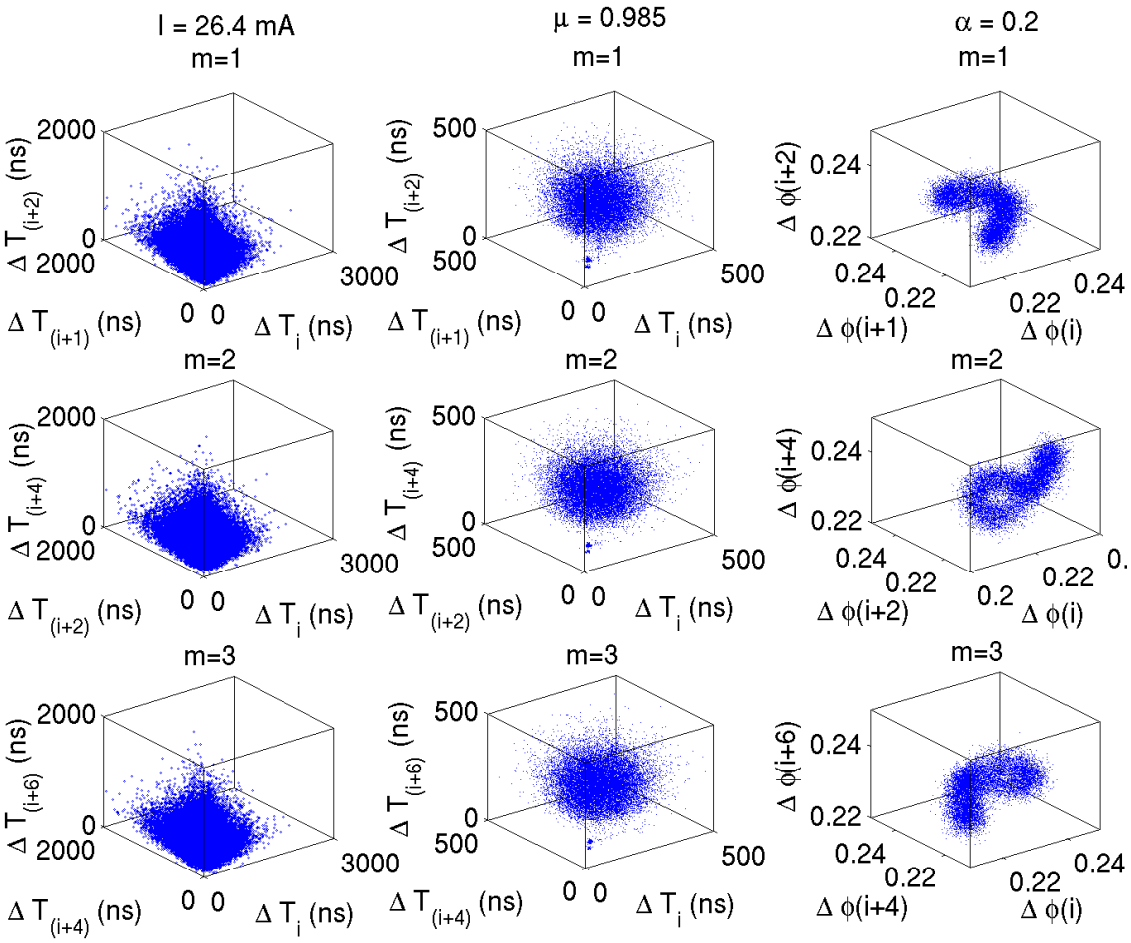

Figure 5.12: Three-dimensional delay embedding of the inter-dropout interval time series for the experimental data (left column), for the numerical simulations with the LK model (middle column), and for the minimal model (right column). For the minimal model, $\Delta\phi(i) = \phi(i) - \phi(i-1)$, following equation 5.2. The embedding dimensions plotted are $m = 1$ (top row), $m = 2$ (middle row), and $m = 3$ (bottom row).

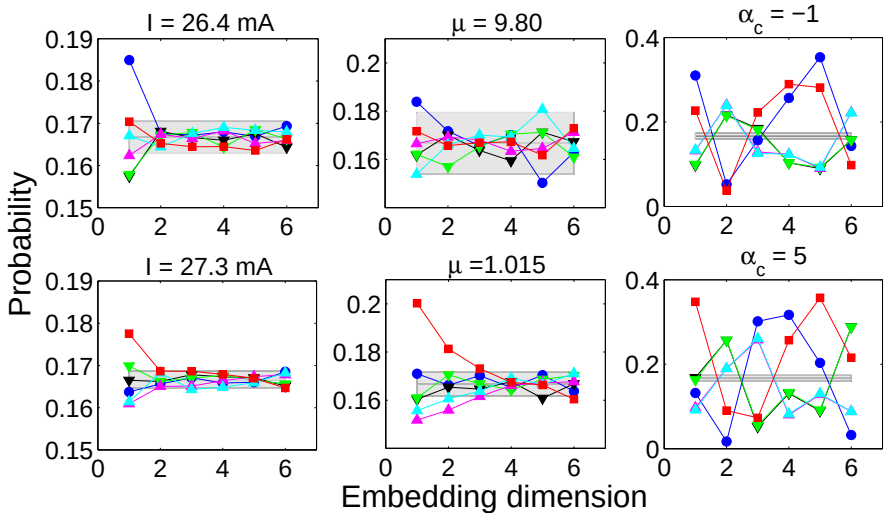

Figure 5.13: Probabilities of the words versus the delay embedding for two different pump currents. Experimental data (left column), and numerical data from the LK model(centre column), and numerical data from the circle map (right column).

to the symbolic dynamics of the sequence of dropouts, and the dimensionality of the dynamics or the statistical distribution of inter-dropout interval values are not well described by this minimal model.

To analyze the length of the serial correlations present in the sequence of inter-dropout intervals, the words are now constructed using a delay m, i.e., the words are formed as (ΔT_i, T_{i+m}, ΔT_{i+2m}). The probabilities of the words defined in this way are presented in Fig. 5.13, for the experimental data (left column), for the numerical data from the LK model (middle column), and for the numerical data from the circle map (right column). For the experimental data and the LK model simulations, the probabilities are outside the gray region (consistent with the null hypothesis) only for the lowest embedding dimension, revealing that the serial correlations only extend to a few inter-dropout intervals.

Again, for the circle map the result do not agree with the experiments for this type of analysis, confirming the limitations of the modified circle map to fully describe the LFF dynamics.

5.8 Summary

In this chapter, it has been demonstrated, in the experiments and in the LK model simulations, the existence of serial correlations in the LFF dynamics. A hierarchical organization of patterns in the symbolic dynamics has been found, that displays a clustered structure, which has not been previously noticed, despite the great attention that the laser dropout dynamics has attracted. Simulations of the LK model have been found to be in good qualitative agreement with the experimental observations. This good qualitative agreement experiment-simulations indicate that this organization of symbolic patterns is a fingerprint of the topology of the attractor underlying the LFF dynamics, and provides a validation of the LK model in unprecedent long time-scale. Also a minimal model has been found, that describes the hierarchical and clustered symbolic structure. However, this minimal model fails to describe other features, such as the IDI distribution or linear correlations.

In the next chapter the suitability of the circle map model is verified, by analyzing the symbolic dynamics of the LFFs under external periodic forcing.

Chapter 6

Symbolic dynamics of a semiconductor laser with current modulation in the LFF regime

You must feel the force around you!
Joda master (The empire strickes back)

6.1 Introduction

As discussed in the previous chapters, the LFF dynamics results from the interplay of the nonlinear light-matter interactions with a time delayed perturbation and noise. A natural extension of this dynamical system, which is of special relevance, is achieved by introducing an external periodic forcing to the system. This physical system is relevant in telecommunications, as information in encoded by direct modulation of the laser pump current [60], and it is also of great interest because of the various dynamical regimes that can arise [68, 69, 71].

In particular, the LFF dynamics has previously been studied in detail when the laser current is periodically modulated [30, 31, 50, 142–144], not only because the LFFs can be supressed via current modulation [49], but also from a complex systems perspective, because the interplay of nonlinearity, noise, periodic forcing and delayed

feedback leads to entrainment and synchronization [30, 31], providing a controllable experimental setup for studying these phenomena. In addition, because the LFF dynamics is excitable, the influence of external forcing has also attracted attention from the point of view of improving our understanding of how excitable systems respond to external signals to encode information [69, 143, 145–147].

In this chapter, the Bandt and Pompe symbolic ordinal analysis is used to study the transition from the LFF dynamics of the un-modulated laser, where the parameters are such that the dropouts reveal only weak signatures of an underlying deterministic attractor [139], to the modulated LFF dynamics, which consists of more regular dropouts, with a periodicity that is related to the external forcing period [30]. By increasing the modulation amplitude, it is found a gradual transition from a mainly stochastic to a mainly deterministic behavior, and the transition characteristic features are identified, which are fingerprints of the underlying topology of the phase space of the system.

Clear changes are identified in the symbolic dynamics as the modulation amplitude increases. Specifically, the analysis uncovers the presence of serial correlations in the sequence of dropouts, and reveals how they are modified by the amplitude of the external forcing.

It is shown that simulations of the LK model [83] are in good qualitative agreement with the experimental observations. Furthermore, the modified circle map model introduced in *Chapter 5* is shown to describe succesfully also the symbolic dynamics of the modulated laser, showing the robustmess of this minimal model to describe the symbolic LFF dynamics.

The experiments presented in this chapter were performed by Taciano Sorrentino and the author, and the numerical simulations of the Lang and Kobayashi model were performed by Sandro Perrone. The numerical simulations of the circle map were performed by the author.

The results presented in this Chapter have been sumarized in [148].

6.2 Experimental setup

The experimental setup is shown in Fig. 6.1. To demonstrate the robustness and the generality of the observations, the experiments were performed with two lasers under different feedback conditions. One experiment was performed with a laser emitting at 650 nm with free-space feedback provided by a mirror. The other experiment was performed with a laser emitting at 1550 nm, with feedback provided by an optical fiber.

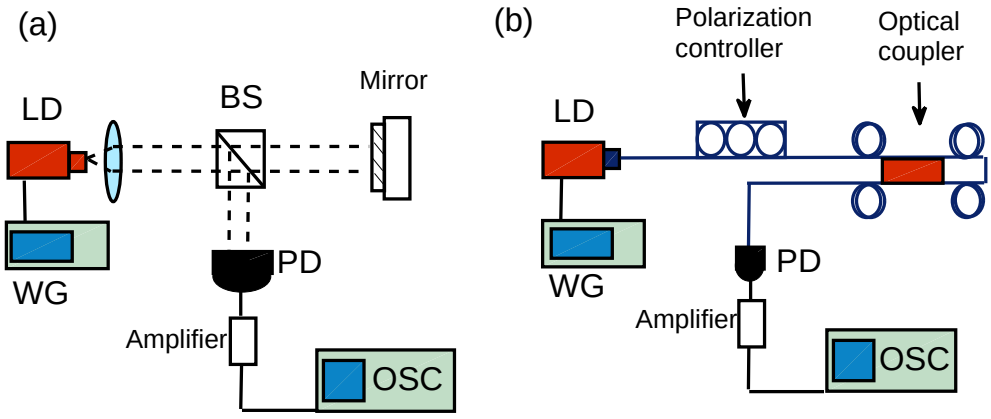

Figure 6.1: Experimental setup for (a) 650 nm laser (Hitachi HL6714G) and (b) 1550 nm laser (Mitsubishi ML925B45F). LD stands for laser diode, BS for beam-splitter, PD for photodetector, WG for waveform generator, and OSC for oscilloscope.

For the 650 nm laser, the external cavity is 70 cm (giving a feedback time delay of 4.7 ns) and the feedback threshold reduction is 8%. A 50/50 beam-splitter sends light to a photodetector (Thorlabs DET210) connected with a 1 GHz oscilloscope (Agilent DSO 6104A). The solitary threshold is 38 mA and the current and temperature (17 C) are stabilized with an accuracy of 0.01 mA and 0.01 C, respectively, using a controller (Thorlabs ITC501). Through a bias-tee in the laser head, a sinusoidal RF component from a leveled waveform generator (HP Agilent 3325A) is combined with a constant dc current of 39 mA. The modulation frequency is $f_{mod} = 17$ MHz and the modulation amplitude varies from 0 mV to 78 mV in steps of 7.8 mV (from 0% to 4% of the dc current in steps of 0.4%). For each modulation amplitude, five measurements of 3.2 ms are recorded, that give a total number of dropouts equivalent

to 16 ms. The time series contain between 74,000 and 207,000 dropouts, at low and high modulation amplitude, respectively.

For the 1550 nm laser, the time delay is 25 ns and the feedback threshold reduction is 10.7%. The solitary threshold is 11.20 mA, the dc value of the pump current is 12.50 mA, the modulation frequency is $f_{mod} = 2$ MHz and the modulation amplitude varies from 0 mV to 150 mV in steps of 10 mV (from 0% to 24% of the dc current in steps of 1.6%). The time series contain between 8,000 and 19,000 dropouts, at low and high modulation amplitude, respectively. While, for the 1550 nm laser, the modulation frequency is about one order of magnitude smaller than for the 650 nm laser, the relation with the characteristic time-scale of the LFF dynamics, given by the average inter-dropout interval $\langle \Delta T \rangle$ is about the same: for the 650 nm laser, $\langle \Delta T \rangle = 365$ ns and thus $\langle \Delta T \rangle \times f_{mod} = 6.2$. For the 1550 nm laser, $\langle \Delta T \rangle = 2.55$ μs and $\langle \Delta T \rangle \times f_{mod} = 5.1$.

6.3 Results

6.3.1 Effect of current modulation on the IDI distribution.

Figure 6.2 displays the intensity time series, the probability distribution functions (PDFs) of inter-dropout intervals, ΔT_i (IDIs), and the return maps, ΔT_{i+1} vs ΔT_i, for four modulation amplitudes for the 650 nm laser. Figure 6.3 is equivalent to Fig. 6.2 but for the 1550 nm laser. As it has been reported in the literature the dropouts tend to occur at the same phase in the drive cycle with current modulation, and the IDIs are multiples of the modulation period [25, 30, 31].

For increasing modulation amplitude, the IDIs become progressively smaller multiples of the modulation period and, for high enough modulation amplitude, the power dropouts occur every modulation cycle [30]. Here, for the highest modulation amplitude, the PDF presents a strong peak at two times the modulation period (see Fig. 6.2(k) and 6.3(k)).

The return maps (third column of Fig. 6.2 and Fig. 6.3) display a clustered structure, with "islands" that correspond to the well-defined peaks observed in the PDFs, also in good agreement with previous reports [25, 30]. These plots of ΔT_{i+1} vs ΔT_i are almost symmetric, suggesting that $\Delta T_{i+1} < \Delta T_i$ and $\Delta T_{i+1} > \Delta T_i$

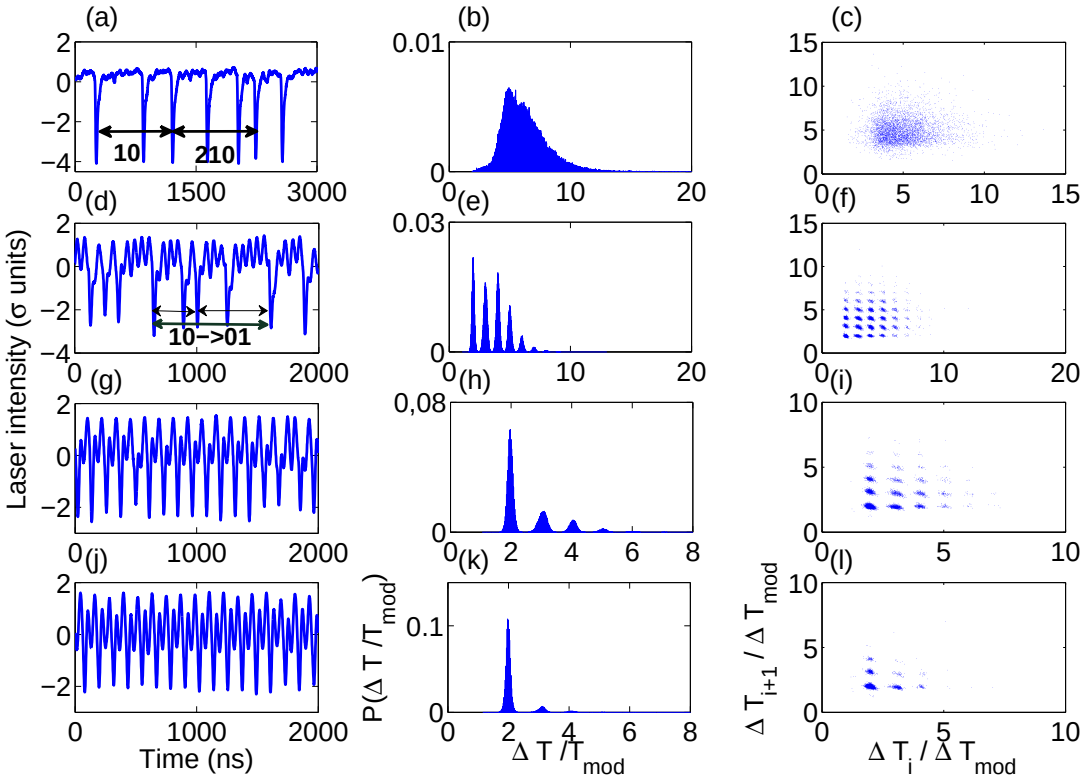

Figure 6.2: For the 650 nm wavelength laser, left column: time traces of the laser intensity; middle column: probability distribution functions (PDFs) of the inter-dropout intervals, ΔT_i (IDIs); right column: return maps (ΔT_{i+1} vs. ΔT_i) in units of the modulation period (T_{mod}). First row: no modulation; seconf row: modulation amplitude of 23.4 mV (1.2% of the dc current); third row: 31.2 mV (1.6%); forth row: 39.0 mV (2%). In panel (a) the words '10' ($D = 2$) and '210' ($D = 3$) are depicted as examples; in panel (d) the transition for '10→01' is depicted as example (see *Section 6.3.3* for details).

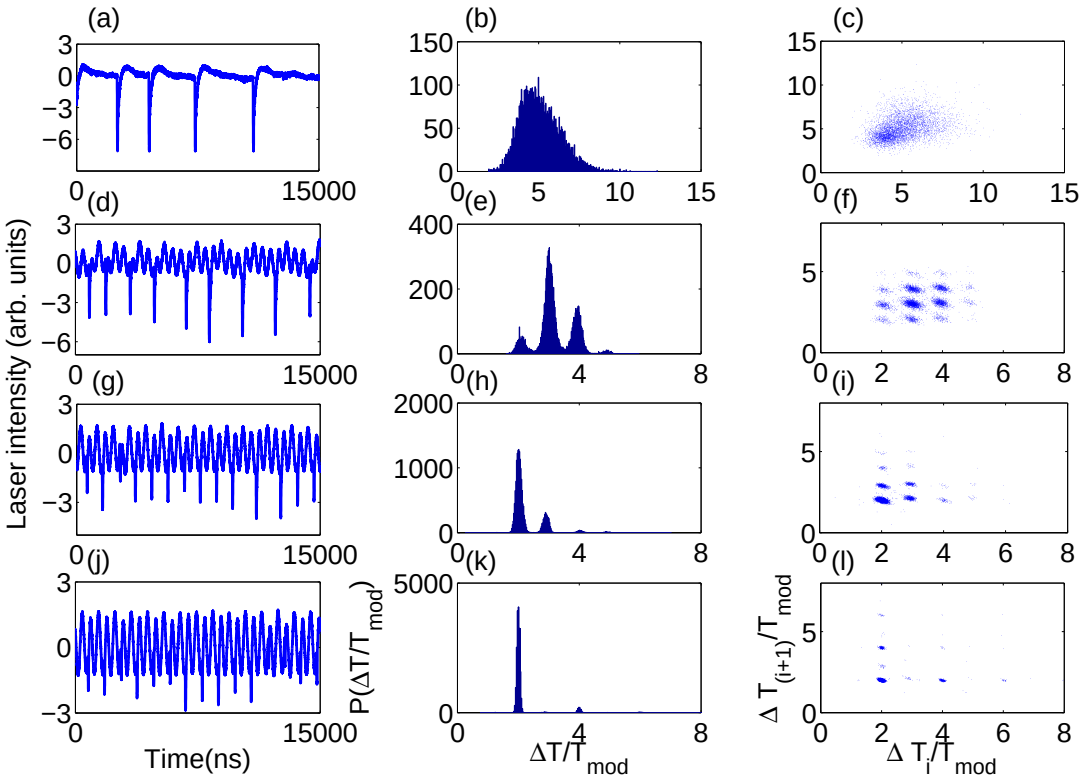

Figure 6.3: For the 1550 nm wavelength laser, left column: time traces of the laser intensity; middle column: probability distribution functions (PDFs) of the inter-dropout intervals, ΔT_i (IDIs); right column: return maps (ΔT_{i+1} vs. ΔT_i) in units of the modulation period (T_{mod}). First row: no modulation; seconf row: modulation amplitude of 40 mV (6.4% of the dc current; third row: 80 mV (12.8%); forth row: 120 mV (19.2%).

are equally probable; however, in the next section it will be demonstrated that the modulation induces correlations in the ΔT_i sequence, induced by the modulation, which can not be inferred from these plots.

6.3.2 Word probabilities

Following with the analysis performed in *Chapters 4* and *5*, here the sequences of IDIs acquired from a modulated laser, are transformed into sequences of words of dimension $D = 2$ and $D = 3$, and their probabilities are computed for the different

modulation amplitudes.

Figure 6.4 shows the probabilities of words of $D = 2$ (a,b) and $D = 3$ (c,d), vs. the modulation amplitude, for the 650 nm laser (a,c), and for the 1550 nm laser (b,d). As in previous chapters, probability values outside the gray regions are not consistent with a uniform distribution of word probabilities and reveal serial correlations in the IDI sequence. It can be noticed that the gray region in (a) and (c) is narrower than in (b) and (d). This is due to the fact that the number of dropouts recorded for the 650 nm laser is much larger than for the 1550 nm laser (the corresponding delay times being 4.7 ns and 25 ns respectively).

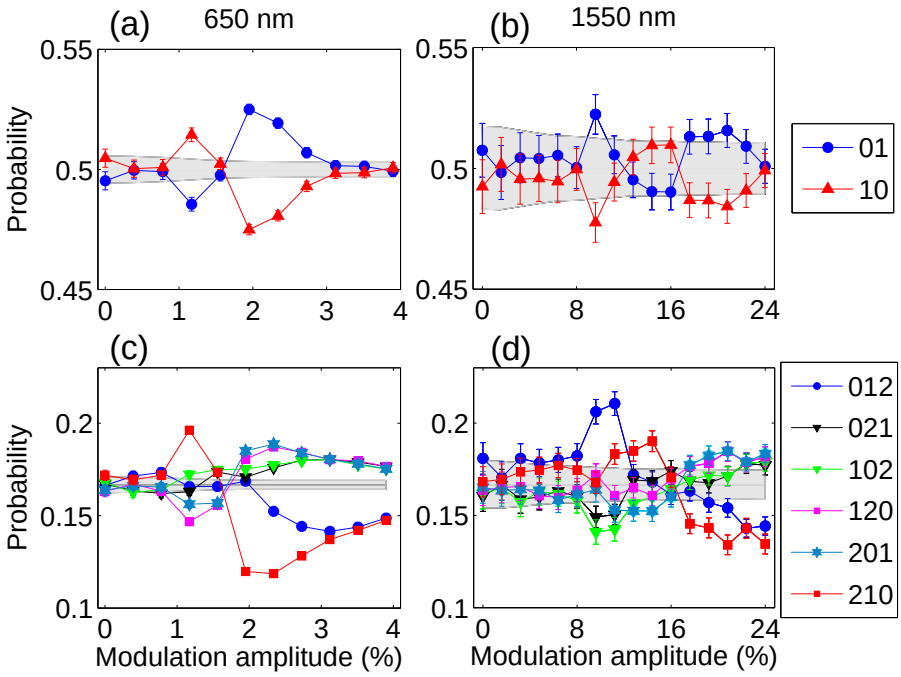

Figure 6.4: Probabilities of the words of $D = 2$ (a,b) and $D = 3$ (c,d) versus the modulation amplitude for the experiment with the 650 nm laser (a,c), and the experiment with the 1550 nm laser (b,d).

It is observed that, for the case of $D = 2$, the dynamics is consistent with the NH for small and for high modulation amplitudes. However, the analysis with $D = 3$ reveals that, for high modulation, the probabilities are outside the gray region, revealing correlations among four consecutive IDIs, which are not detected with the

$D = 2$ analysis. It can also be noted that there are two groups of words for $D = 3$, one less probable ('012', '210') and one more probable ('021','102', '120', '201'), resulting for $D = 2$ in the same probabilities for '01' as for '10'. With $D = 3$, the less probable words are those which imply three consecutively increasing or decreasing IDIs. This can be understood in the following terms: strong enough modulation forces a rhythm in the LFF dynamics, and three consecutively increasing or decreasing intervals imply a loss of synchrony with the external rhythm, and thus, are less likely to occur.

Also, in Fig. 6.4(c) and (d), it can be observed the same two clusters of words already found in *Chapter 5* for the laser without external forcing. These clusters of $D = 3$ words can be seen for all values of the modulation amplitude, remaining even under the strong external forcing.

6.3.3 Transition probabilities

In *Section 5.6* the transition probabilities (TPs) from one word of $D = 2$ to the next word were introduced (see Fig. 6.2(d) for an example of $\mathrm{TP}_{10\to01}$). Figure 6.5 depicts the four transition probabilities for both sets of experiments, vs. the modulation amplitude. The left column corresponds to the 650 nm laser experiment, and the right column to the 1550 nm laser experiment. For the first normalization of the TPs, the first-row shows the transitions from word '01' to words '01' and '10' (such that $TP_{01\to01} + TP_{01\to10} = 1$), and the second-row the transitions from word '10' to words '01' and '10' (such that $TP_{10\to01} + TP_{10\to10} = 1$). The third-row corresponds to the normalization which considers all four transitions (such that $\sum_{i,j=1}^{i,j=2} TP^{*}_{i\to j} = 1$).

As can be seen in Fig. 6.5, at this time scale the dynamics is still consistent with the NH for low modulation amplitudes but, as the modulation increases, a transition takes places and the TPs display a deterministic-like behavior. This transitions occur at the same values as in Fig. 6.4 (at about 1.8% modulation amplitude for the 650 nm case, and 16% for the 1550 nm case).

Figure 6.5 shows that, for high modulation amplitude, the most probable transitions are the ones that go from one word to the same word ('$01 \to 01$' and '$10 \to 10$'). The transition in the dynamics, and the qualitative agreement between both experiments, are independent of the type of normalization used to compute the TPs.

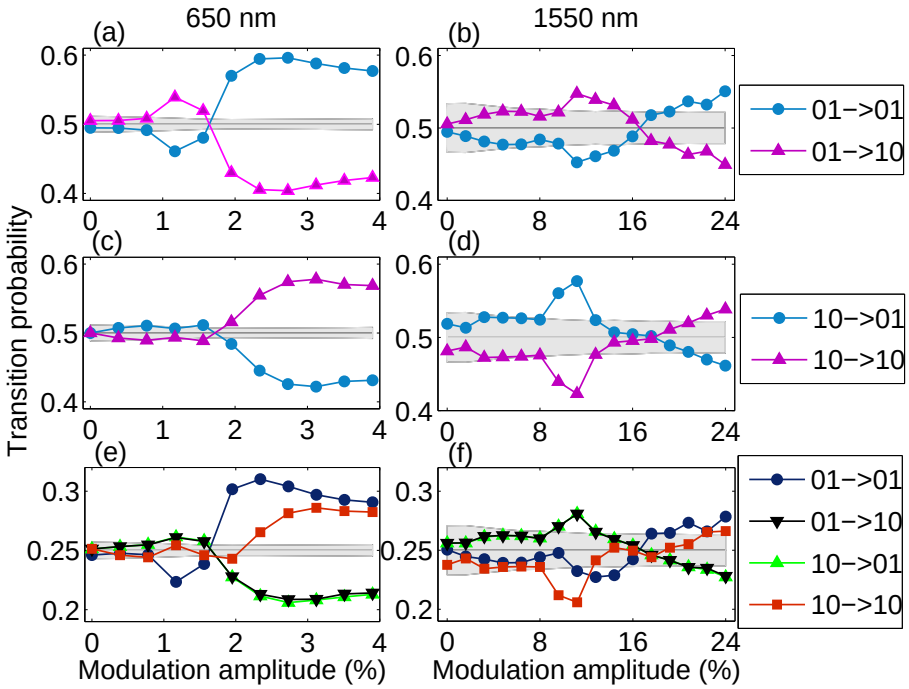

Figure 6.5: Transition probabilities for the 650 nm laser (a, c), and for the 1550 nm laser (b, d). The first row indicates the transition probabilities from word '01' to '01' and '10', such that $TP_{(01\rightarrow01)}+TP_{(01\rightarrow10)} = 1$. The second row indicates the transition probabilities from word '10' to '01' and '10', such that $TP_{(10\rightarrow01)}+TP_{(10\rightarrow10)} = 1$, while the third row consideres all four transitions, such that $TP^*_{(01\rightarrow01)}+TP^*_{(01\rightarrow10)}+TP^*_{(10\rightarrow01)}+TP^*_{(10\rightarrow10)} = 1$.

6.4 Comparison with the LK model and with the modified circle map.

6.4.1 The LK model

For simulating the dynamics with current modulation, a time-dependent pump current parameter has to be considered in the LK rate equation 2.4. In this case $\mu = \mu_0 + a\sin(2\pi f_{mod} t)$, where a is the modulation amplitude, f_{mod} is the modulation frequency, and μ_0 is the dc current. Simulations of 2 ms length were performed. The intensity time-series were averaged over a moving window of 1 ns to simulate the bandwidth of the experimental detection system. The averaged time series contain between 12,000 and 30,000 dropouts for low and high modulation amplitude, respectively.

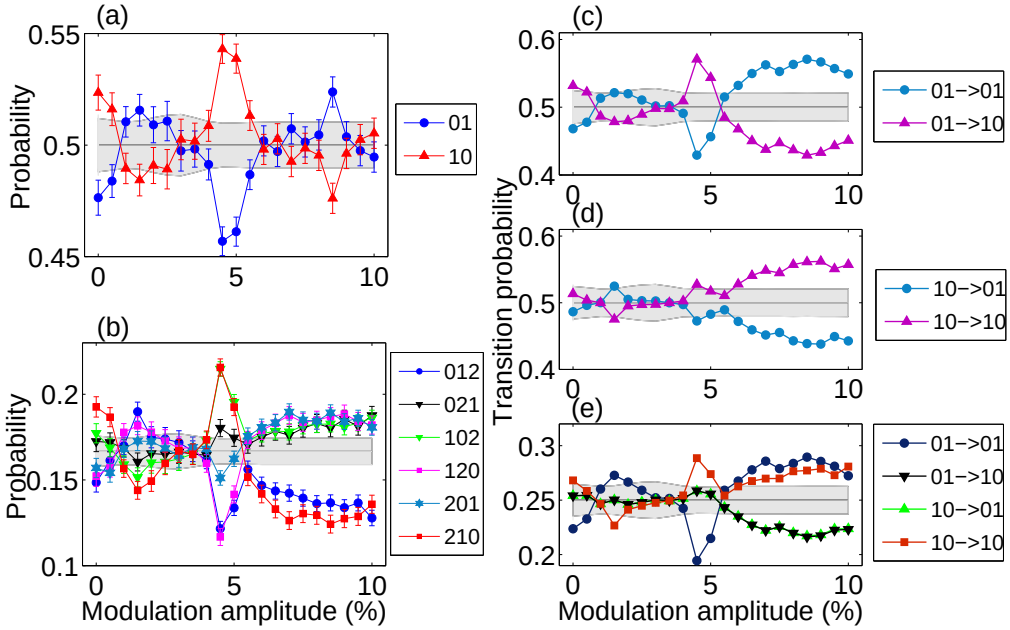

Figure 6.6: Words probabilities for $D = 2$ (a) and for $D = 3$ (b) for the simulations with the LK model. (c) Transition probabilities from word '01' to '01' and '10', such that $\mathrm{TP}_{(01\to01)}+\mathrm{TP}_{(01\to10)} = 1$. (d) Transition probabilities from word '10' to '01' and '10', such that $\mathrm{TP}_{(10\to01)}+\mathrm{TP}_{(10\to10)} = 1$. (e) Transition probabilities such that $\mathrm{TP}^*_{(01\to01)}+\mathrm{TP}^*_{(01\to10)}+\mathrm{TP}^*_{(10\to01)}+\mathrm{TP}^*_{(10\to10)} = 1$.

The best agreement with the experimental data was obtained for $\mu_0 = 1.01$, $f_{mod} = 21$ MHz, $\epsilon = 0.01$, $k = 300$ ns^{-1}, $\tau = 5$ ns, $\gamma = 1$ ns^{-1}, $\beta_{sp} = 10^{-4}$ ns^{-1}, $\eta = 10$ ns^{-1}, and $\alpha = 4$. For these parameters $\langle \Delta T \rangle = 127$ ns and $\langle \Delta T \rangle \times f_{mod} = 2.7$.

Figure 6.6 shows the words probabilities for $D = 2$ (a) and $D = 3$ (b), and the transition probabilities (c,d,e) computed with the LK numerical simulations. It can be observed a transition in the behavior at around 5% of the modulation amplitude, which is present in the OPs analysis for $D = 3$ and in all the TPs analysis. This transition represents a change in the dynamics, from a stochastic-like behavior, where the OPs and TPs lie in the gray region for low modulation amplitudes, to a deterministic-like behavior for high modulation amplitudes.

Comparing Figs. 6.4, 6.5 and 6.6, a good qualitative agreement is found between experiments and simulations. As discussed in *Section 2.4*, within the framework of the LK model, the LFF dynamics is sustained by spontaneous emission noise, and thus, one could expect only weak correlations in the sequence of dropouts. While this is indeed the case for no modulation or very weak modulation amplitude, larger modulation induces IDI correlations, which are adequately reproduced by the LK model. For strong modulation the reason why some words and transitions are more probable than the others is well understood (as due to the external rhythm imposed by the modulation).

It is to be noted that, without modulation, while in the experimental data the word probabilities are within the NH gray region, in the simulated data they are not. This can be due to a number of model parameters that can be tuned in order to obtain a better fit of the symbolic dynamics without modulation (e.g., the feedback strength, the linewidth enhancement factor, the dc value of the pump current, etc.). Although this deserves further study, the effect of the modulation on the LFF symbolic dynamics is consistent with the experimental observations.

6.4.2 The circle map model

The results presented in *Chapter 5* demonstrated that the circle map considered by Neiman and Russell [48], which included a second harmonic term, reproduces the LFF symbolic dynamics at low and high pump currents. Here it is demonstrated that this minimal model also reproduces the statistics of the symbolic dynamics of

the LFFs with periodic external forcing.

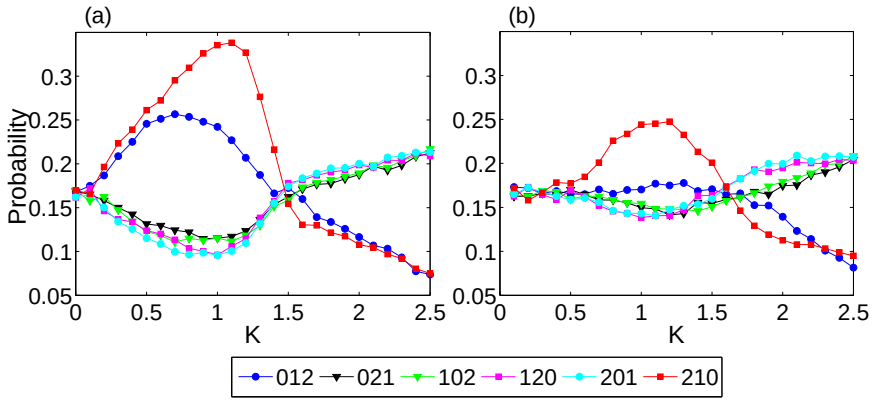

Figure 6.7: Influence of periodic forcing in the probabilities of the ordinal patterns computed from the modified circle map, when varying the parameter K. (a) Probabilities with constant noise strength. Here the hierarchical and clustered structure of the probabilities is in good qualitative agreement with that in the experimental data. The parameters are $\rho = -0.23$, $\alpha_c = 0.2$ and $\beta = 0.002$. (b), Probabilities computed with the modified circle map considering an additional noise strength that decreases with the modulation amplitude. For weak modulation the agreement with the experimental probabilities is further improved.

To show the goodness of the model to describe the dependence of the probabilities with the pump current, in the previous chapter the α_c parameter was varied. The behavior found was equivalent to modify the pump current in the experiments.

In the present situation, the current pumping the laser is a combination of a constant dc current and a sinusoidal component. Now it is not the dc current, but the modulation amplitude of the external forcing, that is varied. Therefore, it is the effect of the K parameter of the circle map model, that corresponds to the forcing strength, that is studied.

Figure 6.7(a) shows the words probabilities versus K. It can be observed that, for high values of K, the probabilities cluster in two groups: the less probable ones, with the words '012' and '210' formed by consecutively increasing and consecutively decreasing intervals; and the more probable ones, where two clusters can be distinguished, '021-102' and '120-201'. This behavior for high K values mimics the one found previously in the experiments and in the simulations with the LK model (Figs. 6.4(c,d) and 6.6(b)).

For the lowest values of the K parameter, all six words are equally probable, being compatible this behavior with a stochastic dynamics, just as in the experiments. For intermediate values of K, clear signatures of determinism appear, where the words '210' and '012' are the most probable ones. This intermediate behavior does not reproduce the experimental results as well as the model does in the un-modulated case. This could be due to the fact that, in the experiments, the current modulation introduces an additional source of noise, which probably depends on the modulation amplitude. In order to test this interpretation, an additional noise term is considered in the map equation. To account for the good agreement at high K values, but the lack of agreement at low and intermediate K values, the additional noise term considered is inversely proportional to the K parameter ($\xi\beta_c/K$):

$$\phi(i+1) = \phi(i) + \rho + \frac{K}{2\pi}[sin(2\pi\phi(i)) + \alpha_c sin(4\pi\phi(i))] + \beta_c(1 + \frac{1}{K})\xi(i) \qquad (6.1)$$

Figure 6.7 (b) shows the new word probabilities with the circle map. This additional noise term mainly affects the word probabilities at low modulation amplitudes (before the crossover), improving the agreement with the experimental probabilities (Fig. 6.4).

Figure 6.8 depicts the transition probabilities, for the two normalization criteria, computed with the circle map. The left column (a, c and e) corresponds to the model with a Gaussian white noise term. As for the word probabilities, there is a good agreement with the experiments for high modulation amplitudes, while not for low modulation amplitudes. The right column (b, d and f) corresponds to the model including the additional noise term, related to the modulation amplitude. There is an improvement in the agreement with the experiments.

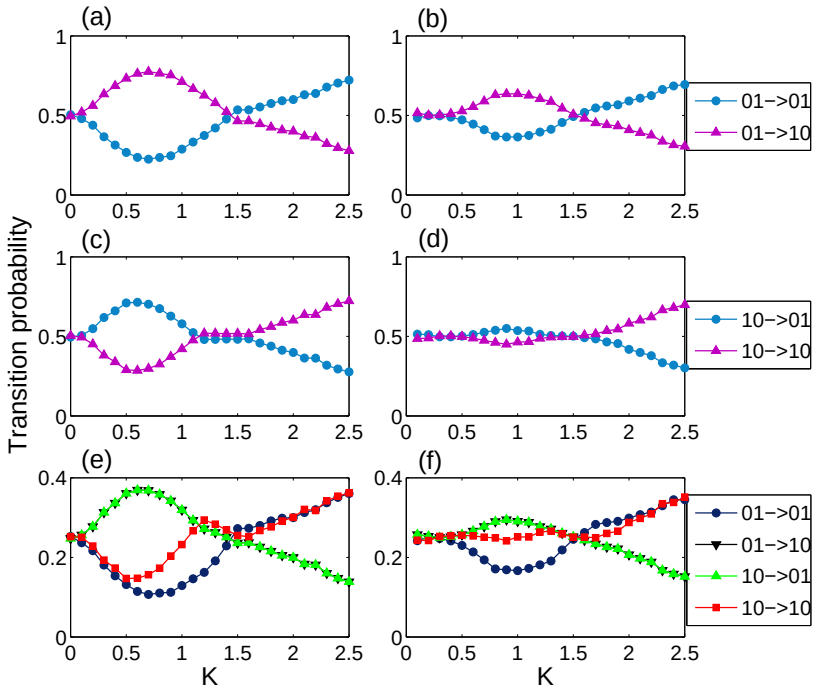

Figure 6.8: Influence of periodic forcing in the transition probabilities computed from the modified circle map, when varying the parameter K. (a,c,e) Transition probabilities with a constant noise strength ($\beta_c\xi$). (b,d,f), transition probabilities computed with the modified circle map considering the additional noise strength ($\beta_c(1+1/K)\xi$). The agreement with the experimental probabilities is further improved.

6.5 Summary

This chapter has presented an experimental and numerical study of the symbolic dynamics of a semiconductor laser with optical feedback and current modulation in the LFF regime. The ordinal symbolic analysis has allowed to identify clear changes in the dynamics induced by the modulation. For weak modulation the sequence of dropouts is found to be mainly stochastic, while for increasing modulation it becomes more deterministic, with correlations among several consecutive dropouts. Furthermore, the analysis of the transition probabilities has gone a step beyond in the time scale, showing correlations among five consecutive dropout events. Surprisingly, the clusters of words found in the previous chapter remain even in the presence of the external forcing.

The LK model, and the modified circle map model, have also been tested, and a good qualitative agreement with the experimental observations has been found. This reinforces the suitability of the LK model to describe the LFF dynamics.

In the case of the circle map it has been observed the convenience of considering an additional noise term, related to the modulation, to improve the agreement with the experiments.

Due to the suitability of the circle map to describe correlations in the spike activity of sensory neurons of paddlefish [48], the optical setup could be used to analyze the role of external forcing in the spike sequence, providing, for example, new insight in the role of gamma oscillations in the brain, which have been shown to serve to concentrate neuronal discharges to particular phases of the gamma cycle [149].

Chapter 7

Subwavelength position sensing using a semiconductor laser with two external cavities

Misura ciò che è misurabile e rendi misurabile ciò che non è misurabile.
Galileo Galilei

7.1 Introduction

Previous chapters have drawn upon the nonlinear dynamics of a semiconductor laser to unveil correlations and structured patterns in its behavior. This chapter presents a novel experimental method that exploits the sensitivity of a semiconductor laser to optical feedback, to perform subwavelength measurements by tracking induced changes in the frequencies of the dynamics. It is demonstrated how to harness quasi-periodic dynamics in a semiconductor laser with optical feedback from two independent external cavities, for measuring subwavelength changes in each arm of the cavity simultaneously.

The extreme sensitivity of semiconductor lasers with optical feedback has been widely studied for applications to sensors [52]. For example, in a semiconductor laser with one external cavity, displacements and vibrations of the external cavity can be

detected with subwavelength resolution, by tracking changes in the laser intensity, leading to the development of laser-feedback interferometry, also referred as self-mixing interferometry [6, 63, 150]. Also, the effect of the feedback in the relaxation oscillations has been used as imaging technique [151]. These techniques lead to the extraction of a single observable, restricting sensing or imaging to one dimension (1D). As a consequence, to image or sense objects in two or three dimensions, such laser-based systems require scanning and sequential 1D acquisitions.

In 2011, Cohen et al. [152] demonstrated a subwavelength 2D position sensor, using a high-speed nonlinear feedback system, in a radio-frequency wave-chaotic cavity. They showed that the position of an object, moving inside the 2D cavity, can be tracked without requiring sequential scanning to deduce 2D information. By measuring the frequency shifts induced in the quasi-periodic dynamics they associated a linear map between the two frequency shifts and the object position.

This chapter raises the question of whether the method can be extrapolated to the optical domain by using a laser diode. It is demonstrated that, by using quasi-periodic (QP) dynamics induced by two independent optical feedbacks (a two-armed cavity), independent fequency shifts can be obtained by independently displacing both mirrors. A mapping between the frequency shifts with subwavelength translations of each arm is unveiled, leading to a detection scheme for 2D nanoscale translations.

This *Chapter* presents the work performed in the laboratory of professor Daniel J. Gauthier, at Duke University (North Carolina, USA) in collaboration with Seth D. Cohen. These results have been sumarized in [153].

7.2 Experimental setup

Figure 7.1 displays the experimental setup. A single-mode semiconductor laser (LD, Sumitomo SLT4416-DP) operating at a wavelength of 1550.8 nm is submitted to dual optical feedback by means of two external cavities of lengths L_1 and L_2 respectively. The delay times from each external cavity is $\tau_1 = 55.5$ ns, and $\tau_2 = 55.6$ ns, with equal feedback strengths. The feedback reduction is of $\sim 1\%$. The pump current of the laser is $I = 23.6$ mA, with a current threshold of $I = 8.0$ mA (thus, $\approx 3I_{th}$).

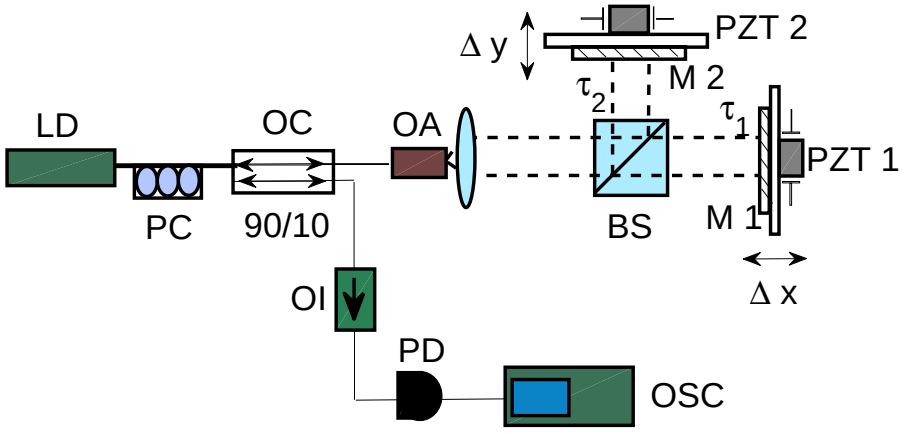

Figure 7.1: Schematic representation of the experimental setup. LD stands for laser diode, PC for polarization controller, OC for optical fiber coupler (90/10), OA for optical attenuator, BS for beamsplitter, M for mirror, PZT for piezoelectric transducer, OI for optical isolator, PD for photodetector, and OSC for oscilloscope.

The feedback strength is controlled via an optical attenuator (OA) placed before the beam splitter (see Fig. 7.1).

The laser is coupled to an optical fiber, and an optical coupler (OC) splits the ligth into two paths, one going to the detector and the other to the feedback cavities. As the optical fiber can modify the polarization of light as it travels through it, a polarization controller (PC) is used to ensure coherente feedback, i.e., the polarization of the return light is the same as the polarization of the emitted light. Figure 7.2(a) shows the output intensity vs. pump current curve for the laser with and without feedback (green and blue, respectively): the two slopes being parallel ensures coherent feedback [5].

In order to vary the lengths of the two external cavities, light goes out of the optical fiber and is sent through free space to two mirrors, via a 50/50 beam splitter (BS). Both mirrors are placed on piezoelectric transducers (PZT, Burleigh PZO-015) that translate the mirrors (M) and change the feedback delay time (τ_1 and τ_2).

In the detection path, to avoid reflections to the laser, an optical isolator (OI) is used before the detection is performed, using an ac-coupled 12 GHz photodetector (PD, New Focus 1544-B) and a 40 GS/s, 8 GHz analog bandwidth, high-speed digital oscilloscope (OSC, Agilent DSO90804A).

All the protocol, i.e., PZTs movements and data acquisition is computer controlled.

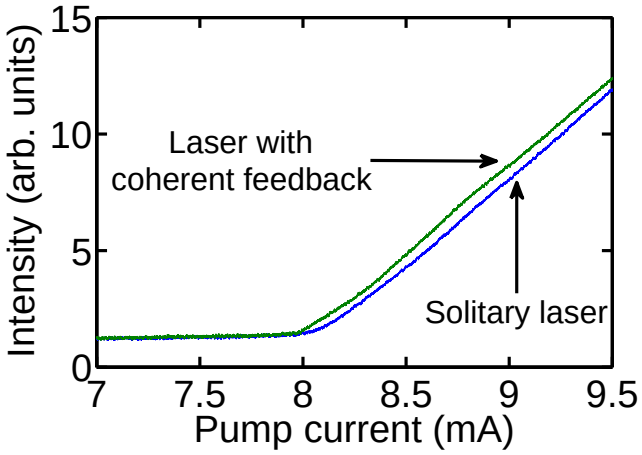

Figure 7.2: Output intensity of the solitary laser (blue), and of the laser with feedback (green). Both slopes are equal, indicating coherent feedback. The laser was a Sumitomo SLT4416-DP operating at 1550.8 nm.

The positions of the mirrors were moved on a nanoscale ($\Delta x << L_1$, and $\Delta y << L_2$), and the PZTs were calibrated in order to estimate their displacements in function of the applied voltage. This calibration was performed via a Michelson interferometer. By moving one of the PZTs, the intensity of the interference varies and, knowing the wavelength of the signal ($\lambda = 1550.8$ nm), it can be inferred the relation between the applied voltage and the displacement of the PZT. This calibration process is repeated for PZT_1 and PZT_2. The conversions obtained are, respectively, 29.2 ± 0.1 nm/V for PZT_1, and 45.8 ± 0.2 nm/V for PZT_2.

This calibration does not include either the hysteresis or the nonlinear response of the PZTs under applied voltages. To reduce the effects of the PZT nonlinearity and hysteresis, they are biased at 50 V (out of a total range of 0-150 V), taking into account the manufacturer's specifications, and the scans are performed by at most 3 V about this value. Deviation from linearity is at most 0.3%.

The 2D scan is then performed by varying the two PZTs in steps of ~ 10 nm, performing an 81 points 2D grid, covering approximately 100 nm $\times$ 100 nm.

7.3 Results

7.3.1 Quasi periodic dynamics

The dynamics that a semiconductor laser with optical feedback can manifest are broad, and among them it is quasi-periodicity (QP). QP dynamics is characterized by having two, or a few, incommensurate frequencies.

To achive this dynamical regime in the experimental setup, the feedback strength has to be fine tuned. This occurs for low feedback strengths ($\sim$ 1% of threshold reduction [36, 39]). Figure 7.3 displays the experimental quasi-periodic dynamics generated by the semiconductor laser with dual optical feedback. Panel (a) shows the signal acquired by the oscilloscope. It is a fast oscillatory signal with a slow modulation in its amplitude.

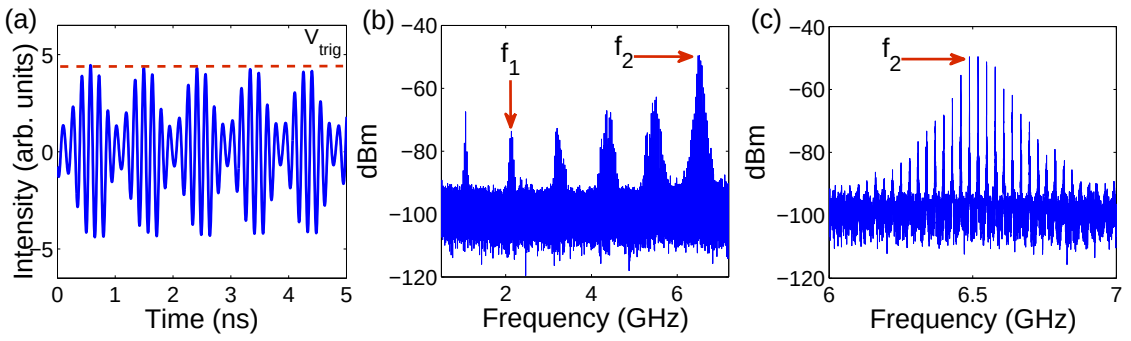

Figure 7.3: (a) Time trace intensity of the laser, averaged 500 times. The dotted line indicates the trigger (V_{trig}) used to do the acquisition (see *Section 7.3*). (b) Power spectral density of the signal in the quasi-periodic regime, showing six frequency clusters. Two of them labelled as $f_1 = 2.13$ GHz and $f_2 = 6.49$ GHz. These two clusters are used for subwavelength sensing. (c) Zoom on the structure of the second labelled frequency cluster.

Panel (b) shows the power spectral density of the signal in the quasi-periodic regime. It reveals multiple clusters of frequency peaks ranging from $\sim$ 1 GHz to $\sim$ 7 GHz (additional clusters above 8 GHz may be present but are not visible without s faster measurement equipment). The highest frequency cluster concentrates the largest amount of spectral power because it lies in the vicinity of the relaxation-oscillation frequency (measured to be $\sim$ 6.5 GHz for pumping current of $I = 23.6$

mA). The central frequencies of two of the clusters are labelled as $f_1 = 2.13$ GHz and $f_2 = 6.49$ GHz. These frequencies are incommensurate, and approximately linearly independent, for Δx and Δy in the range of the experiments. Due to this, they are the frequencies used to perform subwavelength position sensing. Panel (c) shows a zoom of the structure of the second labelled frequency cluster.

7.3.2 Detection of subwavelength displacements

If the frequencies of the QP dynamics are sensitive enough to nanometric variations of the lengths of the two arms, then a study of the frequencies can allow for subwavelength position sensing. Therefore, both mirrors are moved and their displacements tracked by following the relative frequency shifts (Δf_1 and Δf_2) due to subwavelength translations of the mirrors ($\Delta x, \Delta y << \lambda$). These translations imply changes in the time delays ($\Delta\tau_{1,2} = 2\Delta L_{1,2}/c$, where c is the speed of light in free space).

As mentioned before, the piezoelectric transducers are translated by steps of ~ 10 nm, within an approximative 100 nm $\times$ 100 nm 2D grid. The QP frequencies are tracked as the positions of the mirrors are changed. It is important that, over the subwavelength region of interest, the dynamics remains quasi-periodic. Over substantially larger regions, the QP dynamics was observed to undergo abrupt frequency jumps, thus limiting the range of applicability of the method. At each point of the grid, the frequency shifts ($\Delta f_{1,2}$) are measured.

The nanoscale modifications to the lengths of the cavities, induced by the PZTs, lead to observed frequency shifts on the kHz scale. This is considerably smaller than the actual frequencies (on the GHz scale). To discern such fine variations, a *trigger skew* on the oscilloscope was used. This way the oscilloscope waits a certain time between its initial triggering and the acquisition of the waveform ($t_{skew} = 5\mu s$). By using a large enough trigger skew, small frequency shifts (Δf) can be observed in the oscilloscope as phase shifts, $\Delta\varphi = \Delta f \cdot t_{skew}$.

This experimental approach improves the resolution of the frequency shifts up to the limit imposed by the jitter of the waveform. This effect of the jitter is reduced by averaging 500 time series, in real time, for each point of the 2D grid. This method is found to be a good compromise between jitter noise reduction and the inevitable drift in the apparatus due to temperature fluctuations.

In order to successfully average over the waveforms, the trigger height (V_{trig}) must also be tuned so that the oscilloscope triggers only on the maxima of the largest amplitudes, corresponding to regions of the quasi-periodic signal for which the incommensurate frequencies add constructively (see Fig. 7.3(a)). Other triggering values cause the averaged waveforms to collapse to zero, due to the non-periodic nature of the quasi-periodic signal. To know the frequency resolution of the experimental protocol, a quasi-periodic waveform generated by a stable wave-function generator (Agilent E8267D, with a frequency resolution of 10^{-3} Hz) is used, yielding a 3 kHz frequency resolution.

Once the two mirrors are displaced to cover the 2D grid (Δx, Δy), and the waveforms are acquired, they are fitted by a least-squares regression to the following four-frequency nonlinear function:

$$V(t) = \sum_{i=1}^{i=4} A_i \sin\left[2\pi(f_i + \Delta f_i)(t - t_{skew})\right] \tag{7.1}$$

where A_i and Δf_i are parameters determined via the regression, and f_i are directly measured with the oscilloscope. In order to achieve high resolution in determining the frequencies, one long waveform (5.25×10^5 points) is acquired before performing the 2D scan. A Fourier transform of this long waveform gives the four frequencies required for the regression.

To perform the subwavelength position sensing, the QP frequency shifts are monitored as a function of Δx and Δy.

Figure 7.4 shows the maps of Δf_1 (a), and Δf_2 (b) vs. Δx and Δy. The frequency shifts are mapped onto two smooth manifolds. Both manifolds exhibit different ranges of variation and levels of curvature, suggesting independent frequency shifts as a function of the position displacements. This independent behavior indicates that the functions are invertible. To demonstrate the independence and inversion, it is proposed to fit the nonlinear map by:

$$\Delta f_1(\Delta x, \Delta y) = \sum_{i=1}^{i=2} \left(a_i \Delta x^i + b_i \Delta y^i\right) + A\Delta x \Delta y + B \tag{7.2}$$

$$\Delta f_2(\Delta x, \Delta y) = \sum_{i=1}^{i=2} \left(c_i \Delta x^i + d_i \Delta y^i\right) + C\Delta x \Delta y + D \tag{7.3}$$

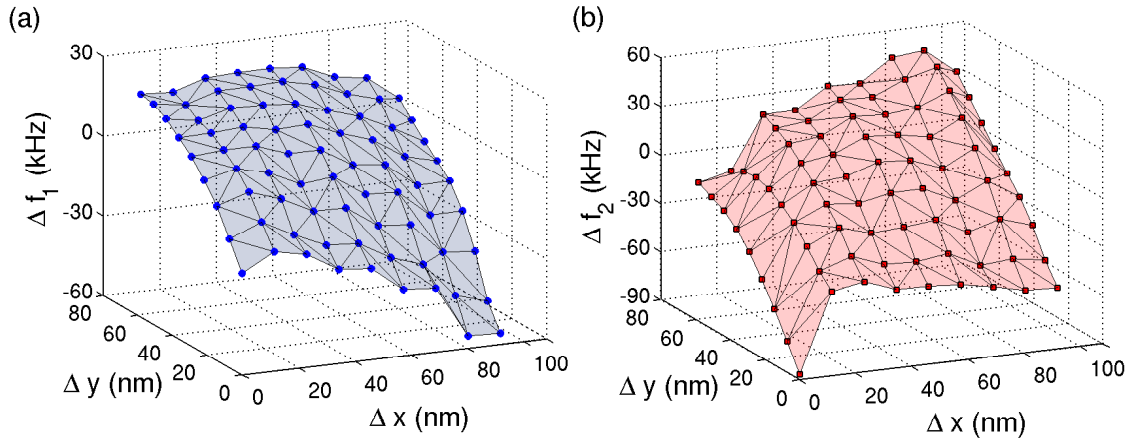

Figure 7.4: Experimental manifold associated with the quasi-periodic frequency shifts for Δf_1 (a), and Δf_2 (b), as a function of Δx and Δy. The 2D manifolds are fitted with the quadratic functions 7.2 and 7.3.

The fit gives:

$$\Delta f_1(\Delta x, \Delta y) = -17 - 0.07\Delta y + 1.25\Delta x + 0.0058\Delta x\Delta y - 0.0041(\Delta y)^2 - 0.0095(\Delta x)^2$$
$$\Delta f_2(\Delta x, \Delta y) = -68 + 1.2\Delta y + 1.9\Delta x + 0.009\Delta x\Delta y - 0.013(\Delta y)^2 - 0.014(\Delta x)^2$$

where Δf_i are measured in kHz, and Δx and Δy are measured in nm. As equations 7.2 and 7.3 are numerically invertible, specific values of Δx and Δy can be related to a given measure of the frequency shifts, Δf_1, and Δf_2, and vice versa. Thus, two specific frequency shifts give a specific set of measures of displacements in both arms, whereupon it can be used for position sensing.

Figure 7.5(a) shows the original grid and the predicted grid, by using the experimental protocol. The blue dots correspond to the 9×9 points where the QP dynamics is acquired to calibrate the protocol. The green line is the corresponding prediction of the fit.

Once the calibration is done, the protocol is tested by moving the two mirrors following an s-shape trajectory of 32 points (see Fig. 7.5(b)). The two PZTs are moved following the blue dots trajectory shown in the figure, and the green line is the trajectory recovered from the experimental protocol. As a guide, the calibration grid is depicted in black.

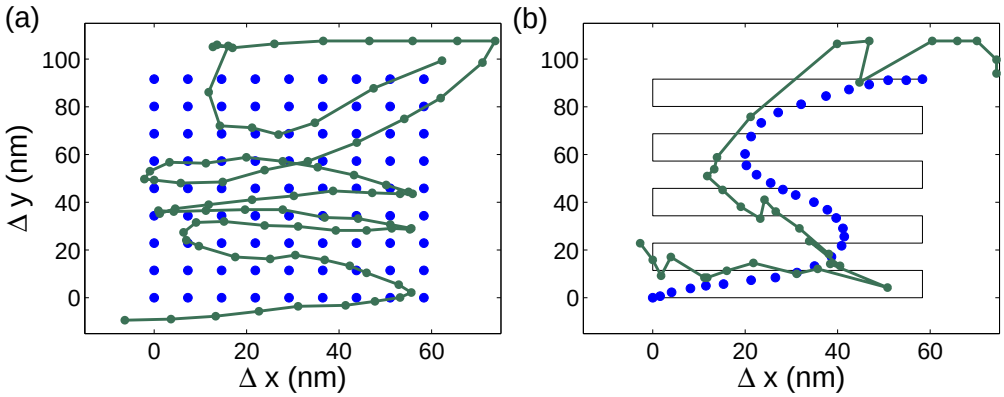

Figure 7.5: (a) Calibration grid formed by 81 points (blue dots), and the corresponding prediction of the experimental protocol (green line). (b) Arbitrary s-shaped trajectory (blue dots) and its corresponding prediction of the experimental protocol (green line)

To complete the measurements, i.e., the 81 calibration points followed by the 32 trajectory points, the experimental measures required almost 5 minutes. Just as in the calibration grid, this reconstructed path does not lie exactly on the actual path followed by the mirrors, although it preserves the S shape. This is expected, as the calibration grid is already distorted and this affects the prediction power. Aside, the protocol assumes a second order map, $\Delta f_{1,2} \rightarrow \Delta x, \Delta y$, while a higher order fit could improve the protocol.

The root-mean-square differences between the predicted and actual subwavelength translations realized by PZT_x and PZT_y are 12.3 nm and 6.8 nm, respectively. This gives an average resolution of 9.6 nm ($\sim \lambda/160$). The maximum errors between the experimental map and the fit are $\epsilon_{x,max} = 27.5$ nm ($\sim \lambda/60$), and $\epsilon_{y,max} = 22.7$ nm ($\sim \lambda/70$). This sets a limit on the achievable resolution of the device. Of course, other pairs of frequencies than f_1 and f_2 can be used to perform the position sensing, but from the experimental data acquired, these are the ones that provide the best 2D resolution.

It is thought that the main sources of errors in the measurements are room temperature fluctuations, which are not controlled. They induce erratic changes of the path lengths of each arm in the cavity, thus affecting the frequencies f_i with parasitic frequency shifts. Due to this fluctuations, the manifolds displayed in Fig.

7.4 can only be used once as calibration measurements to then infer an unknown subwavelength trajectory on the 100 nm × 100 nm grid. Beyond the 5 minutes time window, temperature fluctuations prevent from inferring subwavelength positions from the original calibrations, and a new calibration has to be performed. Also, as mentioned before, the approximation of the calibration grid as a second order surface introduces errors in the resolution of the calibration and the predicted positions.

7.4 Summary

In this chapter, an experimental protocol for a 2D position sensor with a resolution in the nanometer scale has been presented. The protocol uses a semiconductor laser with dual feedback, in the quasi-periodic dynamics regime. The sensitivity of the complex dynamics of semiconductor lasers to feedback has been exploited, to track subwavelength displacements of the mirrors of the external cavities. This is the first experimental study of a dual optical feedback for subwavelength multidimensional position sensing based on frequency shifts in the quasi-periodic dynamics spectrum.

This work has been a proof of concept demonstration, extending to the optical domain the work fo Cohen et al. [152], and applications to other systems can be expected.

Chapter 8

Summary of results and future work

Somewhere, something incredible is waiting to be known.
Carl Sagan

8.1 Summary of results

The main goal of the work presented in this *Thesis* has been to study the nonlinear dynamics of semiconductor lasers, in order to improve our understanding of nonlinear stochastic complex systems, and to exploit their dynamics for practical purposes.

The second part of the *Thesis* (*Chapters* 4 to 8) presents the results of the work.

Chapters 4, 5 and *6* have been devoted to the study of the LFF regime. In spite of the fact that the LFF regime is well known due to the great deal of attention that it has attracted over the last three decades, the work performed here has been able to unveil new features of the LFF dynamics: a novel analysis method for identifying signatures of determinism has been demonstrated; the presence of serial correlations, previously unkown, has been uncovered; and a minimal model to describe the statistics of the symbolic patterns has been found. This minimal model had been previously used to describe correlations among neuronal spikes, therefore suggesting

that semiconductor lasers in the LFF regime could be used for mimicking neuronal activity.

In *Chapter 4* a novel method of analysis has been introduced, which allows to distinguish statistical signatures of stochasticity and determinism from the sequence of dropouts in the LFF regime. The method, which uses ordinal symbolic analysis, is based on the choice of a threshold to classify the IDIs into short intervals (SIs) and long intervals (LIs), and suggests different mechanisms triggering the dropouts: one (LIs) compatible with a stochastic process, like escapes from a fixed point due to noise; and the other (SIs) with clear signs of determinism, that could be due to a stochastic trajectory on an underlying attractor in its return to the resting state. Therefore, the method allows statistically to infer which dropouts could be noise induced, and which ones could have a deterministic origin.

Furthermore, in *Chapter 5* ordinal symbolic analysis has shown that serial correlations are present in the sequence of intensity dropouts in the LFF regime. These correlations have a hierarchical and clustered organization of patterns which had not been previously noticed.

In *Chapter 6* the symbolic ordinal analysis has also enabled to identify clear changes in the LFF dynamics induced by modulation of the laser pump current. As the pump current is varied from un-modulated to high modulation amplitude, a transition from a stochastic-like behavior to a deterministic-like has been identified. In addition, the same clusters found in the un-modulated experiments have been found in the modulated ones, despite the external forcing.

A minimal model (modified circle map) has also been found, that describes the hierarachical and clustered symbolic structure seen in the experimental data.

Simulations of the LK model have been found to be in good qualitative agreement with the experimental observations, representing a validation of the model in unpredecent long time-scales.

In *Chapter 7* a novel method for 2D subwavelength position sensing in the infrared domain ($\lambda = 1550$ nm) was demonstrated. The method exploits the quasi-periodic dynamics of a semiconductor laser with two external cavities to resolve two independent displacements. By analyzing frequency shifts in the multifrequency spectrum of the laser intensity, a resolution in the nanometer scale has been demonstrated

($\lambda/160$). In this way two independent displacements can be identified by only acquiring the output intensity of the laser, without the need of a 2D scanning.

8.2 Perspectives for future work

This *Thesis* has improved our understanding of the nonlinear dynamics of semiconductor lasers with optical feedback, and leaves open questions that can be a logical continuation of the research presented here.

• It has been demonstrated the robustness of the words probabilities to variations of the threshold to detect the dropouts. However, for high values of the detection thresholds, close to the recovery of the dropout, where small intensity fluctuations appear to be stochastic, also signatures of determinism have been detected, which require more research in order to understand them properly.

• The method to distinguish signatures of determinism and stochasticity, which is computationally simple and has proven to be robust to threshold variations, could be used in a wide variety of real-world systems that present a spiking dynamics where signatures of deterministic underlying dynamics can be obscured by the presence of noise, such as neuronal inter-spike intervals, sequences of earthquakes, inter-event times in social networks, or intervals between sharp changes in the luminosity of variable stars.

• It would be interesting to consider the phenomenological model proposed by Mindlin and coworkers [84], which gives a good description of the probability distribution function of the inter-dropout intervals. In the symbolic dynamics of this model the most probable words are '012' and '210' [130], and it would be interesting to explore the parameter space to search for the two clusters of words uncovered here.

• In the analysis developed for the laser with external forcing, only the influence of the modulation amplitud has been studied. It is of interest to analyze the influence of varying the modulation frequency and the noise strength in the LFF dynamics and in the dropout correlations, specially having in mind phenomena such as stochastic or ghost resonance.

• All through this *Thesis*, the research has been focussed in the perturbations

induced by external optical feedback on a semiconductor laser (with and without pump current modulation). An interesting continuation of this research is to investigate the effect on the symbolic dynamics induced by optical injection from a second laser (uni-directional and bi-directional coupling). This could help to characterize synchronization states. This investigation and the effect of the modulation frequency in the symbolic dynamics is being carried out by Taciano Sorrentino and Carlos. A. Quintero.

• The suitability of the circle map, to describe the symbolic dynamics of the semiconductor laser under pump current modulation, revealed the need to include an additional noise term related to the modulation amplitude for a better agreement with the experiments. It would be interesting to analyze the LK model considering this additional noise term.

• The circle map minimal model has shown its suitability to describe the symbolic dynamics of the LFFs, but there is no explanation of why this is a good minimal moedl. This is an important open question that requires further studies.

• As the circle map had been previously proposed as minimal model of electroreceptors in paddlefish, these findings suggest that optical neurons, inspired in biological ones, displaying similar temporal correlations in their firing patterns, could be built using semiconductor lasers, thus providing a novel, inexpensive and controllable experimental set up for mimicking neuronal activity. In particular, it would be interestnig to explore the similarities between the symbolic dynamics of optical spikes and those from real neurons.

• The subwavelength position sensing protocol is a continuation of previous works in the radio-frequency domain in a chaotic cavity [152], and were followed by other experiments by Seth D. Cohen in an alectronic circuit [154]. Based on the results it would be expected that this method could be extended to other systems, as coupling the optical system to a wave-chaotic cavity [155], such that it interacts with a contained subwavelength scatterer. This system could also be modified to monitor chemical concentrations or nanoparticles in a solution [156, 157].

• From the theoretical point of view, there is still lack of an explanation for the frequency shifts in the QP regime. It would be of interest to analyze in depth the relation of the different independent frequencies with the nanometer displacements.

In this direction, it would be very helpful to perfom simulations with the LK model to identify the model parameters requiered for robust QP dynamics that allow to do 2D position sensing.

Bibliography

[1] T. H. Maiman, "Stimulated optical radiation in Ruby," *Nature*, vol. 187, pp. 493–494, 1960.

[2] T. H. Maiman, "Optical and microwave-optical experiments in Ruby," *Phys. Rev. Lett.*, vol. 4, pp. 564–566, 1960.

[3] A. E. Siegman, *Lasers*. University Science Books, 1986.

[4] C. O. Weiss and R. Vilaseca, *Dynamics of lasers*. VCH Weinheim, 1991.

[5] J. Ohtsubo, *Semiconductor Lasers: Stability, Instability and Chaos*. Springer, 2006.

[6] D. M. Kane and K. A. Shore, *Unlocking dynamical diversity. Optical feedback effects on semiconductor lasers*. Wiley, 2005.

[7] K. Lüdge, *Nonlinear laser dynamics: from quantum dots to cryptography*. Wiley-VCH, 2010.

[8] M. C. Soriano, J. García-Ojalvo, and I. F. C. R. Mirasso, "Complex photonics: Dynamics and applications of delay-coupled semiconductors lasers," *Rev. Mod. Phys.*, vol. 85, p. 421, 2013.

[9] M. Mitchell, *Complexity: a guided tour*. Oxford University press, 2009.

[10] A. A. Cecen and C. Erkal, "Distinguishing between stochastic and deterministic behavior in high frequency foreign exchange rate returns: Can non-linear dynamics help forecasting?," *Int. Jour. Forecast.*, vol. 12, pp. 465 – 473, 1996.

[11] J. A. Holyst, M. Zebrowska1, and K. Urbanowicz, "Observations of deterministic chaos in financial time series by recurrence plots, can one control chaotic economy?," *Eur. Phys J. B*, vol. 20, pp. 531 – 535, 2001.

[12] M. W. Slutzky, P. Cvitanovic, and D. J. Mogul, "Identification of determinism in noisy neuronal systems," *Jour. Neuro. Meth.*, vol. 118, pp. 153 – 161, 2002.

[13] P. Huybers and C. Wunsch, "Obliquity pacing of the late pleistocene glacial terminations," *Nature*, vol. 434, p. 491, 2005.

[14] O. A. Rosso, H. A. Larrondo, M. T. Martin, A. Plastino, and M. A. Fuentes, "Distinguishing noise from chaos," *Phys. Rev. Lett.*, vol. 99, p. 154102, 2007.

[15] B. Luque, L. Lacasa, F. Ballesteros, and J. Luque, "Observations of deterministic chaos in financial time series by recurrence plots, can one control chaotic economy?," *Phys. Rev. E*, vol. 80, p. 046103, 2009.

[16] J. Tiana-Alsina, J. M. Buldú, M. C. Torrent, and J. García-Ojalvo, "Quantifying stochasticity in the dynamics of delay-coupled semiconductor lasers via forbidden patterns," *Phil. Trans. Royal Soc.*, vol. 368, pp. 367 – 377, 2010.

[17] J. P. Crutchfield, "Between order and chaos," *Nature Phys.*, vol. 8, pp. 17 – 24, 2012.

[18] M. C. Soriano, L. Zunino, L. Larger, I. Fischer, and C. R. Mirasso, "Distinguishing fingerprints of hyperchaotic and stochastic dynamics in optical chaos from a delayed opto-electronic oscillator," *Opt. Lett.*, vol. 36, pp. 2212 – 2214, 2011.

[19] K. Hicke, X. Porte, and I. Fischer, "Characterizing the deterministic nature of individual power dropouts in semiconductor lasers subject to delayed feedback," *Phys. Rev. E*, vol. 88, p. 052904, 2013.

[20] C. Risch, C. Voumard, F. K. Reinhart, and R. Salathe, "External-cavity-induced nonlinearities in the light versus current characteristic of (Ga,AI) as continuous-wave diode lasers," *IEEE J. Quantum Electron.*, vol. 13, pp. 692 – 697, 1977.

[21] C. H. Henry, "Theory of the linewidth of SLC," *IEEE J. Quantum Electron.*, vol. 18, p. 259, 1982.

[22] T. Sano, "Antimode dynamics and chaotic itinerancy in the coherence collapse of semiconductor laser with feedback," *Phys. Rev. A*, vol. 50, pp. 2719 –2726, 1994.

[23] A. Hohl, H. J. C. van der Linden, and R. Roy, "Determinism and stochasticity of power-dropout events in semiconductor lasers with optical feedback," *Opt. Lett.*, vol. 20, pp. 2396 – 2398, 1995.

[24] I. Fischer, G. H. M. van Tartwijk, A. M. Levine, W. Elsässer, E. Göbel, and D. Lenstra, "Fast pulsing and chaotic itinerancy with a drift in the coherence collapse of semiconductor lasers," *Phys. Rev. Lett.*, vol. 76, pp. 220 – 223, 1996.

[25] M. Giudici, C. Green, G. Giacomelli, U. Nespolo, and J. R. Tredicce, "Andronov bifurcation and excitability in semiconductor lasers with optical feedback," *Phys. Rev. E*, vol. 55, p. 6414, 1997.

[26] G. Huyet, S. Hegarty, M. Giudici, D. de Bruyn, and J. G. McInerney, "Statistical properties of the dynamics of semiconductor lasers with optical feedback," *Europhys. Lett.*, vol. 40, pp. 619 – 624, 1997.

[27] T. Heil, I. Fischer, W. Elsässer, J. Mulet, and C. R. Mirasso, "Statistical properties of low-frequency fluctuations during single-mode operation in distributed-feedback lasers: experiments and modeling," *Opt. Lett.*, vol. 24, pp. 1275 – 1277, 1999.

[28] J. Mulet and C. R. Mirasso, "Numerical statistics of power dropouts based on the Lang-Kobayashi model," *Phys. Rev. E*, vol. 59, pp. 5400 – 5405, 1999.

[29] R. L. Davidchack, Y.-C. Lai, A. Gavrielides, and V. Kovanis, "Dynamical origin of low frequency fluctuations in external cavity semiconductor lasers," *Phys. Lett. A*, vol. 267, pp. 350 – 356, 2000.

[30] D. W. Sukow and D. J. Gauthier, "Entraining power-dropout events in an external-cavity semiconductor laser using weak modulation of the injection current," *IEEE J. Quantum Electron.*, vol. 36, pp. 175 – 183, 2000.

[31] W.-S. Lam, N. Parvez, and R. Roy, "Effect of spontaneous emission noise and modulation on semiconductor lasers near threshold with optical feedback," *Int. J. of Modern Phys. B*, vol. 17, pp. 4123 – 4138, 2003.

[32] J. M. Méndez, J. Aliaga, and G. B. Mindlin, "Limits on the excitable behavior of a semiconductor laser with optical feedback," *Phys. Rev. E*, vol. 71, p. 026231, 2005.

[33] Y. Hong and K. A. Shore, "Statistical measures of the power dropout ratio in semiconductor lasers subject to optical feedback," *Opt. Lett.*, vol. 30, pp. 3332 – 3334, 2005.

[34] A. Torcini, S. Barland, G. Giacomelli, and F. Marin, "Low-frequency fluctuations in vertical cavity lasers: Experiments versus Lang-Kobayashi dynamics," *Phys. Rev. A*, vol. 74, p. 063801, 2006.

[35] J. Zamora-Munt, C. Masoller, and J. García-Ojalvo, "Transient low-frequency fluctuations in semiconductor lasers with optical feedback," *Phys. Rev. A*, vol. 81, p. 033820, 2010.

[36] J. Mork, T. Tromborg, and J. Mark, "Chaos in semiconductor lasers with optical feedback: theory and experiment," *IEEE J. Quantum Electron.*, vol. 28, pp. 93 – 108, 1992.

[37] J. F. M. Ávila, H. L. D. de S. Cavalcante, and J. R. R. Leite, "Coarse grained variables and deterministic chaos in an excitable system," *Phys. Rev. Lett.*, vol. 17, p. 044101, 2008.

[38] J. Sacher, W. Elsässer, and O. Göbel, "Intermittency in the coherence collapse of a semiconductor laser with external feedback," *Phys. Rev. Lett.*, vol. 63, pp. 2224 – 2227, 1989.

[39] C. Masoller, "Coexistence of attractors in a laser diode with optical feedback from a large external cavity," *Phys. Rev. A*, vol. 50, pp. 2569 –2578, 1994.

[40] J. Ye, H. Li, and G. McInerney, "Period-doubling route to chaos in a semiconductor laser with weak optical feedback," *Phys. Rev. A*, vol. 47, pp. 22494 – 2252, 1993.

[41] A. Hohl and A. Gavrielides, "Bifurcation cascade in a semiconductor laser subject to optical feedback," *Phys. Rev. Lett.*, vol. 82, p. 1148, 1999.

[42] D. Brunner, M. C. Soriano, and I. F. C. R. Mirasso, "Parallel photonic information processing at gigabyte per second data rates using transient states," *Nature Comm.*, vol. 4, p. 1364, 2013.

[43] N. Oliver, M. C. Soriano, D. W. Sukow, and I. Fischer, "Fast random bit generation using a chaotic laser: Approaching the information theoretic limit," *IEEE J. Quantum Electron.*, vol. 49, pp. 910 – 918, 2013.

[44] L. Appeltant, G. V. der Sande, J. Danckaert, and I. Fischer, "Constructing optimized binary masks for reservoir computing with delay systems," *Sci. Rep.*, vol. 4, p. 3629, 2014.

[45] A. U. et al., "Fast physical random bit generation with chaotic semiconductor lasers," *Nat. Phot.*, vol. 2, pp. 728 – 732, 2008.

[46] I. Kanter, Y. Aviad, I. Reidler, E. Cohen, and M. Rosenbluh, "An optical ultrafast random bit generator," *Nat. Phot.*, vol. 4, pp. 58 – 61, 2009.

[47] A. Argyris, D. Syvridis, L. Larger, V. Annovazzi-Lodi, P. Colet, I. Fischer, J. García-Ojalvo, C. R. Mirasso, L. Pesquera, and A. Shore, "Chaos-based communications at high bit rates using commercial fibre-optic links," *Nature*, vol. 438, pp. 343 – 346, 2005.

[48] A. B. Neiman and D. F. Russell, "Models of stochastic biperiodic oscillations and extended serial correlations in electroreceptors of paddlefish," *Phys. Rev. E*, vol. 71, p. 061915, 2005.

[49] Y. Liu, N. Kikuchi, and J. Ohtsubo, "Controlling dynamical behavior of a semiconductor laser with external optical feedback," *Phys. Rev. E*, vol. 51, pp. R2697 – R2700, 1995.

[50] C. M. Ticos, I. R. Andrei, M. L. Pascu, and M. Bulinski, "Experimental control of power dropouts by current modulation in a semiconductor laser with optical feedback," *Physica Scripta*, vol. 83, p. 055402, 2011.

[51] J. L. A. Dubbeldam, B. Krauskopf, and D. Lenstra, "Excitability and coherence resonance in lasers with saturable absorber," *Phys. Rev. E*, vol. 60, p. 6580, 1999.

[52] S. Donati, "Developing self-mixing interferometry for instrumentation and measurements," *Lasers & Photonics Review*, vol. 6, p. 393, 2012.

[53] A. Einstein, "Zur quantentheorie der strahlung," *Physik. Zeitschs.*, vol. XVIII, pp. 121 – 128, 1917.

[54] J. Gordon, H. Zeiger, and C. Townes, "Molecular microwave oscillator and new hyperfine structure in the microwave spectrum of NH_3," *Phys. Rev*, vol. 95, pp. 282 – 284, 1954.

[55] R. N. Hall, G. F. Fenner, J. D. Kingsley, T. J. Soltys, and R. D. Carlson, "Coherent light emission from GaAs junctions," *Phys. Rev. Lett.*, vol. 9, p. 366, 1962.

[56] N. Holonyak and S. F. Bevacqua, "Coherent (visible) light emission from $Ga(As_{1-x}P_x)$ junctions," *Appl. Phys. Lett.*, vol. 1, p. 82, 1962.

[57] M. I. Nathan, W. P. Dumke, G. Burns, F. H. Hill, and G. A. Lasher, "Stimulated emission of radiationfrom GaAs p-n junctions," *Appl. Phys. Lett.*, vol. 1, p. 62, 1962.

[58] T. M. Quist, R. H. Rediker, R. J. Keyes, W. E. Krag, B. Lax, A. L. McWorther, and H. J. Zeiger, "Semiconductor maser of GaAs," *Appl. Phys. Lett.*, vol. 1, p. 91, 1962.

[59] M. C. Torrent and M. S. Miguel, "Stochastic-dynamics characterization of delayed laser threshold instability with swept control parameters," *Phys. Rev. A*, vol. 38, p. 245, 1988.

[60] J.-M. Liu, *Photonic devices*. Cambridge University Press, 2005.

[61] F. Rossi, P. Matteini, F. Ratto, L. Menabuoni, I. Lenzetti, and R. Pini, "Laser tissue welding in ophthalmic surgery," *J. Biophotonics*, vol. 4, pp. 331 – 342, 2008.

[62] Y.-P. Chang, F. Pinaud, J. Antelman, and S. Weiss, "Tracking bio-molecules in live cells using quantum dots," *J. Biophotonics*, vol. 4, pp. 287 – 298, 2008.

[63] U. Zabit, R. Atashkhooei, T. Bosch, S. Royo, F. Bony, and A. D. Rakic, "Adaptive self-mixing vibrometer based on a liquid lens," *Opt. Lett.*, vol. 35, pp. 1278 – 1280, 2010.

[64] T. Heil, I. Fischer, W. Elsässer, and A. Gavrielides, "Dynamics of semiconductor lasers subject to delayed optical feedback: The short cavity regime," *Phys. Rev. Lett.*, vol. 87, p. 243901, 2001.

[65] D. Lenstra, B. H. Verbeek, and A. J. den Boef, "Coherence collapse in single-mode semiconductor lasers due to optical feedback," *IEEE J. Quantum Electron.*, vol. 21, p. 674, 1985.

[66] T. Heil, I. Fischer, and W. Elsässer, "Influence of amplitude-phase coupling on the dynamics of semiconductor lasers subject to optical feedback," *Phys. Rev. A*, vol. 60, pp. 634 – 641, 1999.

[67] J. R. Terry, K. S. Thornburg, D. J. DeShazer, G. D. VanWiggeren, S. Zhu, P. Ashwin, and R. Roy, "Synchronization of chaos in an array of three lasers," *Phys. Rev. E*, vol. 59, pp. 4036 – 4043, 1999.

[68] J. M. Buldú, J. García-Ojalvo, C. R. Mirasso, M. C. Torrent, and J. M. Sancho, "Effect of external noise correlation in optical coherence resonance," *Phys. Rev. E*, vol. 64, p. 051109, 2001.

[69] J. M. Buldú, D. R. Chialvo, C. R. Mirasso, M. C. Torrent, and J. García-Ojalvo, "Ghost resonance in a semiconductor laser with optical feedback," *Europhys. Letts.*, vol. 64, p. 178, 2003.

[70] J. F. M. Ávila, H. L. D. de S. Cavalcante, and J. R. R. Leite, "Experimental deterministic coherence resonance," *Phys. Rev. Lett.*, vol. 93, p. 144101, 2004.

[71] C. M. González, J. M. Buldú, M. C. Torrent, and J. García-Ojalvo, "Processing distributed inputs in coupled excitable lasers," *Phys. Rev. A.*, vol. 76, p. 053824, 2007.

[72] R. Tkach and A. Chraplyvy, "Regimes of feedback effects in 1.5 μ m distributed feedback lasers," *J. Lightwave Technol.*, vol. LT-4, pp. 1655 – 1661, 1986.

[73] G. D. V. Wiggener and R. Roy, "Communication with chaotic lasers," *Science*, vol. 279, p. 1198, 1998.

[74] F.-Y. Lin and J.-M. Liu, "Communication with chaotic lasers," *IEEE J. Quantum Electr.*, vol. 40, p. 815, 2004.

[75] H. Jaeger and H. Haas, "Harnessing nonlinearity: Predicting chaotic systems and saving energy in wireless communication," *Science*, vol. 304, pp. 78 – 80, 2004.

[76] L. Appeltant, M. C. Soriano, G. van der Sande, J. Dankaert, S. Massar, J. Dambre, B. Schrauwen, C. R. Mirasso, and I. Fischer, "Information processing using a single dynamical node as complex system," *Nat. Comm.*, vol. 2, p. 468, 2011.

[77] L. Larger, M. C. Soriano, D. Brunner, L. Appeltant, J. M. Gutierrez, L. Pesquera, C. R. Mirasso, , and I. Fischer, "Photonic information processing beyond Turing: an optoelectronic implementation of reservoir computing," *Opt. Expr.*, vol. 20, pp. 3241 – 3249, 2012.

[78] N. Schunk and K. Petermann, "Stability analysis for laser diodes with short external cavities," *IEEE Photon. Technol. Lett.*, vol. 1, pp. 49 – 51, 1989.

[79] C. Masoller, "Effects of the external cavity length in the dynamics of a semiconductor laser with optical feedback," *Optics Comm.*, vol. 128, pp. 363 – 376, 1996.

[80] V. Ahlers, U. Parlitz, and W. Lauterborn, "Hyperchaotic dynamics and synchronization of external-cavity semiconductor lasers," *Phys. Lett. E*, vol. 58, p. 7208, 1998.

[81] J. Ohtsubo, "Chaotic dynamics in semiconductor lasers with optical feedback," *Progress in Optics.*, vol. 44, pp. 1 – 84, 2002.

[82] C. Masoller, "Spatiotemporal dynamics in the coherence collapsed regime of semiconductor lasers with optical feedback," *Chaos*, vol. 17, pp. 455 – 462, 1997.

[83] R. Lang and K. Kobayashi, "External optical feedback effects on semiconductor injection laser properties," *IEEE J. Quantum Electron.*, vol. 16, p. 347, 1980.

[84] A. M. Yacomotti, M. C. Eguia, J. Aliaga, O. E. Martínez, G. B. Mindlin, and A. Lispsich, "Interspike time distribution in noise driven excitable systems," *Phys. Rev. Lett.*, vol. 83, p. 292, 1999.

[85] A. Tabaka, M. Peil, M. Sciamanna, I. Fischer, W. Elsässer, H. Thienpont, I.Veretennicoff, and K. Panajotov, "Dynamics of vertical-cavity surface-emitting lasers in the short external cavity regime: Pulse packages and polarization mode competition," *Phys. Rev. A*, vol. 73, p. 013810, 2006.

[86] A. Takeda, R. Shogenji, and J. Ohtsubo, "Dynamics and pulse-package oscillations in broad-area semiconductor lasers with short optical feedback," *Appl. Phys. Lett.*, vol. 101, p. 231105, 2012.

[87] C. H. Henry and R. F. Kazarinov, "Instability of semiconductor lasers due to optical feedback from distant reflector," *IEEE J. Quantum Electron.*, vol. 2, pp. 294 – 301, 1982.

[88] J. Sacher, W. Elsässer, and O. Göbel, "Intermittency in coherence collapse of a semiconductor laser with external feedback," *Phys. Rev. Lett.*, vol. 63, pp. 2224 – 2227, 1989.

[89] H. Kantz and T. Schreiber, *Nonlinear time series analysis.* Cambridge University press, 2000.

[90] P. Grassberger and I. Procaccia, "Estimation of the Kolmogorov entropy from a chaotic signal," *Phys. Rev. A*, vol. 28, pp. 2591 – 2593, 1983.

[91] J. P. Eckmann and D. Ruelle, "Ergodic theory of chaos and strange attractors," *Rev. Mod. Phys.*, vol. 57, pp. 617 – 656, 1985.

[92] T. Sauer, "Reconstruction of the dynamical systems from interspike intervals," *Phys. Rev. Lett.*, vol. 72, pp. 3811 – 3814, 1994.

[93] L. Lacasa, B. Luque, F. Ballesteros, J. Luque, and J. C. Nuno, "From time series to complex networks: The visibility graph," *PNAS*, vol. 105, pp. 4972 – 4975, 2008.

[94] A. Kolmogorov *Dokl. Akad. Nauk. SSSR*, vol. 119, p. 861, 1958.

[95] Y. Sinaj *Dokl. Akad. Nauk. SSSR*, vol. 124, p. 768, 1959.

[96] P. Grassberger and I. Procaccia, "Measuring the strangeness of strange attractors," *Phys. D: Nonlinear Phenomena*, vol. 9, pp. 189 – 208, 1983.

[97] C. E. Shannon, "A mathematical theory of communiaction," *The Bell System Technical Journal*, vol. XXVII, pp. 379 – 423, 1948.

[98] H. Kantz and E. Olbrich, "Coarse grained dynamical entropies: Investigation of high-entropic dynamical systems," *Physica A*, vol. 280, pp. 34 – 48, 2000.

[99] C. S. Daw, C. E. A. Finney, and E. R. Tracy, "A review of symbolic analysis of experimental data," *Rev. Scientific Intr.*, vol. 74, pp. 915 – 930, 2003.

[100] S. H. Strogatz, *Nonlinear dynamics and chaos.* Westview Press, 1994.

[101] C. S. Daw, M. B. Kennel, C. E. A. Finney, and F. T. Connolly, "Observing and modeling nonlinear dynamics in an internal combustion engine," *Phys. Lett. E*, vol. 57, p. 2811, 1998.

[102] U. Schwarz, A. O. Benz, J. Kurths, and A. Witt, "Analysis of solar spike events by means of symbolic dynamics methods," *Astron. Astrophys.*, vol. 277, p. 215, 1993.

[103] C. Bandt and B. Pompe, "Permutation entropy: A natural complexity measure for time series," *Phys. Rev. Lett.*, vol. 88, p. 174102, 2002.

[104] J. Amigó, S. Zambrano, and M. Sanjuán, "True and false forbidden patterns in deterministic and random dynamics," *Europhys. Lett.*, vol. 79, p. 50001, 2007.

[105] J. M. Amigó, R. Monetti, T. Aschenbrenner, and W. Bunk

[106] L. Z. M. Zanin, and, O. A. Rosso, and D. Papo, "Permutation entropy and its main biomedical and econophysics applications: A review," *Entropy*, vol. 14, pp. 1553 – 1577, 2012.

[107] European Physics Journal: Special Topics, "Recent progress in symbolic dynamics and permutation complexity. Ten years of permutation entropy," vol. 222, june, 2013.

[108] J. M. Amigó, L. Kocarev, and J. Szczepanski, "Order patterns and chaos," *Phys. Lett. A*, vol. 355, pp. 27 – 31, 2006.

[109] L. C. Carpi, P. M. Saco, and O. A. Rosso, "Missing ordinal patterns in correlated noises," *Phys. A*, vol. 389, pp. 2020 – 2029, 2010.

[110] L. Zunino, M. C. Soriano, I. Fischer, O. A. Rosso, and C. R. Mirasso, "Permutation-information-theory approach to unveil delay dynamics from time-series analysis," *Phys. Rev. E*, vol. 82, 2010.

[111] M. Matilla-García and M. R. Marín, "A non-parametric independence test using permutation entropy," *J. Econom.*, vol. 144, pp. 139 – 155, 2008.

[112] S. J. Cánovas and a. M. C. R. A. Guillamón, "Using permutations to detect dependence between time series," *Phys. D*, vol. 240, pp. 1199 – 1204, 2011.

[113] I. Veisi, N. Pariz, and A. Karimpour, "Fast and robust detection of epilepsy in noisy EEG signals using permutation entropy," *Proceedings of the 7th IEEE International Conference on Bioinformatics and Bioengineering*, pp. 200 – 203, 2007.

[114] Y. Cao, W. Tung, and J. B. Gao, "Detecting dynamical changes in time series using the permutation entropy," *Phys. Rev. E*, vol. 70, p. 046217, 2004.

[115] X. Li, X. G. Ouyang, and D. A. Richards, "Predictability analysis of absence seizures with permutation entropy," *Proceedings of the 7th IEEE International Conference on Bioinformatics and Bioengineering*, vol. 77, 2007.

[116] G. Ouyang and D. A. R. X. Li, C. Dang, "Deterministic dynamics of neural activity during absence seizures in rats," *Phys. Rev. E*, vol. 79, p. 041146, 2009.

[117] S. Schinkel, N. Marwan, and J. Kurths, "Brain signal analysis based on recurrences," *J. Physiol.*, vol. 103, pp. 315 – 323, 2009.

[118] U. Parlitz, S. Berg, S. Luther, A. Schirdewan, J. Kurths, and N. Wessel, "Classifying cardiac biosignals using ordinal pattern statistics and symbolic dynamics," *Comput. Biol. Med.*, vol. 42, pp. 319 – 327, 2012.

[119] C. Bian, C. Qin, Q. D. Y. Ma, and Q. Shen, "Modied permutation-entropy analysis of heartbeat dynamics," *Phys. Rev. E*, vol. 85, 2012.

[120] B. Frank, B. Pompe, U. Schneider, and D. Hoyer, "Permutation entropy improves fetal behavioural state classification based on heart rate analysis from biomagnetic recordings in near term fetuses.," *Med. Biol. Eng. Comput.*, vol. 44, p. 013103, 2006.

[121] A. Bahraminasab, F. Ghasemi, A. Stefanovska, P. V. E. McClintock, and H. Kantz, "Direction of coupling from phases of interacting oscillators: A permutation information approach," *Phys. Rev. Lett.*, vol. 100, 2008.

[122] M. Zanin, "Forbidden patterns in financial time series," *Chaos*, vol. 18, 2008.

[123] L. Zunino, M. Zanin, B. M. Tabak, D. G. Pérez, and O. A. Rosso, "Forbidden patterns, permutation entropy and stock market inefficiency," *Phys. A*, vol. 388, 2009.

[124] L. Zunino, A. F. Bariviera, M. B. Guercio, L. B. Martínez, and O. A. Rosso, "On the efficiency of sovereign bond markets," *Phys. A*, vol. 391, pp. 4322 – 4349, 2012.

[125] V. Suyal, A. Prasad, and H. P. Singh, "Hysteresis in a solar activity cycle," *Solar Phys.*, vol. 276, pp. 407 – 414, 2012.

[126] P. M. Saco, L. C. Carpi, A. Figliola, E. Serrano, and O. A. Rosso, "Entropy analysis of the dynamics of El Niño Southern Oscillation during the Holocene," *Physica A*, vol. 389, pp. 5022 – 5027, 2010.

[127] J. Deza, M. Barreiro, and C. Masoller, "Inferring interdependencies in climate networks constructed at inter-annual, intra-season and longer time scales," *Eur. Phys. J. Special Topics*, vol. 222, pp. 511 – 523, 2013.

[128] J. Tiana-Alsina, M. C. Torrent, O. A. Rosso, C. Masoller, and J. García-Ojalvo, "Quantifying the statistical complexity of low-frequency fluctuations in semiconductor lasers with optical feedback," *Phys. Rev. A*, vol. 82, p. 013819, 2010.

[129] M. Martin, A. Plastino, and O. Rosso, "Generalized statistical complexity measures: Geometrical and analytical properties," *Physica A*, vol. 369, pp. 439 – 462, 2006.

[130] N. Rubido, J. Tiana-Alsina, M. C. Torrent, J. García-Ojalvo, and C. Masoller, "Language organization and temporal correlations in the spiking activity of an excitable laser: Experiments and model comparison," *Phys. Rev. E*, vol. 84, p. 026202, 2011.

[131] M. C. Soriano, L. Zunino, O. A. Rosso, I. Fischer, and C. R. Mirasso, "Time scales of a chaotic semiconductor laser with optical feedback under the lens

of a permutation information analysis," *IEEE J. Quantum Electron.*, vol. 47, pp. 252 – 261, 2011.

[132] L. Zunino, M. C. Soriano, and O. A. Rosso, "Characterizing the hyperchaotic dynamics of a semiconductor laser subject to optical feedback via permutation entropy," *IEEE J. Selected Topics in Quantum Electron.*, vol. 17, pp. 1250 – 1257, 2011.

[133] S. Y. Xiang, W. Pan, L. S. Yan, B. Luo, X. H. Zou, N. Jiang, and K. H. Wen, "Quantifying chaotic unpredictability of vertical-cavity surface-emitting lasers with polarized optical feedback via permutation entropy," *IEEE J. Quantum Electron.*, vol. 17, pp. 1212 – 1219, 2011.

[134] M. San-Miguel, Q. Feng, and J. V. Moloney, "Light polarization dynamics in surface-emitting semiconductor lasers," *Phys. Rev. A*, vol. 52, pp. 1728 – 1739, 1995.

[135] J. P. Toomey and D. M. Kane, "Mapping the dynamic complexity of a semiconductor laser with optical feedback using permutation entropy," *Opt. Express*, vol. 22, p. 1713, 2014.

[136] A. J. Archer and M. Rauscher, "Dynamical density functional theory for interacting brownian particles: stochastic or deterministic?," *J. Phys. A: Math. Gen.*, vol. 37, pp. 9325–9333, 2004.

[137] A. A. Tsonis and J. P. Elsner, "Nonlinear prediction as a way of distinguishing chaos from random fractal sequences," *Nature*, vol. 358, p. 217, 1992.

[138] U. Parlitz, S. Berg, S. Luther, A. Schirdewan, J. Kurths, and N. Wessel, "Classifying cardiac biosignals using ordinal pattern statistics and symbolic dynamics," *Comp. Biol. Med.*, vol. 42, pp. 319 – 327, 2012.

[139] A. Aragoneses, N. Rubido, J. Tiana-Alsina, M. C. Torrent, and C. Masoller, "Distinguishing signatures of determinism and stochasticity in spiking complex systems," *Sci. Rep.*, vol. 3, p. 1778, 2013.

[140] L. Glass, M. R. Guevara, J. Belair, and A. Shrier, "Global bifurcations of a periodically forced biological oscillator," *Phys. Rev. A*, vol. 29, pp. 1348 – 1357, 1984.

[141] A. Aragoneses, S. Perrone, T. Sorrentino, M. C. Torrent, and C. Masoller, "Unveiling the complex organization of recurrent patterns in spiking dynamical systems," *Sci. Rep.*, vol. 4, p. 4696, 2014.

[142] D. Baums, W. Elsässer, and E. O. Göbel, "Farey tree and Devil's staircase of a modulated external-cavity semiconductor laser," *Phys. Rev. Lett.*, vol. 63, p. 155, 1989.

[143] J. M. Méndez, R. Laje, M. Giudici, J. Aliaga, and G. B. Mindlin, "Dynamics of periodically forced semiconductor laser with optical feedback," *Phys. Rev. E*, vol. 63, p. 066218, 2001.

[144] J. P. Toomey, D. M. Kane, M. W. Lee, and K. A. Shore, "Nonlinear dynamics of semiconductor lasers with feedback and modulation," *Opt. Express*, vol. 18, pp. 16955 – 16972, 2010.

[145] F. Marino, M. Giudici, S. Barland, and S. Balle, "Experimental evidence of stochastic resonance in an excitable optical system," *Phys. Rev. Lett.*, vol. 88, p. 040601, 2002.

[146] J. M. Buldú, J. García-Ojalvo, C. R. Mirasso, and M. C. Torrent, "Stochastic entrainment of optical power dropouts," *Phys. Rev. E*, vol. 66, p. 021106, 2002.

[147] T. Schwalger, J. Tiana-Alsina, M. C. Torrent, J. Garcia-Ojalvo, and B. Lindner, "Interspike-interval correlations induced by two-state switching in an excitable system," *Europhys. Letts.*, vol. 99, p. 10004, 2012.

[148] A. Aragoneses, T. Sorrentino, S. Perrone, D. J. Gauthier, M. C. Torrent, and C. Masoller, "Experimental and numerical study of the symbolic dynamics of a modulated external-cavity semiconductor laser," *Opt. Express*, vol. 4, pp. 4705 – 4713, 2014.

[149] D. Nikolic, P. Fries, and W. Singer, "Gamma oscillations: precise temporal coordination without a metronome," *Trends in Cognitive Sciences*, vol. 17, p. 54, 2013.

[150] S. Donati, G. Giuliani, and S. Merlo, "Laser diode feedback interferometer for measurement of displacements without ambiguity," *IEEE J. Quantum Electron.*, vol. 31, pp. 113 – 119, 1995.

[151] E. Lacot, R. Day, J. Pinel, and F. Stoeckel, "Adaptive self-mixing vibrometer based on a liquid lens," *Opt. Lett.*, vol. 26, p. 1483, 2001.

[152] S. D. Cohen, H. D. S. L. Cavalcante, and D. J. Gauthier, "Subwavelength position sensing using nonlinear feedback and wave chaos," *Phys. Rev. Lett.*, vol. 107, p. 254103, 2011.

[153] S. D. Cohen, A. Aragoneses, D. Rontani, M. C. Torrent, C. Masoller, and D. J. Gauthier, "Multidimensional subwavelength position sensing using a semiconductor laser with optical feedback," *Opt. Lett.*, vol. 38, pp. 4331 – 4334, 2013.

[154] S. D. Cohen, *Subwavelength sensing using nonlinear feedback in a wave-chaotic cavity, Ph. D. thesis*. Duke University, 2013.

[155] T. Gensty, K. Becker, I. Fischer, W. Elsässer, C. Degen, P. Debernardi, and G. P. Bava, "Wave chaos in real-world vertical-cavity surface-emitting lasers," *Phys. Rev. Lett.*, vol. 94, p. 33901, 2005.

[156] B. E. DeMartini, J. F. Rhoads, M. A. Zielke, K. G. Owen, S. W. Shaw, and K. L. Turner, "A single input-single output coupled microresonator array for the detection and identification of multiple analytes," *Appl. Phys. Lett.*, vol. 93, p. 054102, 2008.

[157] H.-Y. Lin, C.-H. Huang, C.-C. Huang, Y.-C. Liu, and L.-K. Chau, "Multiple resonance fiber-optic sensor with time division multiplexing for multianalyte detection," *Opt. Lett.*, vol. 37, p. 3969, 2012.

List of publications related to this thesis

• Andrés Aragoneses, Nicolás Rubido, Jordi Tiana-Alsina, M. C. Torrent, and Cristina Masoller. *Distinguishing signatures of determinism and stochasticity in spiking complex systems*. Sci. Rep. **3**, 1778 (2013).

• Seth D. Cohen, Andrés Aragoneses, Damien Rontani, M. C. Torrent, Cristina Masoller, and Daniel J. Gauthier. *Multidimensional subwavelength position sensing using a semiconductor laser with optical feedback*. Opt. Lett. **38**, 4331 (2013).

• Andrés Aragoneses, Taciano Sorrentino, Sandro Perrone, Daniel J. Gauthier, M. C. Torrent, and Cristina Masoller. *Experimental and numerical study of the symbolic dynamics of a modulated external-cavity semiconductor laser*. Opt. Express. **22**, 4705 (2014).

• Andrés Aragoneses, Sandro Perrone, Taciano Sorrentino, M. C. Torrent, and Cristina Masoller. *Unveiling the complex organization of recurrent patterns in spiking dynamical systems*. Sci. Rep. **4**, 4696 (2014).

Presentations in conferences and workshops

• QUONLOP'11. *Experimental study of different LFF regimes in semiconductor lasers with an external cavity.* Andrés Aragoneses, Jordi Zamora-Munt, Pramod Kumar, M. C. Torrent, and Cristina Masoller. Valladolid, Spain, 10-11 February, 2011. [Poster contribution]

• IBERSINC'11. *Laboratorio de dinámica de láseres.* Jordi García-Ojalvo, M. C. Torrent, Cristina Masoller, Cristian Bonatto, Jordi Zamora-Munt, Jordi Tiana-Alsina, and Andrés Aragoneses. Barcelona, Spain, 17-18 March, 2011. [Poster contribution]

• Congreso de Física Estadística, FISES'11. *Laboratorio de dinámica de láseres.* Jordi García-Ojalvo, M. C. Torrent, Cristina Masoller, Cristian Bonatto, Jordi Zamora-Munt, Jordi Tiana-Alsina, and Andrés Aragoneses. Barcelona, Spain, 2-4 June, 2011. [Poster contribution]

• Deutsche Physikalische Gesellschaft. *Distinguishing determinism from stochasticity: ordinal analysis of the structure of the spiking activity of semiconductor lasers with optical feedback.* Andrés Aragoneses, Nicolás Rubido, Taciano Sorrentino, M. C. Torrent, and Cristina Masoller. Berlin, Germany, 25-30 March, 2012. [Poster

contribution]

• XXXV Brazilian Meeting on Condensed Matter Physics, *Characterizing the spiking activity of semiconductor lasers with current modulation and optical feedback via ordinal time-series analysis.* Taciano Sorrentino, Andrés Aragoneses, Nicol'as Rubido, M. C. Torrent, Daniel J. Gauthier, Cristina Masoller. Aguas de Lindoia, Brazil, 17 May, 2012. [Poster contribution]

• XXXV Brazilian Meeting on Condensed Matter Physics, *Symbolic statistical ordinal analysis distinguishes determinism from stochasticity in the spiking activity of semiconductor lasers with optical feedback.* Andrés Aragoneses, Nicol'as Rubido, Taciano Sorrentino, M. C. Torrent, and Cristina Masoller. Aguas de Lindoia, Brazil, 17 May, 2012. [Poster contribution]

• NOLINEAL. *Ordinal analysis of the spiking activity of semiconductor lasers with time-delayed optical feedback.* Andrés Aragoneses, Nicolás Rubido, Taciano Sorrentino, M. C. Torrent, and Cristina Masoller. Zaragoza, Spain, 4-6 June, 2012. [Poster contribution]

• Internatinal Conference on Delayed Complex Systems. *Characterizing the spiking activity of semiconductor lasers with current modulation and optical feedback via ordinal time-series analysis.* Taciano Sorrentino, Andrés Aragoneses, Nicolás Rubido, M. C. Torrent, Daniel J. Gauthier, and Cristina Masoller. Palma de Mallorca, Spain, 4-8 June, 2012. [Poster contribution]

• European Optical Society Annual Meeting (EOSAM 2012) *Nonlinear time-series analysis of low-frequency fluctuations in semiconductor lasers with optical feedback.* Andrés Aragoneses, Nicolás Rubido, Jordi Tiana-Alsina, M. C. Torrent, and Cristina Masoller. Aberdeen, Scotland, 25-28 September, 2012. [Oral contribution]

• Congreso de Física Estadística, FISES'12. *Ordinal time-series analysis of low-*

frequency fluctuations in semiconductor lasers with optical feedback. Andrés Aragoneses, Nicolás Rubido, Taciano sorrentino, M. C. Torrent, and Cristina Masoller. Palma de Mallorca, Spain, 18-20 October 2012. [Poster contribution]

• International Symposium on Nonlinear Theory and its Applications, NOLTA'12. *Nonlinear time-series analysis of low-frequency fluctuations in semiconductor lasers with optical feedback*. Andrés Aragoneses, Nicolás Rubido, Jordi Tiana-Alsina, M. C. Torrent, and Cristina Masoller. Palma de Mallorca, Spain, 22-26 October 2012. [Oral contribution]

• Jornada d'Investigadors Predoctorals Interdisciplinària, JIPI-2013. *Distinguishing signatures of determinism and stochasticity in spiking complex systems*. Andrés Aragoneses, M. C. Torrent, Cristina Masoller. Barcelona, 7 february 2013. [Oral contribution]

• Dynamics Days Europe. *Transitions of determinism and stochasticity in time-delayed complex systems with modulation*, Andrés Aragoneses, Sandro Perrone, Taciano Sorrentino, M. C. Torrent, and Cristina Masoller. Madrid, Spain, 3-7 June 2013. [Oral contribution]

• Bienal de Física. *Distinguishing signatures of determinism and stochasticity in spiking complex Systems*, Andrés Aragoneses, Sandro Perrone, Taciano Sorrentino, M. C. Torrent, and Cristina Masoller. Valencia, Spain, 15-19 June, 2013. [Oral contribution]

• International Symposium on Physics and Aplications of Laser Dynamics, ISPALD'13. *Characterizing the Symbolic Dynamics Underlying the Intensity Dropouts of A Semiconductor Laser with Optical Feedback in the Regime of Low Frequency Fluctuations*. Andrés Aragoneses, Sandro Perrone, Taciano Sorrentino, M. C. Torrent, and Cristina Masoller. Paris, France, 29-31 October, 2013. [Oral contribution]

• International Symposium on Physics and Aplications of Laser Dynamics, IS-

PALD'13. *Laser-based dynamical sensor resolving two-dimensional translations at the nanoscale.* Damien Rontani, Seth D. Cohen, Andrés Aragoneses, M. C. Torrent, Cristina Masoller, and Daniel J. Gauthier. Paris, France, 29-31 October, 2013. [Oral contribution]

• Congreso de Física Estadística, FISES'14. *Unveiling the complex organization of recurrent patterns in spiking dynamical systems.* Andrés Aragoneses, Sandro Perrone, Taciano Sorrentino, M. C. Torrent, and Cristina Masoller. Ourense, Spain, 2-4 April, 2014. [Poster contribution]

• Congreso de Física Estadística, FISES'14. *Characterizing the complex dynamics of a semiconductor laser with optical feedback and modulation.* Andrés Aragoneses, Sandro Perrone, Taciano Sorrentino, Daniel J. Gauthier, M. C. Torrent, and Cristina Masoller. Ourense, Spain, 2-4 April, 2014. [Oral contribution]

• SPIE Photonics Europe. *Experimental study of the complex dynamics of semiconductor lasers with feedback via symbolic time-series analysis.* Taciano Sorrentino, Andrés Aragoneses, Sandro Perrone, Daniel J. Gauthier, M. C. Torrent, and Cristina Masoller. Brussels, Belgium, 14-17 April, 2014. [Oral contribution]

• International Commission for Optics, ICO-23. *Characterizing the complex dynamics of a semiconductor laser with optical feedback and modulation.* Andrés Aragoneses, Taciano Sorrentino, Sandro Perrone, Daniel J. Gauthier, M. C. Torrent, and Cristina Masoller. Santiago de Compostela, Spain, 26-29 August, 2014. [Invited Oral contribution]

• International Symposium on Nonlinear Theory and its Applications, NOLTA'12. *Nanoscale-resolution sensing of two-dimensional translations using complex dynamics of a laser diode.* Damien Rontani, Seth D. Cohen, Andrés Aragoneses, M. C. Torrent, Cristina Masoller, and Daniel J. Gauthier. Luzern, Switzerland, 14-18 September 2014. [Invited Oral contribution]

Attendance to courses and research stays

• Curso Dinámica y sincronización en redes biológicas. Red Ibersinc, and Centro de Tecnología Biomédica. Pozuelo, Spain. 1 July - 7 July, 2011.

• Curs d'introducció a Matlab, Universitat Politècnica de Catalunya, Castelldefels, Spain, 27 June - 29 June, 2011.

• Research stay of three months at the laboratory of Professor Daniel J. Gauthier at Duke University, Durham, North Carolina, USA. July-September 2012.

• School of nonlinear optics and nanophotonics. IFT-UNESP, São Paulo, Brazil. 25 November - 6 December, 2013.

• Curso de LABVIEW *Core 1*, Universitat Politècnica de Catalunya, Vinanova i la Geltrú, Spain. 17 March - 19 March, 2014.

Repercussion on the media

• Local media (newspapers and TV) published in ref. [139] *Thesis* (Sci. Rep., **3**, 1778, 2013):

http://www.terrassadigital.cat/detall_actualitat/?id=17143.U2UeVfmSylc

http://www.naciodigital.cat/latorredelpalau/noticia/26246/tenen/comu/xarxes/socials/terratremols

http://www.elperiodico.cat/ca/noticias/terrassa/investigadors-del-campus-upc-terrassa-creen-nou-metode-per-identificar-lordre-dins-sistemes-caotics- complexos-2438914

Acronyms

LFF: Low-Frequency Fluctuations.
IDI: Inter-Dropout Interval.
PDF: Probability distribution Function.
OP: Ordinal Pattern.
TP: Transition Probability.
QP: Quasi-periodic.